Modeling and Simulation of PDMS Micropillars for Microfluidic Viscometer Applications

By

Ayşenur Eser

A Dissertation Submitted to the Graduate School of Sciences and Engineering in Partial Fulfillment of the Requirements for the Degree of

Master of Science

in

Biomedical Engineering

KOÇ UNIVERSITY

August 17, 2018

Modeling and Simulation of PDMS Micropillars for

Microfluidic Viscometer Applications

Koç University

Graduate School of Sciences and Engineering

This is to certify that I have examined this copy of a master's thesis by

Ayşenur Eser

and have found that it is complete and satisfactory in all respects, and that any and all revisions required by the final examining committee have been made.

Committee Members:

____

Özlem Yalçın, Ph.D. (Advisor)

____

Alper Kiraz, Ph.D.

____

Ahmet Can Erten, Ph.D.

Date: August 17, 2018

Dedicated to my family

ABSTRACT

Microfluidics technology has started to be used in a tremendous diversity of applications in various research areas. In the recent years, as one of the user-friendly microfluidic application, micropillar arrays have become very important. Reversible dry adhesives, superoleophobic surface, tunable wetting, micromechanical sensors, and actuators are examples of technological applications where micropillar arrays have been used.

Computational Fluid Dynamics (CFD) simulations are remarkably helpful at design and optimization steps of microfluidic devices. They provide an understanding of the behavior of the fluid and the initial design studies for the optimization of parameters for geometry and methods, hence, reducing the cost, and workload for the microfluidic chip development.

In the present study, we investigate fluid flow characteristics and the micropillar behavior through micropillar based microfluidic channels via conducting a set of case studies that include the change in micropillar shapes, and numbers, and the inter-pillar spacing. As the verification of the simulations, we have produced the PDMS square and cylindrical micropillars using double layer SU-8 master molds fabricated by using standard photolithography method and proceeded with a set of experiments. Experiments were performed with micropillar based microfluidic channels over a range of flow rates from 30 to 150 ml/hr for 1cP, 5 cP viscosity fluids, and blood as the same with the computational fluid dynamics conditions. According to the results, we could predict the micropillar behaviors and the flow profiles under a specific flow rate and for certain viscosity of fluids. We also observed that pressure, wall shear stress, strain rate inside the microfluidic channel, and the force applied to micropillars varies linearly with increasing flow rates for different micropillar shapes and inter-pillar spacing.

The main contribution of this thesis is reducing the time spent, cost and effort in the fabrication process for the development of a micropillars based microfluidic chips. Overall this work demonstrates the simulated and fabricated micropillar based channels with a variety of parameters applied, for finding the optimum micropillar based devices that can be used for viscometer applications.

ÖZET

Son yıllarda, mikroakışkan sistemler, birçok alanda yaygın olarak kullanılmaya başlanmıştır. Kullanımı kolay olan mikroakışkan uygulamalardan biri olan mikro-çubuk bazlı diziler gelişen teknolojiyle birlikte önem kazanmıştır. Geri dönüşümlü kuru yapıştırıcılar, süpereofobik yüzey, ayarlanabilir ıslaklık, mikromekanik sensörler ve aktüatörler mikro-çubuk bazlı dizilerin kullanıldığı uygulama örnekleridir.

Hesaplamalı Akışkanlar Dinamiği (CFD) simülasyonları, mikroakışkan cihazların tasarım ve optimizasyon aşamalarında oldukça faydalıdır. Mikroakışkan tabalı cihazlardaki akış profilleri, cihaz geometrilerinin geliştirilmesinde kullanılan parametrelerinin optimizasyonu ve ilk prototip tasarım çalışmalarında gerekli olan maliyeti ve iş yükünü azaltmayı hedefler.

Bu çalışmada, mikro-çubuk şekilleri olan kanalların kullanımında, farklı mikro-çubuk şekilleri ve mikro-çubukların birbirine olan uzaklıkları inceleyen bir dizi vaka çalışması yaparak mikro-çubuk tabanlı mikroakışkan kanallar yoluyla akış profilleri ve mikro-çubukların akış esnasındaki davranışını araştırdık. Yapılan vaka çalışmalarının doğruluğunu test etmek amacıyla standart fotolitografi yöntemiyle üretilen çift katmanlı SU-8 mastır kalıplar kullanılarak PDMS kare ve silindirik mikro-çubuk yapılar üretilmiş ve gerekli deneyler yapılmıştır. Deneylerde, mikro-çubuk tabanlı mikroakışkan çipler kullanılarak, 30 ila 150 ml / saat arasında akış hızlarında kan, lcP ve5 cP viskoziteli sıvılar ile akış sağlanarak, hesaplamalı akışkanlar dinamiği ile aynı koşullar yaratılmaya çalışılmıştır. Elde edilen sonuçlara göre, belirli akış hızları ve belirli viskoziteye sahip sıvılar için mikro-çubuk davranışlarını ve kanallar içerisindeki akış profillerini daha doğru ve kısa süre içerisinde tespit edebilmekteyiz. Aynı zamanda, farklı mikro-çubuk şekilleri ve mikro-çubukların birbirine olan uzaklıklarının değişimi ile kanal içerisinde oluşan basınç, duvar kesme gerilimi, gerilme hızları ve her bir mikro-çubuğa uygulanan kuvvetin, artan akış hızları ile lineer olarak değiştiğini gözlemledik.

Bu tezin temel katkısı, mikro-çubuk bazlı mikroakışkan çiplerin geliştirilmesi için üretim sürecinde harcanan sürenin, maliyetin ve çabanın azaltılması yönündedir. Genel olarak bu çalışma, viskozimetre uygulamaları için kullanılabilecek optimum mikro-çubuk tabanlı cihazların geliştirilebilmesi için yapılan bir dizi vaka çalışmasının sonuçlarını sunmaktadır.

ACKNOWLEDGEMENTS

My great adventure at Koç University has come to an end. However, before it finishes, I would like to express my gratitude to my family for their genuine love and encouragement all the time. I also would like to express my sincere appreciation and thanks to my thesis advisor Dr. Özlem Yalçın for her care, guidance, and patience in every aspect of my thesis. I would like to thank Dr. Ahmet Erten and Dr. Şenol Pişkin for their support and guidance. I am grateful to Dr. Melikhan Tanyeri who trusted and motivated me to study here at Koç University. There are many people who else I would like to thank; I can start with Dr. Barış Yağcı for countless times of SEM imaging sessions and his great patience and support. My colleagues from here, Ali Cenk Aksu, Yaprak Özbakır, Rhustamzon Melikov, Mahmut Biçer, Ümmü Koç, Mustafa Eryürek, Adil Mustafa helped me and made valuable contributions to my studies when I needed, which gave me the strength and motivation to improve my work. Additionally, I would like to thank my dearest friends Elif Uğurel, Yaprak Özbakır, Burcu Özçimen, Deniz Uğurlu Çimen and Esra Ahunbay for their friendship, care and comfort, especially at the hardest times of my graduate life. Last but not least, I am thankful to everyone for their guidance directly and indirectly to complete this thesis.

Contents

LIST OF FIGURES

LIST OF TABLES

LIST OF EQUATIONS

Chapter 1 INTRODUCTION

Microelectromechanical systems (MEMS) refer to devices consisting of electrical and mechanical components at micro dimensions[1]. Micro- and micro-electronics technology has emerged in the light of innovations in integrated circuit manufacturing, and over the last decade, improvements in the field of MEMS has increased[2].

Among the bio-MEMS applications Lab-on-a-chip (LOC), has an increasing prevalence in recent years, with the evolving technology. (LOC) means that analyzes that can be performed in a laboratory are performed in miniaturized devices of a few millimeters in length. As a result of advances in medicine and biotechnology, the practical applications of technology (LOC) have become more important as the needs for chemical / biochemical analyzes increase. Thus, large laboratories, which require classical methods, have left the complex devices in place for the application of integrated biochips (LOC) technology from microfluidic applications. Metal, glass or plastic, thermoplastic, PDMS or PMMA materials are the base surface materials for lab-on-a-chip devices (LOC)[3].

1.1 Point of Care Diagnostics

Point of Care (POC) devices are easy-to-use diagnostic tools that can be performed in hospitals, emergency rooms or the patient's houses[4-9].The POC sector is a rapidly growing sector and is increasingly being used especially in infectious diseases (due to increased disease and mutations) and in coagulation monitoring tests. Therefore, the need for lightweight, easy to use and portable testing tools is rising[9, 10].

Microfluidic systems provide effective and rapid test results from small volumes in compliance with these developments[11]. Many devices perform rapid testing, and they are divided into three different categories (permanent integrated instruments; pure disposables, and permanent instruments that use disposable components[12].

Permanent integrated instruments: Shows fast and accurate results, cost-effective and are designed for high-throughput work, yet, they need trained personnel. Even with the microfluidic components, frequent calibration and cleaning procedures are needed, because of that, they could not be considered as point of care devices[12].

Pure Disposables: Advantageous aspects are relatively economical because of the use of disposable materials that are commercially available from large-scale production methods. They can be used to detect antigens or antibodies. Another advantageous aspect is that they can withstand more than one year at room temperature[13]

Disposable tests allow for advanced diagnostics without the need for well-equipped laboratory environments. Patients can efficiently use these devices. These tests are mostly used in developed world countries and modern armies[14]

Disadvantages of disposable tests are that they still can not provide sufficient sensitivity, specificity and accuracy.

Another critical issue for disposable tests is their use in conjunction with a reader to ensure that these test materials are evaluated. The readers to evaluate the test and the disposable test material may be an integrated product or a combination that is merely combined in the test phase. The advantages of an integrated product case are that they require less cleaning and less calibration between the two samples. The disadvantages are the need for complex systems, pumps and valves outside the electrical unit.

Integrated products are preferred in hospital environments where more than one can be measured. These products must be used in developing countries as they will require electricity for pumps and valves[12]. The products in which the test material and readers are combined and easily transportable, readily separable from the reader after use, and easily meet the electricity requirement[12].

For these reasons, it is necessary to develop more compact products, especially those that are developing countries and cheaper disposable components for home use.

1.2 Microfluidic Technologies & Lab-on-a-Chip Applications

In microfluidic systems, liquids in micro and nano-volumes can be transported and transported through micrometer-sized channels[15, 16].

In microfluidic systems, external forces such as capillary action, an interaction of the liquid with channel walls and surface tension are essential. In the production of devices operating with microfluidic technology, different designs are needed, including micropumps to provide flow, microcirculation points responsible for processing and microchannels and conduits to deliver fluids.

In micron and nano-scale, the analysis methods have been refined by working with fluids in a controlled manner, making it easier to develop these methods[16].

The micro-technology is most recently developing in Bio-MEMS. Bio-MEMS are micro-electro-mechanical structures that enable the analysis, measurement and monitoring of biological materials. The fields in which Bio-MEMS is being developed are systems used in lab-on-a-chip (LOC) applications, biomedical devices, chemistry and biochemistry applications[17].

Biological microanalysis chips, known as bio-MEMS, can perform many biochemical and medical analyzes inexpensively, quickly and with high precision without the need for laboratory equipment. While these devices have developed existing applications, they make diagnosis and treatment methods that are not possible before, cheap and accessible[2].

Microfluidic system applications in bio-MEMS applications have enabled the use of micro- and nano-sized fluids to provide a controlled flow of sample fluid with reduced amounts of expensive reagents required for medical diagnostics and chemical analysis and analysis. Thus, rapid and accurate diagnosis of a micron-sized sample is provided[16].

1.2.1 Microfluidic Viscometers

Shear viscosity is the most widely characterized material property of chemical and biological fluids; therefore, monitoring and analyzing changes in viscosity of these fluids such as polymers, oils, paints, food, drugs and fermentation products, blood, plasma, cerebrospinal fluid and amniotic fluid is essential in industrial and medical diagnostics [18, 19]. Consequently, measuring viscosity by easy, rapid, cost-efficient methods using low sample volumes is of great importance in numerous industrial and medical fields. Microfluidic devices provide a natural platform for fast, low-cost viscosity measurements using minute amounts of sample. For that reason, researchers recently have developed several miniaturized viscometers using microfabrication and microfluidics technology. One of the most used methods for the viscometer approach is the pressure sensing which involves pressure drop measurement across a straight microchannel for known flow rates[18]. Zou et al.[21] presented a microfluidic viscometer fabricated using a novel microwire molding technique for measuring viscosities of biological fluids. Kim et al.[22] reported a hybrid method using a smartphone camera and a microfluidic device. Their measurement was based on estimating pressure inside a microfluidic chip by measuring the width ratio between reference and sample fluids using images captured by a smartphone camera. With a similar method called flow rate sensing, instead of pressure drop, the flow rate is measured. By this method, Hudson et al.[23] miniaturized the capillary viscometry to handle microliter-volume samples. The implementation approach involves pressure chambers with an internal flow path in the form of a tubular capillary combined with an in-line flow meter for measuring the flow rate. Another viscometer approach is the droplet-based, which relies on the analysis of the flow of a sample plug immersed in an outer phase such as oil for calculating visco-sity[19]. Li et al.[20] reported a microdroplet-based viscometer which is capable of measuring the viscosity of both Newtonian and non-Newtonian fluids by measuring the length of the droplets. This method finds its advantages by using a minimum amount of sample volume. As a final example of the viscometer methods is the surface-tension method can be given. In this method, capillary pressure and wetting properties of surfaces have been used to draw fluids into microchannels. Guillot et al.[24] measured viscosity of fluids flowing in a microchannel as a function of shear rate. They calculated the mean shear rates sustained by the sample fluid.

Even though microfluidic viscometers have many advantages, they have some limitations such as the channel deformation when flexible construction materials are used such as PDMS[21, 22]. However, the field of microfluidic viscometry is growing, and substantial opportunities exist for the development of devices with enhanced capacities.

1.2.2 Micropillar Based Microfluidic Device Approach

Recently, micropillar arrays have become very important. Reversible dry adhesives[23-26], superoleophobic surface[27], tunable wetting[28, 29], micromechanical sensors[30-35], and actuators[32, 34, 36-38] are examples of technological applications where micropillar arrays have been used. Micropillar arrays possess large surface area and large mechanical compliance. The topography of micropillar arrays that is well-separated from the underlying substrate gives rise to the researchers to design and explore[39].

Benefits of micropillar arrays have caused evolutionary features. For example, regeneration of a gecko foot due to hierarchical arrays of nano and micropillars[40]; and superhydrophobic nature of lotus leaves. Notwithstanding, due to their small dimensions and large aspect ratio, these structures have a high surface area to volume ratio. Hence, they are susceptible to surface forces like adhesive forces between the microstructures and liquid capillary forces when immersed and dried from the liquid, leading to collapse of the pattern.

The effect of capillary forces on the stability of micropillar arrays has critical importance for the production of high fidelity micropillar arrays, and their manipulation for the vast spectrum of applications. Below, some of the applications of pillar arrays are explained.

Force sensors and actuators

Small bending stiffness is a critical feature offered by micropillar arrays. Hence, applications of force sensors and actuators at microscale is contributed by this feature. Micropillar arrays have been used widely for the study of the mechanical response of living biological cells[30, 31, 35]. A living cell lying on top of micropillar arrays strives traction forces that could be evaluated by measuring the deflection of the tips of the underlying micropillars. The geometry of the micropillar arrays affects the sensitivity and spatial resolution of the force measurement[32]. A high aspect ratio of micropillars produces small bending stiffness; therefore, more tip deflection and higher sensitivity occur, and small inter-pillar separation causes better spatial resolution. By using this approach, du Roure et al.[31] studied the traction force created by epithelial cells on an array of PDMS micropillars by observing the deflection of the micropillars; they could achieve a spatial resolution of cell mechanics down to 2 microns. Tan et al.[35] applying a similar method, investigated the cell morphology effect, on the cell generated traction forces on PDMS micropillar arrays. Additionally, micropillar arrays started to be used as actuators in response to external forces. Evans et al.[36] showed the actuation of PDMS-ferrofluid composite micropillar arrays by applying an external magnetic field. Another example demonstrated by Sniadecki et al.[32] can be given that, by putting the cells on PDMS-cobalt nanowire composite micropillar arrays they created a cell response to external forces and actuated the pillars by applying a magnetic field. Consequently, the force generated by living cells can be used to actuate micropillars, and thus realizing bio-microactuators[32, 34, 37, 38]. Tanaka et al.[38] show that they can successfully generate forces over 1 μN by chemically stimulated muscle cells attached to micropillars. In the meantime, Sidorenko et al.[41] proved reversible actuation of Si pillars through swelling and drying of the hydrogel coating by coating hydrogels on silicon nanopillar arrays. As another advancement, micropillar arrays with elliptical cross-section have been created in addition to the many nano and micropillars have isotropic cross-sections (e.g., spherical and square)[42]. The latter demonstrates anisotropic rigidity (more rigid in the direction of major axis of the ellipses), causing anisotropic cell migration on such substrates.

Biomimetic dry adhesives

There has been considerable interest in the production of arrays of tall microstructures to mimic the biological design inspired by robust, reversible and dry adhesion of gecko foot hairs[40]. Each gecko foot is covered with an array of half a million-keratin hair called setae, which are about 130 μm long and 15 μm in diameter. At the tip, each setae split into hundreds of long filaments called spatulae. Each of the spatulae produces a tiny van der Walls force of about 10^{-7} N, resulting in a fierce adhesion force, 10 N/cm^2 in each gecko foot, where the high aspect-ratio nature of the setae and spatulae plays an important role. Since they are small bending stiffness, the setae can conformably contact the microscopic roughness of any surface, enabling almost all the spatulae to make physical contact with the surface, causing a large cumulative adhesive force. In the meantime, locating the mechanically compliant setae at a critical angle with the surface eases the detachment of the gecko toe[40]. Hence, in order to design gecko-inspired, synthetic and reversible dry adhesive, it is crucial to creating the stable, tall structures with optimum aspect ratio and Young's modulus[23, 24]. Greiner et al.[24] produces a periodic array of PDMS micropillars and demonstrated increasing adhesion with an increase in the pillar aspect-ratio. Depending on the same principles, Qu et al.[26] designed dry adhesive tape comprising carbon nanotube arrays, which produced strong adhesion in the shear direction and small adhesion in the normal lift-off direction similar to the behaviors observed in gecko foot. Furthermore, Mahdavi et al.[25] formed a biocompatible and biodegradable tissue adhesive from micropillars of poly (glycerol-co-sebacate acrylate) elastomer, demonstrating the microstructure could improve the wet adhesion.

In addition to the applications mentioned above, micropillar arrays have also been used in enhanced heat transfer[43].

1.3 Thesis Objectives

With the review of the literature of the microfluidic point of care devices and the micropillar approach on different applications in this chapter, it is noted that micropillar-based microfluidics is a growing field in Lab-on-a-chip devices. The main goal of this thesis is to apply CFD simulations to understand the flow behavior inside micropillar-based microfluidic devices and the characteristics of the micropillars, in order to find suitable operating conditions and optimal designs for micropillars-based microfluidic viscometer applications. Hence, we performed an extensive fluid flow studies through micropillars based microfluidic chips, consisting different designs that are changing with micropillar shapes and inter-pillar spacing.

The organization of this thesis is as follows;

Chapter 2. Theorethical Background. This chapter outlines the fundamental concepts of computational fluid dynamics.

Chapter 3. CFD Model and Operating Parameters. This chapter describes finite volume models that are used for calculation and verification for micropillar based microfluidic chip design.

Chapter 4. Structural Analysis. In this chapter, computational simulations were carried out to determine the deformation response of individual pillars and pillar arrays. The simulations are used to determine the origins of improved sensitivity and correlate the experimental data.

Chapter 5. Methodology. This chapter describes the fabrication methods and the process for the micropillar based microfluidic chips developed in this work.

Chapter 6. Experimental Setup. In this chapter, a detailed description of the experimental setup and the image analysis for the deformation of all fabricated micropillar designs is provided.

Chapter 7. Findings and Discussion. This chapter presents the results that is accomplished and the findings of experimental and computational measurements.

Chapter 8. Conclusion and Future Work. This chapter presents a summary of the thesis highlights and corresponding conclusion with a potential future directions.

Chapter 2 THEORETICAL BACKGROUND

2.1 Fluid flow simulation with CFD

A new approach has been developed to investigate the microfluidics, with the advancement of computational power and simulation methods. The fluid flow behavior and material characteristics inside a microfluidic device are essential for microfluidic applications; as a consequence, computational fluid dynamics (CFD) simulations provide a simple way to study those parameters that are difficult to observe by experiments.

2.1.1 Computational Fluid Dynamics

Computational Fluid Dynamics (CFD) is computer software that can be used to calculate resistances that occur due to fluid flow. The most important advantage of these programs is that it sloves flow patterns that can be difficult, expensive or impossible to study using traditional, experimental techniques. By using the mesh of control volume and control volume created for any form, it is possible to get an idea of the characteristics examined without the need for costly test equipment. Thus, the sizes of the designed forms can be arranged among themselves in comparison with each other. The duration of the numerical solution can vary depending on the size of the control volume and the mesh size. This period is also directly related to the processor speeds of the used computers. However, it should be emphasized that it is only possible to reach the data without any doubt after the numerical simulations made by model experiments.

In this thesis, the geometry created in AutoCAD program was transferred to the ANSYS Workbench 19 software, and computational study of flow characteristics and case studies based on the deformation of the micropillars inside a microfluidic chip has been performed.

2.1.2 Governing Equations

In engineering studies such as two-dimensional flows like jet streams, channel flows, two plate flows or three-dimensional complex flows becomes unstable with a specific Reynolds number.

With low Reynolds numbers flow course is laminar. High Reynolds numbers` flows are turbulent. This means that the flow`s caotic and random movements as well as its speed and pressure vary according to time. Flow continuity and Navier-Stokes (momentum) equations are used to describe Laminar flow. The continuity equation for incompressible fluids are:

$$\nabla . V = 0 \qquad or \qquad \frac{\partial u}{\partial x} + \frac{\partial v}{\partial y} + \frac{\partial w}{\partial z} = 0$$

Equation 2:1 – Continuity Equation

Navier-Stokes equations are;

$$\frac{\partial u}{\partial t} + u\frac{\partial u}{\partial x} + v\frac{\partial u}{\partial y} + w\frac{\partial u}{\partial z} = -\frac{1}{\rho}\frac{\partial P}{\partial x} + \upsilon\nabla^2 u + X$$

$$\frac{\partial v}{\partial t} + u\frac{\partial v}{\partial x} + v\frac{\partial v}{\partial y} + w\frac{\partial v}{\partial z} = -\frac{1}{\rho}\frac{\partial P}{\partial y} + \upsilon\nabla^2 v + Y$$

$$\frac{\partial w}{\partial t} + u\frac{\partial w}{\partial x} + v\frac{\partial w}{\partial y} + w\frac{\partial w}{\partial z} = -\frac{1}{\rho}\frac{\partial P}{\partial z} + \upsilon\nabla^2 w + Z$$

Equation 2:2 – Navier-Stokes Equations

Where, $V = ui + vj + wk$ is the fluid velocity, P is the pressure, ρ is the density, υ is the constant fluid viscosity and the X, Y, Z are the constants of the force $F_{ex} = Xi + Yj + Zk$ that effects the flow[44].

Navier-Stokes equations consist of four unknown parameters of the velocity vector and the pressure. For simple geometries that arise in microfluidics, the Navier-Stokes equations are easy to solve analytically. To give an example, in a straight channel that a uniform cross-sectional shape, there is incompressible flow, around the areas that are away from the entrance or an exit, the nonlinear term $u \cdot \nabla u = 0$[45]. This step is a notable simplification concerning the analytical results. Steady solutions for simple geometries depend on the flow rate. The solutions can be realistic only when the flow speed is adequately small (according to the Reynolds number calculations). Otherwise, the steady solutions would not be stable, so the flow becomes a turbulent flow.

Setting the boundary conditions is necessary to solve the Navier-Stokes equations. For most cases, the velocity is zero on all stationary boundaries (no-slip boundary condition), and the pressure, velocity distribution or flow rate are determined on the two ends of the device.

2.1.3 Newtonian and Non-Newtonian Fluids

Viscosity is the most important property for fluids. Fluid viscosity is affecting the fluid flow including the flow in pipes and the flow of blood in vessels[46].

Two plates model

A two plates model is explaining viscosity. If the viscous fluid considered between two parallel plates, and a force is applied to the top plate through a specific direction, then the fluid between the plates should move to that direction with the same speed, because of the no-slip boundary condition of the fluid close to the top plate. Likewise, fluid close to the bottom plate should be stable. Fluid will have different acceleration in different regions between the plates. The applied force is named as shear and the force per unit area is called shear stress[46].

Newtonian Fluids

According to Newton's law of viscosity found in 1687, Newtonian fluids have a linear relationship between the strain rate and the shear stress, the viscosity of the fluid is constant. Since the force applied to the area is resulting the shear stress, it described as the equation below;

$$\tau = \frac{F}{A}$$

Equation 2:3 – Shear Stress Equation

Where τ (N/m^2) is the shear stress, F (N) is the force and the A (m^2) is the area of the force applied. The ratio of the velocity and the distance between the plates is called shear rate, and it can be show as the equation below;

$$\dot{\gamma} = \frac{dV}{dx}$$

Equation 2:4 – Shear Rate Equation

Where, $\dot{\gamma}(l/s)$ is the shear rate, $dV(m/s)$ is the velocity and $dx(m)$ is the distance between the plates.

The viscosity (η_a) can be explained as the slope of the shear stress versus the shear rate curve for the Newtonian fluids. It is shown in the equation below;

$$\eta_a = \frac{\tau}{\dot{\gamma}}$$

Equation 2:5 – Viscosity Equation for Newtonian Fluids

When deciding a flow profile, Reynolds number range should be considered. The small number of Re indicates that the friction flow, which inertia effects are not significant, is acting frictionally. The median values of the number of Re correspond to the laminar flow. The high Re numbers will likely cause turbulent flow, which slowly changes over time, but with strong high-frequency random fluctuations on it[47].

Water, gasoline, oil, air can be given as an example of a Newtonian fluid[46].

Non-Newtonian Fluids

Non-Newtonian fluids are not showing a linear relationship with shear stress and shear rate ratio change. Viscosity is depends on the strain rate and not constant for non-newtonian fluids. While the viscosity is not constant at a specific temperature and pressure, the shear rate of the fluid depends on the flow geometry and the kinematic history of the fluid element.

Non-newtonian fluids are characterized in 2 groups[48];

- Time dependent
- Independent fluids

Time-dependent non-Newtonian fluids have two categories as thixotropic and rheopectic fluids. The viscosity of thixotropic fluids are depending on time and can show shear thinning behavior, yet they change with the kinematic history of the fluid. Similarly, the viscosity of the rheopectic fluids depends on time and can show shear thickening behavior, yet changes with the kinematic history of the fluid. Honey can be given as an example for thixotropic fluids and printer inks can be given as rheopectic fluids[48].

Independent non-newtonian fluids are defined with different models as; Shear thickening (dilatant) fluids, Shear thinning (Pseudoplastic) fluids, Bingham plastic and Hershel-Buckley model[49].

Shear thickening (dilatant) fluid viscosities are increasing with the shear rate. Examples are honey and cornstarch solutions[49]. The viscosity of the Bingham plastic has a linear slope yet; it needs a finite rate of yield stress to flow. In the Hershel-Buckley model, the viscosity is non-linear and the model develops the yield stress before the flow. Finally in the shear thinnig (Pseudoplastic) models, the fluid viscosity is decreasing with the increase of the shear rate.

Casson Model

Stresses bigger than the yield stress allows the real plastic otherwise known as the Casson fluid to flow. The shear rate of the fluid causes the viscosity to decrease and after some time this causes the Casson fluid to act as a Newtonian fluid. Some heterogeneous fluids can have a particulate phase. This particulate phase asks for yield stress because it forms aggregates at low rates of shear. Blood mostly contains red blood cells and is considered a non-newtonian fluid, so it follows the narrow pathway it is shown. High-value viscosity is acquired with the red blood cells coming together to form aggregates at low shear rates. However, if low shear rates cannot be obtained in these circumstances are not met and the blood has a viscosity of 3cP mimicking a Newtonian fluid.

The Casson fluid modeling is widely used to show the mathematical way blood behaves in narrow arteries as shown by studies of Blair and Coley et al.[50, 51] . The Casson fluid is popular for this model because it is a yield stressed non-Newtonian fluid. Casson showed that the yield stress for blood is nonzero at low shear rates. Merrill et al.[52] revealed that this modeling could be used with tubes of 130-1000 μm in diameter.

It is said that the Casson fluid model is the best representation of blood in previously said conditions. The Casson fluid model can be applied to humans with a range of hematocrits and shear rates.

Casson fluid can be shown with the equation of an incompressible flow[53];

$$\tau_{ij} = \begin{cases} 2\left(\mu_B + p_y/\sqrt{2\pi}\right)e_{ij}, & \pi > \pi_c \\ 2\left(\mu_B + p_y/\sqrt{2\pi_c}\right)e_{ij}, & \pi < \pi_c \end{cases}$$

Equation 2:6 – Rheological Equation of the Casson Fluid

Where, $\pi = e_{ij}e_{ij}$ is the product of deformation rate, π_c is the critical value of π, μ_B is the dynamic viscosity of the non-newtonian fluid, p_y is the yield stress of the fluid.

In this thesis, Casson model (shear thinning model) has been used for the fluid material, in need of blood viscosity properties for the fluid flow simulations of non-newtonian fluids.

2.1.4 Boundary Conditions

One of the mathematical fluid flow requirements is boundary conditions. It is required to determine the boundary conditions for the region where is selected for the problem since not to simulate the entire area. Primary and boundary conditions have to be carried out while solving Navier-Stokes equations. Non-physical solutions might be shown up as the cause by inapplicable boundary conditions.

Regarding each numerical values, the standard boundary conditions are categorized by considering physical conditions. There are three types of (Dirichlet, Neumann, and mixed) spatial boundary conditions for steady state problems. However, solid walls, inlets, symmetry boundaries, pressure boundary conditions, outflow boundary conditions, cyclic or periodic conditions are physical boundary conditions which are commonly used in fluid problems.

The fluid enters the domain from the inlet ; hence its velocity, pressure, and mass flow rate have to be known. The fluid must be specified when it has disorganized characteristics. Pressure boundary conditions are generally used as boundary conditions due to pressure gradient induces the fluid in limited flows. If the features of flow velocity or pressure are known before the solution of the problem, outflow boundary conditions are operated at flow exits. If the flow at the exit is approximately in a fully expanded state, this condition is suitable to use.

2.1.5 Finite Volume Method

In fluid dynamics problems, it is not possible to solve equations with analytically related boundary conditions, a consequence of complexity, 3D phenomena, and turbulence effects. These can be generalized with finite difference methods, finite volume methods, and finite element methods.

These methods can be applied to fluid mechanics, but studies and acquired experience have shown that precise and straightforward solutions can be obtained by the finite volume method[44, 54]. Another reason for the widespread use of the finite volume method is that it can be applied to complex and curvilinear geometries.

Before the equations can be solved, the flow volume and boundary conditions must be determined. It is essential to know the flow volume clearly and it should be known precisely which volume the equations will be solved. In the finite volume method, the flow volume is divided into small finite volumes (discretization) and the corresponding equations are solved separately for each finite volume.

Although the use of small finite volumes obtains a more accurate solution, dividing the flow volume into as many final volumes as possible forces computer capacity and extends the analysis time. The recommended method is to divide the domain first into a large number of finite volumes, and in a given phase of the analysis process, locate the domains that will be divided into smaller finite volumes[44].

After the flow volume is divided, the type of boundary condition on the surfaces should be given as a type of information. It is defined at this stage which regions of flow volume are fluid and which regions are surrounded by solid boundaries. At this stage, the surface that the fluid flows, the surface that the fluid will come out, wall surfaces of the flow volume and the interfaces should be given.

In studying a flow, the boundary layer formed on the solid surfaces should be emphasized. The ignoring of the boundary layer causes both the inaccuracies of the inaccurate velocity distribution and the calculated stress, friction coefficient and torque to be calculated according to the change in velocity on the solid surface[44]. As already mentioned, in the regions close to the solid surfaces where the velocity change is high, more intensive and suitable compartments should be made for the boundary layer flow.

2.1.6 Finite Element Method

The finite element method is a method developed for solving the problems in different disciplines such as elasticity, structural analysis, thermal analysis, flow analysis and electromagnetic in engineering branches such as complex machine, construction, and aeronautical engineering[55]. In the finite element method, which is more frequent than others, the solution area is divided into a large number of elements to increase the resolution accuracy. The elements "nodes" to obtain sets of equations[54].

Elements should be selected appropriately and placed according to the structure of the problem. Elements should be chosen small where the variable changes suddenly. It is also essential to number these elements and their node points as well as select the appropriate elements. After the splitting to the finite elements, an interpolation function is determined which shows the variation of the magnitude within the region to be expressed[56]. The closer the task is to the truth, the better the convergence in the solution.

Using finite elements, problems in fields such as solid mechanics, liquid mechanics, acoustics, electromagnetism, biomechanics, heat transfer can be solved. Also, it can be applied to the systems with complicated boundary conditions, systems with non-uniform geometry, steady state, time-dependent and eigenvalue problems, linear and non-linear problems.

In this thesis, in the first studies, finite volume method has been used with the Ansys FLUENT analysis system with pre-designed rigid structured micropillars for fluid flow simulations. Subsequently, to investigate the deflections of the micropillars, a case study has been carried out using nonlinear solution methods with finite element method with Ansys Static Structural analysis system.

Chapter 3 CFD MODEL & OPERATING PARAMETERS

In this chapter, CDF model for the fluid pattern of the microfluidic chip is discussed. A detailed overview of the simulation parameters in this work is presented. Using a computational simulation during the prototyping stage is an efficient way to identify problems or validate a design before fabrication. Different chip designs were evaluated using the 3D computational fluid dynamic (CFD) simulation modules in ANSYS Fluent.

3.1 Geometry

At the beginning of the simulations, the geometry must be defined. There are two geometries has been designed both for the fluid and the solid domains. ANSYS Workbench presents a visual interface named Design Modeler that the geometry of a structure with various parts and features can be drawn easily. Geometries were carried out in Design Modeler. The shape and the dimensions of the rectangular microfluidic channel has been chosen with respect to the experiemental data. A three dimensional body of rectangular channel was created as a base for test designs. There are one inlet, one outlet and a rectangular body for the fluid domain. The length of the rectangular body is set as 12 mm length, 1.025 mm width and a depth of 80 µm. Each micropillar has the aspect ratio of 3:1 and a diameter/edge of 25 µm and a height of 75 µm. Figure 3.1 represents an example fluid domain modeled in Ansys Design Modeler.

The flow characteristics obtained inside a micropillar based microfluidic channel via case studies that includes, change in micropillar shapes, and numbers, and the inter-pillar spacing in test designs. As shown in Figure 3:1, the micropillars are placed in the middle of the channel as vertical arrays. Table 3:2 shows the specifications of the case studies that have been conducted.

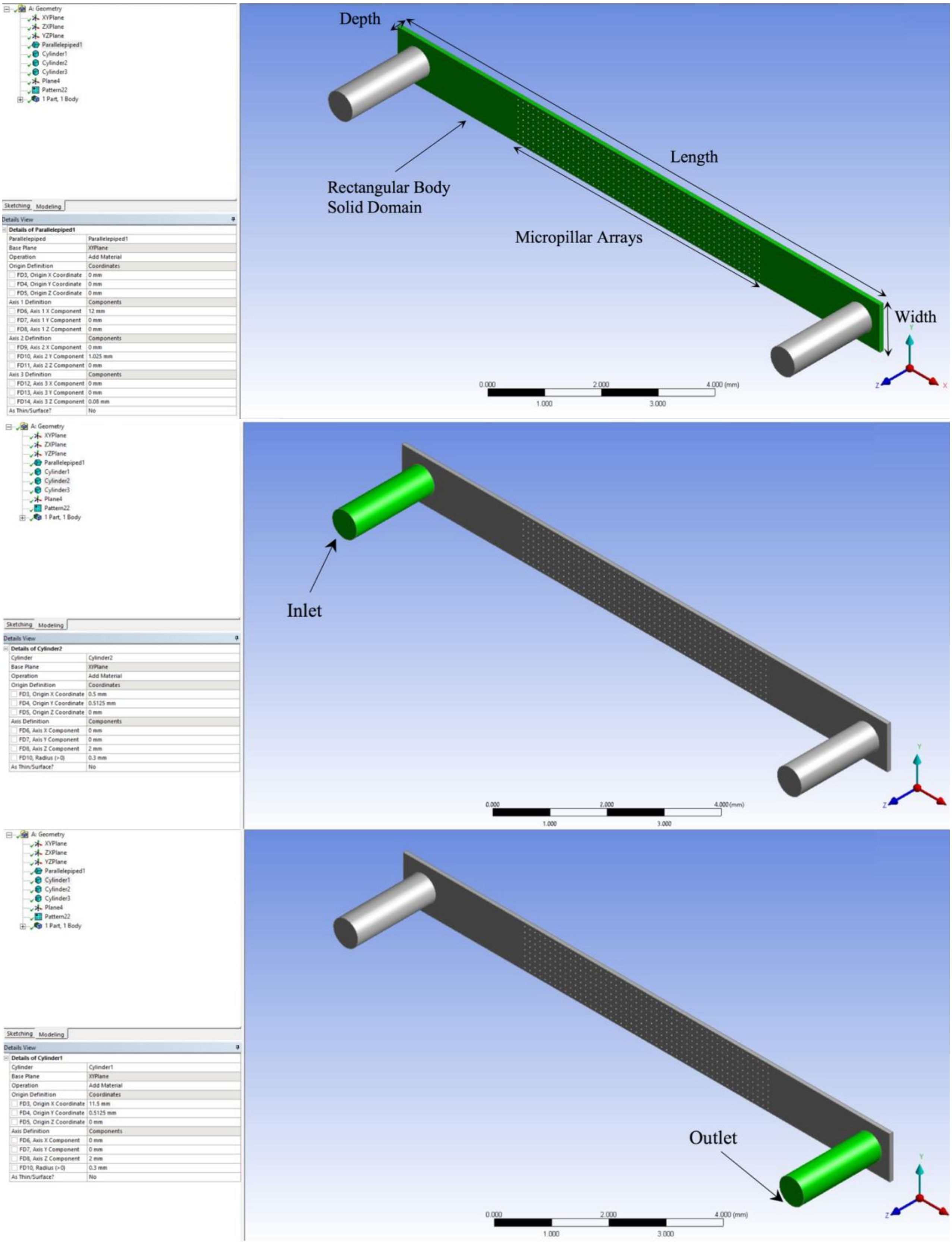

Figure 3:1 Fluid domain geometry

Dimensions	Size(mm)
Channel Length	12
Channel Width	1.025
Channel Depth	0.08
Inlet diameter	0.3
Inlet Tubing Length	2
Outlet diameter	0.3
Outlet Tubing Length	2
Micropillar diameter/edge	0.025
Micropillar Height	0.075

Table 3:1 Dimensions of the rectangular microfluidic channel

Case Study	Micropillar Shape	Inter-pillar Spacing(µm)	Micropillar #
Case 1	Cylindrical	25	1800
		50	900
		75	531
Case 2	Square	25	1120
		50	600
		75	400
Case 3	Diamond	25	1120
		50	600
		75	400
Case 4	Triangle	25	1700
		50	671
		75	504

Table 3:2 Test matrix for Ansys Fluent simulations

3.2 Mesh

Meshing was carried out with ANSYS meshing software with a CFD physics preference using the Fluent solver. Mesh creation is one of the most critical steps for the simulations. Too many cells might result in a long time for solver calculations. With less number of mesh elements are a risk for not having accurate results compared to experimental data. One of the main purposes of doing this simulation is trying to capture and understand the flow characteristics inside micropillar based channel and the velocity component perpendicular to the channel surface. Therefore, a better resolution or a relatively fine mesh in the pillar area was needed. Though, after some meshing methods and operation, the finite volume model of the fluid mesh chosen to consist of 15699661 elements and 3043891 nodes. The geometry meshed with the tetrahedral cells. Element sizing is decided by the size function adaptive, with a coarse relevance center, slow transition and a fine span angle center. In order to achieve a more accurate view of velocity field around and behind a pillar, element size used was 0.004 mm. The element size was chosen to ensure that the mesh would provide sufficiently accurate results. The mesh properties used can be seen below in Figure 3:2, and the geometry mesh shown in Figure 3:3. As a mesh convergence study of the simulations, by comparing the same geometry on four different meshes, a specific mesh has been determined for reliable results. The element sizes used is shown in Table 3:3 and the results are shown in Figure 3:4. In all cases the cell size is tolerably small and the flow profiles are reasonable. However, as for more accuracy in results of flow conditions and the micropillars displacement calculations, 0.04 mm element size was chosen.

Details of "Mesh"	
Display	
Display Style	Body Color
Defaults	
Physics Preference	CFD
Solver Preference	Fluent
Relevance	0
Export Format	Standard
Export Preview Surface Mesh	No
Element Order	Linear
Sizing	
Size Function	Adaptive
Relevance Center	Coarse
Element Size	4.e-003 mm
Mesh Defeaturing	Yes
Defeature Size	Default
Transition	Slow
Initial Size Seed	Assembly
Span Angle Center	Fine
Bounding Box Diagonal	12.2050 mm
Average Surface Area	1.2427e-002 mm^2
Minimum Edge Length	2.4e-002 mm
Quality	
Check Mesh Quality	Yes, Errors
Target Skewness	Default (0.900000)
Smoothing	Medium
Mesh Metric	None
Inflation	
Use Automatic Inflation	None
Inflation Option	Smooth Transition
Transition Ratio	0.272
Maximum Layers	5
Growth Rate	1.2
Inflation Algorithm	Pre
View Advanced Options	No
Assembly Meshing	
Method	None
Advanced	
Number of CPUs for Parallel...	Program Controlled
Straight Sided Elements	
Number of Retries	Default (0)
Rigid Body Behavior	Dimensionally Reduced
Triangle Surface Mesher	Program Controlled
Topology Checking	No
Pinch Tolerance	Please Define
Generate Pinch on Refresh	No
Statistics	
Nodes	3043891
Elements	15699661

Figure 3:2 Mesh details

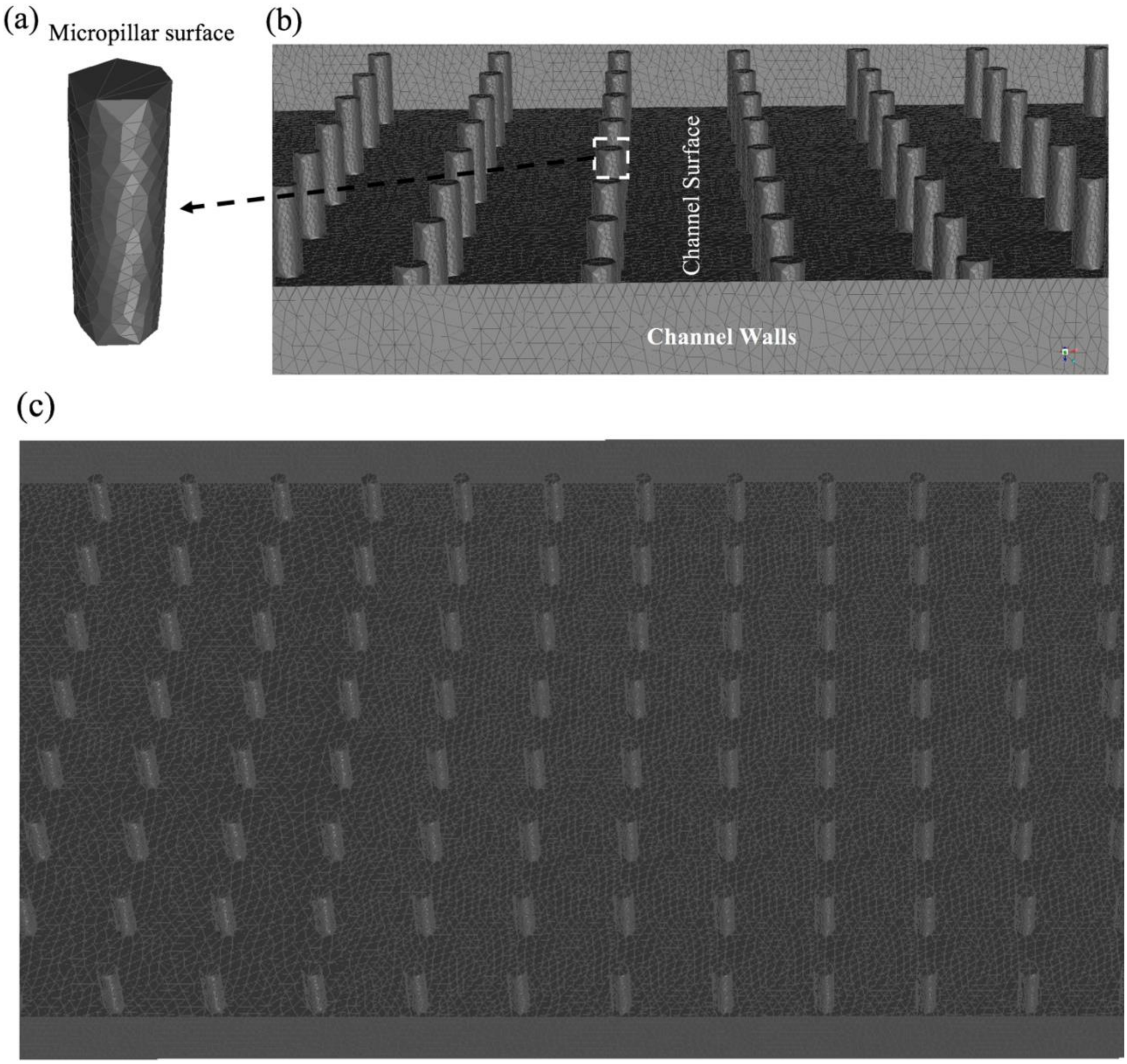

Figure 3:3 Geometry mesh. (a) Cylindrical micropillar mesh. (b) Side-view of the solid mesh. (c) Perspective-view of the solid mesh.

Element Size(mm)	# of Elements	# of Nodes
0.01	2566758	13521530
0.007	4188571	22240554
0.005	9583202	7145325
0.04	15699661	3043891

Table 3:3 Mesh Convergence Study

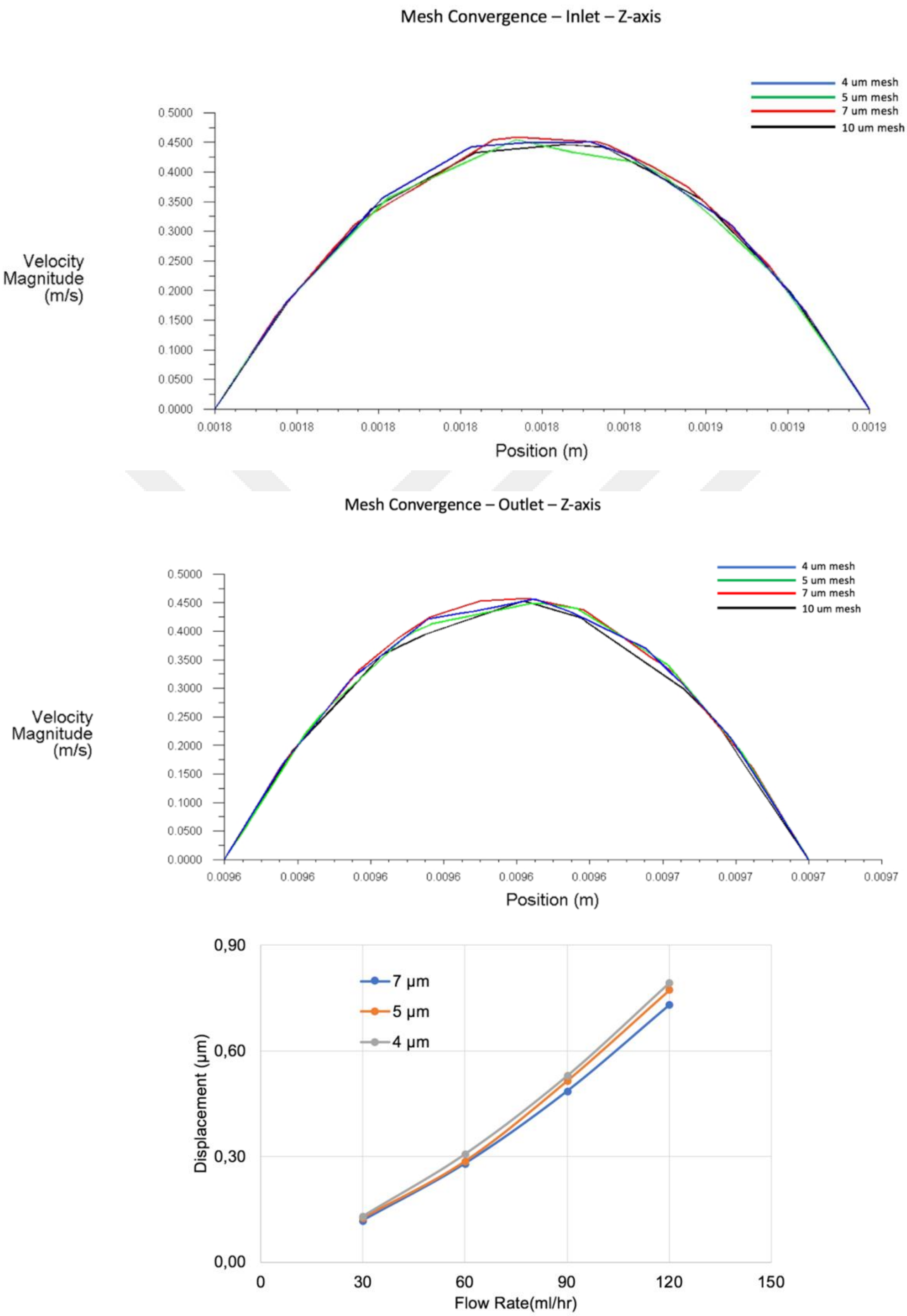

Figure 3:4 Mesh convergence graphs of velocity profiles for inlet and outlet. Flow Rate vs displacement graph of different element sizes.

3.3 Simulation Settings

Finite volume method is used for a steady time simulation using the CFD software ANSYS Fluent. The pressure-based solver has used for the simulations. The pressure-based solver is a solution algorithm that solves the governing equations consecutively. The general settings have been given in Figure 3:5 In the Fluent launcher, double precision is specified for accuracy in the residuals, and parallel processing is specified for reducing the computing time via making use of all the processors inside the computer. The Fluent launcher is given detailed in Figure 3:6.

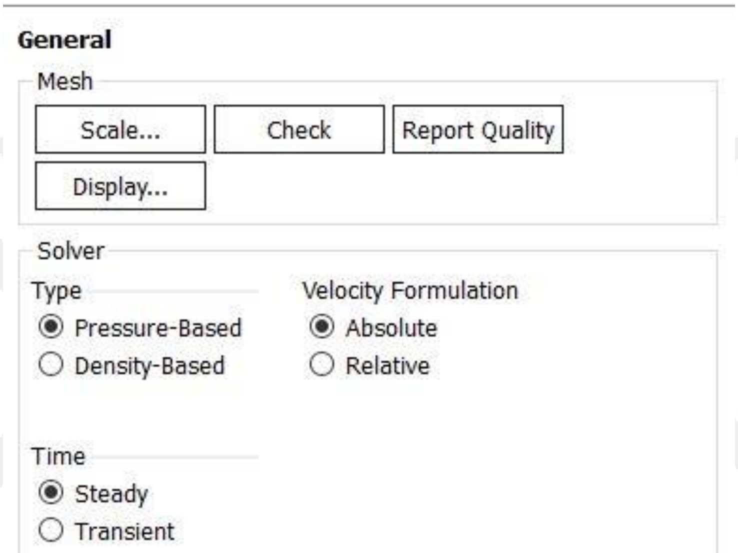

Figure 3:5 Solution setup – General settings

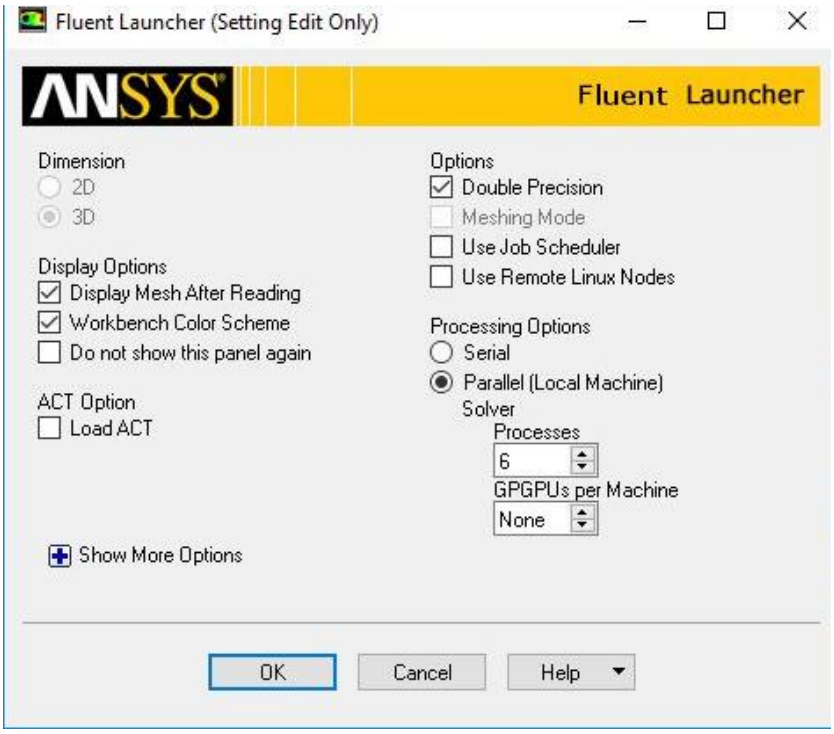

Figure 3:6 Fluent launcher

The viscous model has been selected as laminar, as the flow rates needed for the simulations are low flow rates that do not require a turbulent model. There are two fluid materials has been used for the simulations. The viscous model that is used for the first simulations is a Newtonian fluid that is the glycerol-water solution with a density of 0.001 $kg/$(m·s) and a constant viscosity of 998.02 $kg/m3$ for the simplification of the work. The second material that has been used is the Casson model, which is a non-newtonian fluid and the most common yield stress model for blood[57]. Literature shows that, in the case of moderate shear rate flows, blood behaves like a Casson fluid, and Casson model is the for most common yield stress model for blood. Therefore, it is suitable to assume blood as a Casson model in our simulations [64]. The Casson model has a user-defined function for viscosity that calculates the viscosity according to the change in strain rate, where the initial value measured is 4.89 cP and a constant density of 1060 $kg/m3$. For the solid body, aluminum was selected. The materials chosen for the simulations is shown in Figure 3:7. Fluent setup has a cell zone and boundary condition section. In this project, cell zone condition has the solid_mesh_, which corresponds to the rectangular channel that the fluid flows. Boundary conditions are set at inlet, walls, and outlet. Inlet conditions have the pressure constant and the velocity range that starts from 30ml/hr to 150ml/hr to compare the behavior of the force per micropillars at different flow rates. Flow rates that were used in the simulations converted to velocity magnitudes. The converted versions are shown in Table 3:4. Outlet condition is zero relative pressure. Other walls are set to be no slip stationary wall. Boundary conditions are shown in Figure 3:8. Finally, the reference values for the simulations are shown in Figure 3:9

Flow Rate (ml/hr)	Velocity Magnitude (m/s)
30	0.029473
45	0.044209
60	0.058946
75	0.073683
90	0.088419
105	0.103156
120	0.117893
135	0.132629
150	0.147366

Table 3:4 Flow rate conversion

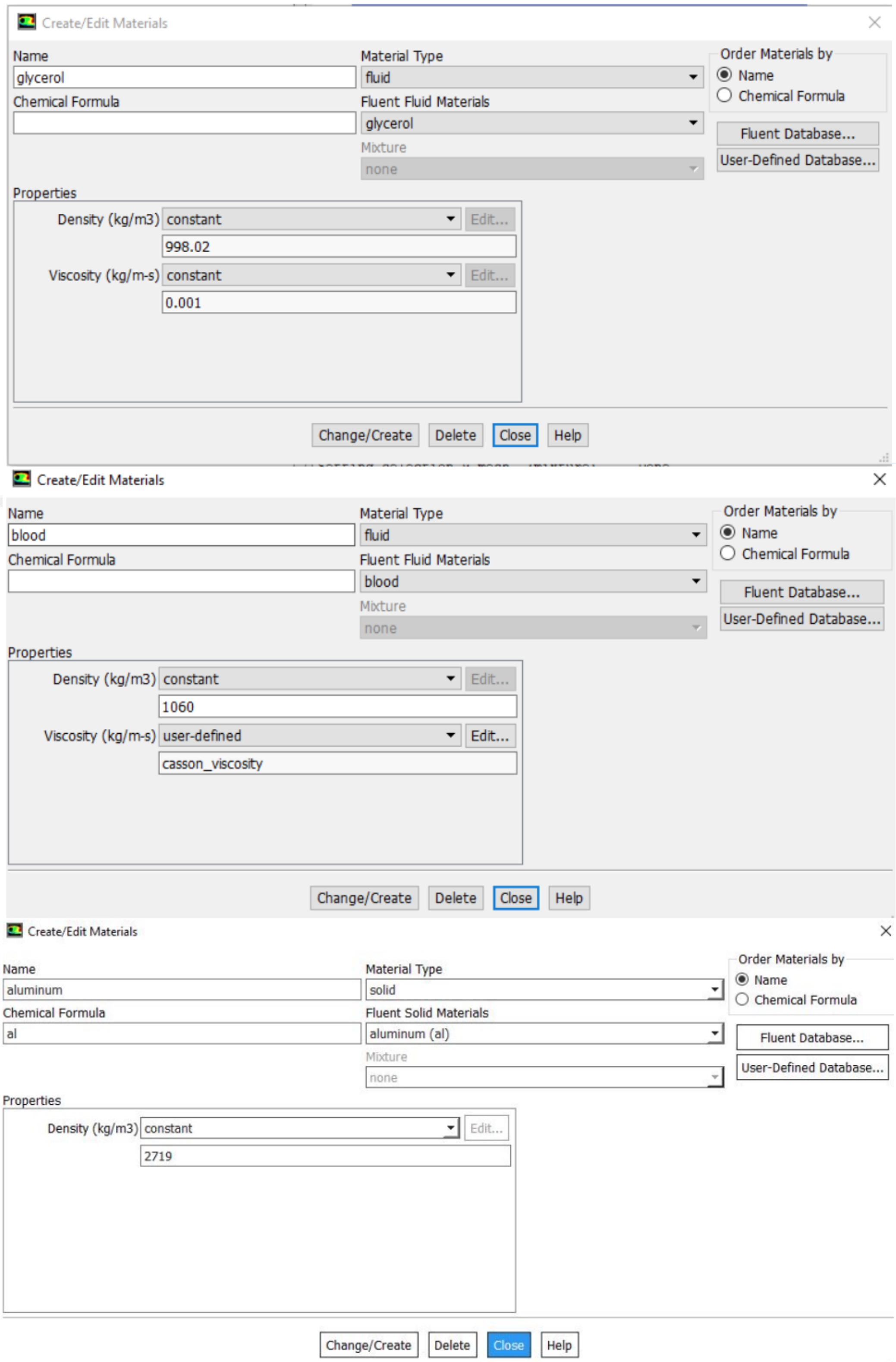

Figure 3:7 Fluent material selection

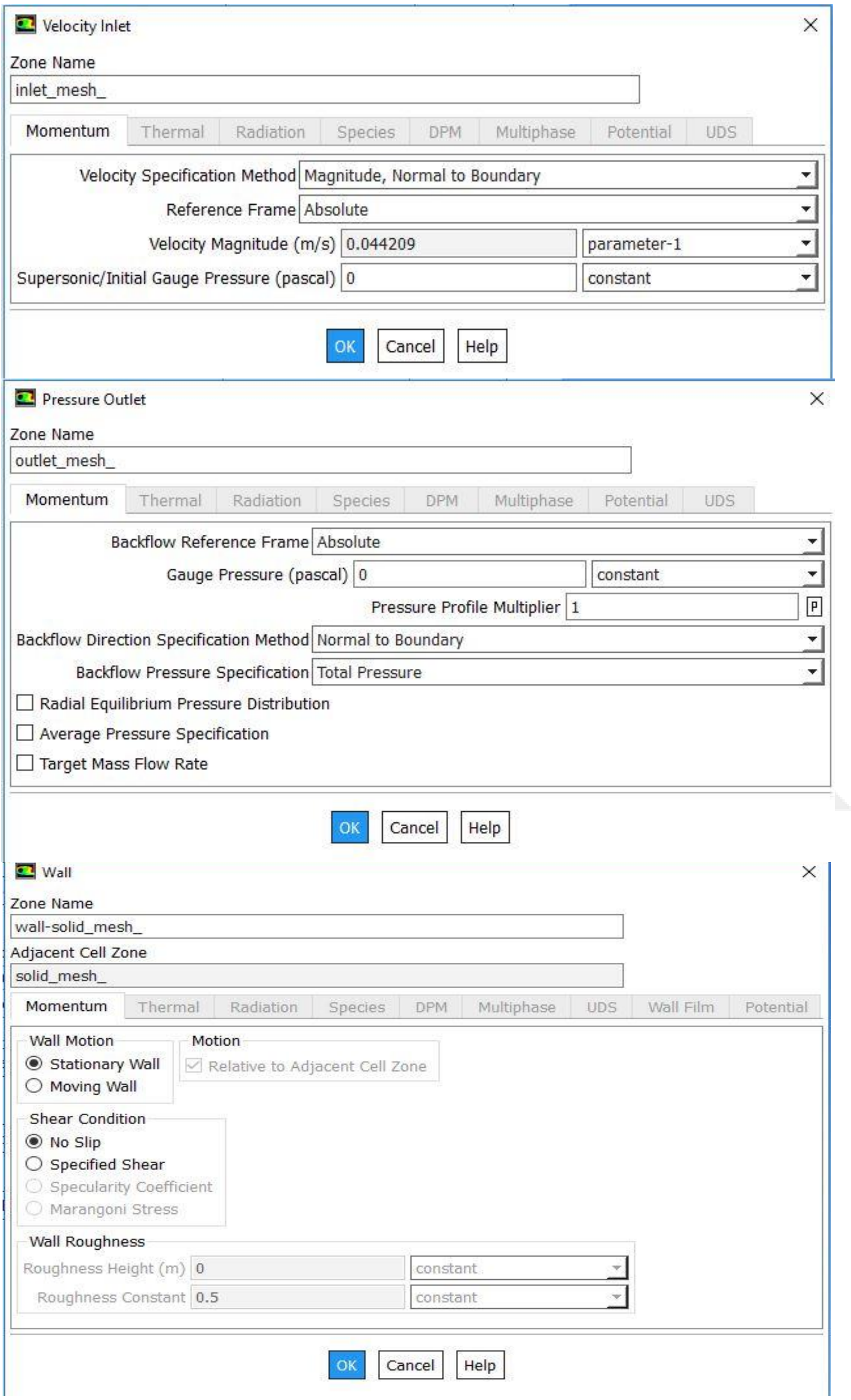

Figure 3:8 Boundary cinditions

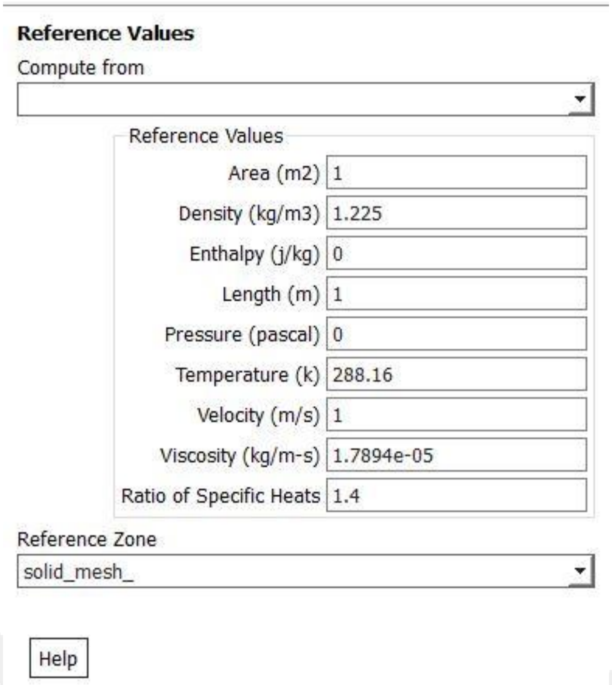

Figure 3:9 Reference values for simulation setup

3.4 Solution

Solution sections start with the solution method. Finite volume method is used for the spatial discretization method. The solution methods and the solution controls for under-relaxation factors are given in Figure 3:10. The residuals monitor is shown in Figure 3 :11. Solution initialization is essential in assuring that initial conditions are similar to the values generated in the converged results. Solution initialization defines the flow variables ; hence the program initializes the flow field according to these values. Initial conditions are set for the beginning of the flow from that boundary. Initialization method for this project is chosen as Hybrid initialization. Number of iterations are set to 1000 iterations for the run calculation. The convergence impulse is shown in figure 3 :12.

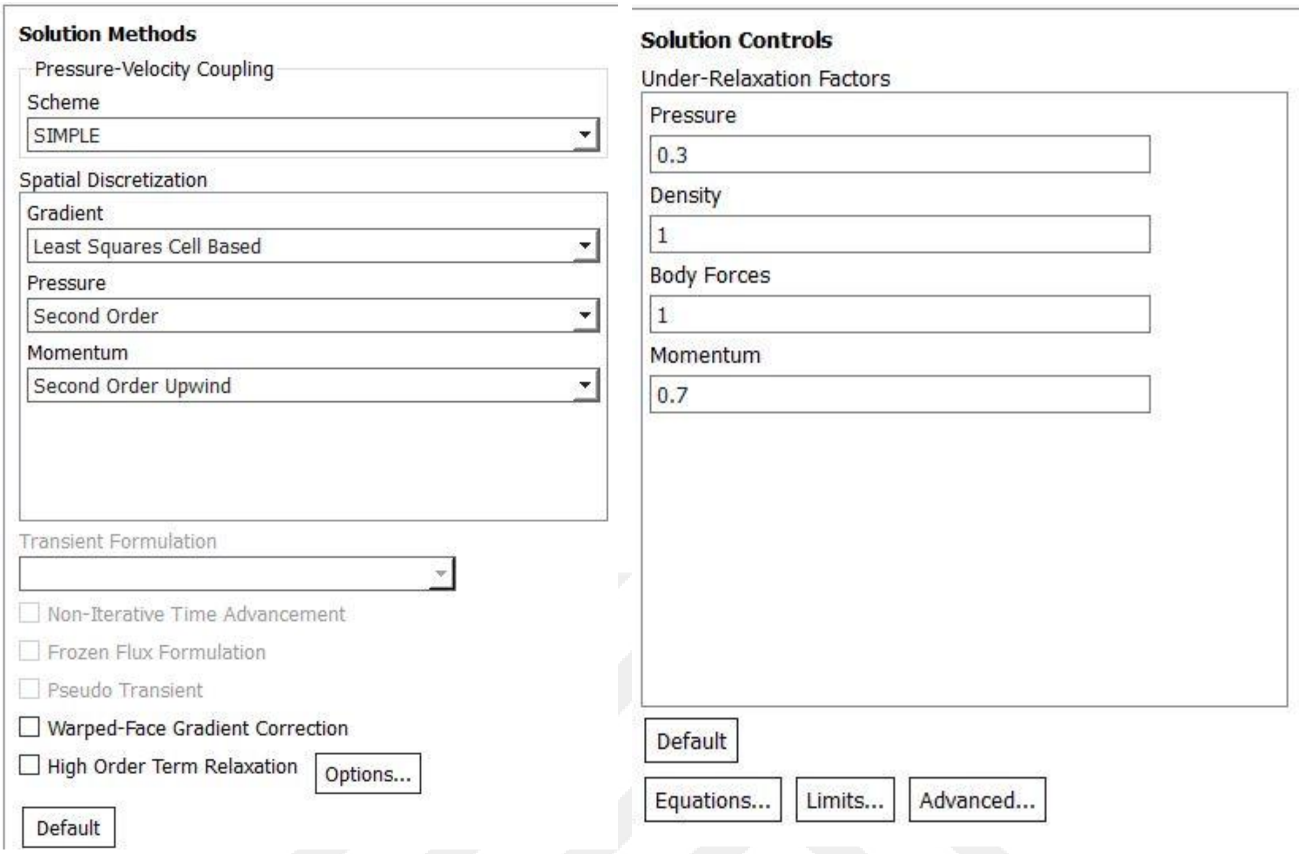

Figure 3:10 Solution methods and solution controls

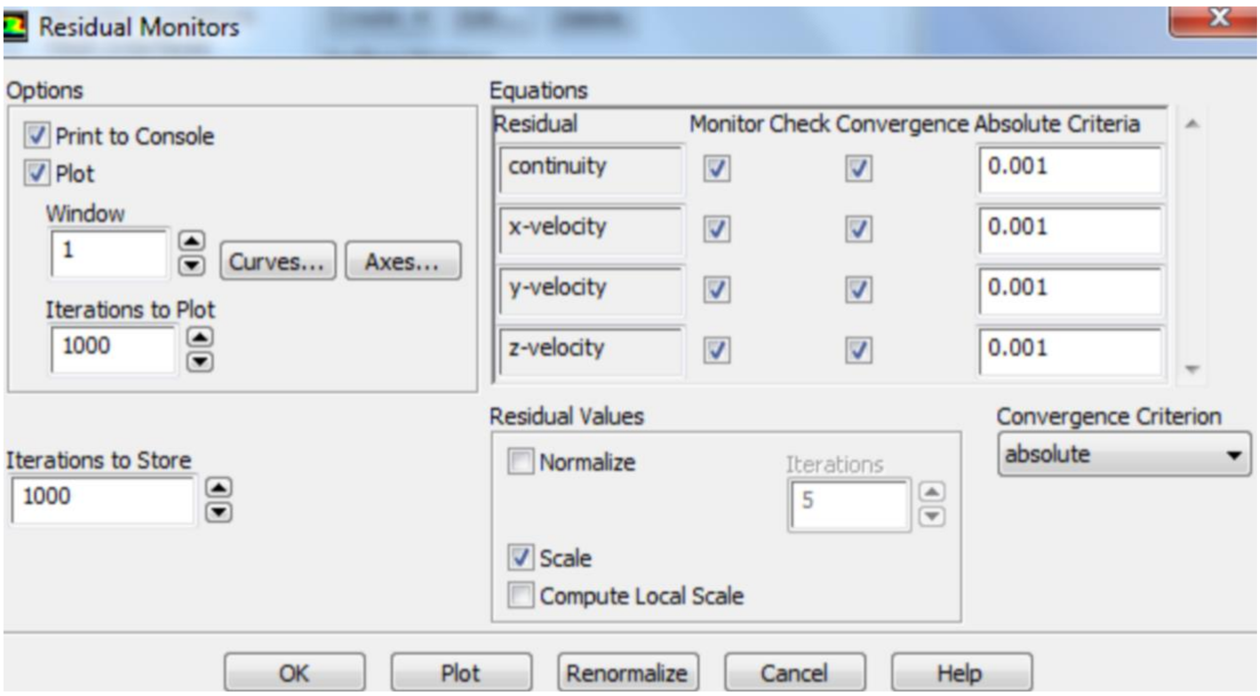

Figure 3:11 Residual monitors

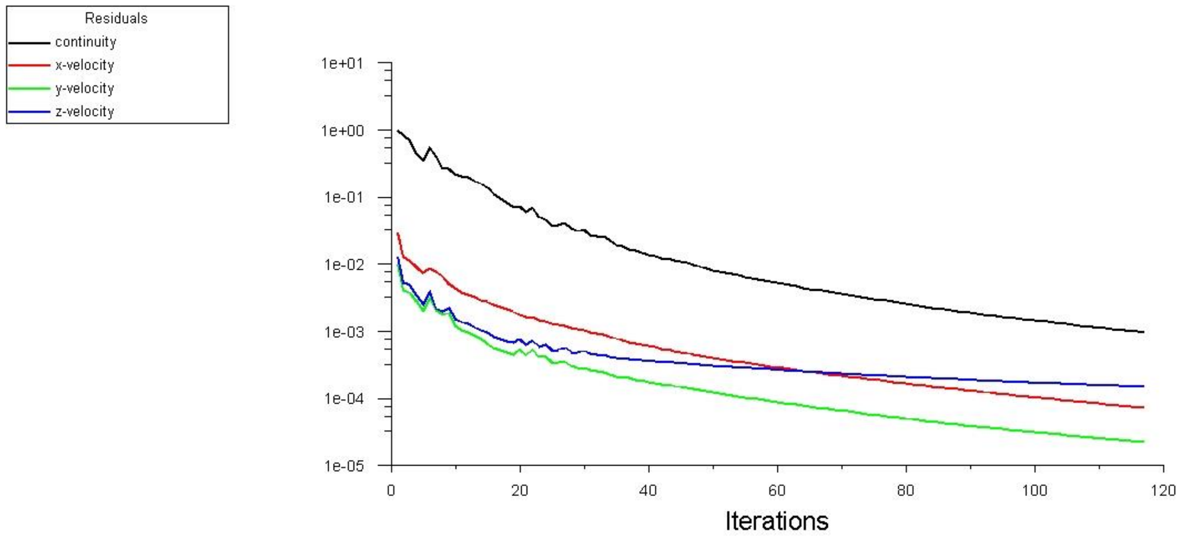

Figure 3:12 Residual graph

Convergence goals are achieved if each variable has been reached to the convergence criteria. The default criterion is that each residual will be reduced to a value of less than 10−3. In some cases, the residuals may not go under the convergence criteria set in the setup. However, observing the characteristic flow variables through iterations could show that the residuals have stagnated and do not change with further iterations.

Chapter 4 STRUCTURAL ANALYSIS

Static Structural is used in ANSYS to model the structural setup.

4.1 Geometry

The geometry of micropillars created to observe the FSI (fluid-structure interactions) with micropillar displacements. The bounding rectangular channel has 12 mm length, 1.025 mm width and a depth of 112 µm. Each micropillar has the aspect ratio of 3:1 and a diameter/edge of 25 µm and a height of 75 µm. Figure 4.1 shows an example solid domain geometry details. Figure 4:2 represents the cylindrical micropillars used for structural analysis. The material for bounding rectangular channel and the micropillars is PDMS.

Table 4:1 and Table 4:2 shows the specifications of the case studies that have been conducted with static structural.

Case Study	Micropillar Shape	Inter-pillar Spacing(µm)	Micropillar #
Case 1	Cylindrical	75	531
Case 2	Square	75	400

Table 4:1 Test matrix for Ansys Static Sturctural simulations.

Dimensions	Size(mm)
Channel Length	12
Channel Width	1.025
Channel Depth	0.08
Inlet diameter	0.3
Inlet Tubing Length	2
Outlet diameter	0.3
Outlet Tubing Length	2
Micropillar diameter/edge	0.025 - 0.030
Micropillar Height	0.075 – 0.090

Table 4:2 Dimensions of the rectangular microfluidic channel

Details of "Geometry"

Definition	
Source	C:\Users\generic\Desktop\yeni\75umspa-1cP\75umspa-1cP_files\
Type	DesignModeler
Length Unit	Meters
Element Control	Program Controlled
Display Style	Body Color
Bounding Box	
Length X	12. mm
Length Y	1.025 mm
Length Z	0.112 mm
Properties	
Volume	0.48892 mm^3
Mass	0. kg
Scale Factor Va...	1.
Statistics	
Bodies	1
Active Bodies	1
Nodes	409277
Elements	1946914
Mesh Metric	None
Basic Geometry Options	
Parameters	Independent
Parameter Key	
Attributes	Yes
Attribute Key	
Named Selecti...	Yes
Named Selecti...	
Material Prope...	Yes
Advanced Geometry Options	
Use Associativity	Yes
Coordinate Sys...	Yes
Coordinate Sys...	
Reader Mode S...	No
Use Instances	Yes
Smart CAD Up...	Yes
Compare Parts ...	No
Analysis Type	3-D
Decompose Di...	Yes
Enclosure and ...	Yes

Details of "Solid"

Graphics Properties	
Definition	
Suppressed	No
Stiffness Behavior	Flexible
Coordinate System	Default Coordinate System
Reference Temperature	By Environment
Behavior	None
Material	
Assignment	PDMS
Nonlinear Effects	Yes
Thermal Strain Effects	Yes
Bounding Box	
Length X	12. mm
Length Y	1.025 mm
Length Z	0.112 mm
Properties	
Volume	0.48892 mm^3
Mass	0. kg
Centroid X	5.998 mm
Centroid Y	0.5126 mm
Centroid Z	9.7773e-002 mm
Moment of Inertia ...	0. kg·mm^2
Moment of Inertia ...	0. kg·mm^2
Moment of Inertia ...	0. kg·mm^2
Statistics	
Nodes	409277
Elements	1946914
Mesh Metric	None

Figure 4:1 Solid domain geometry in Static Structural

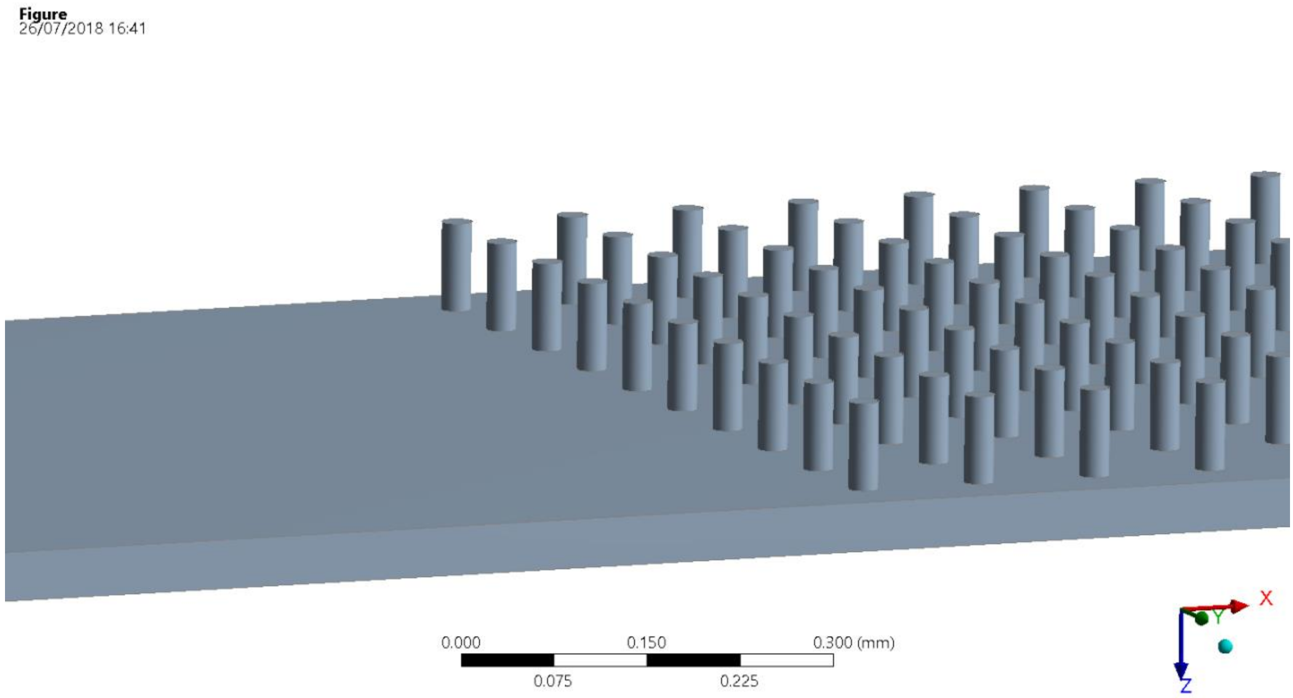

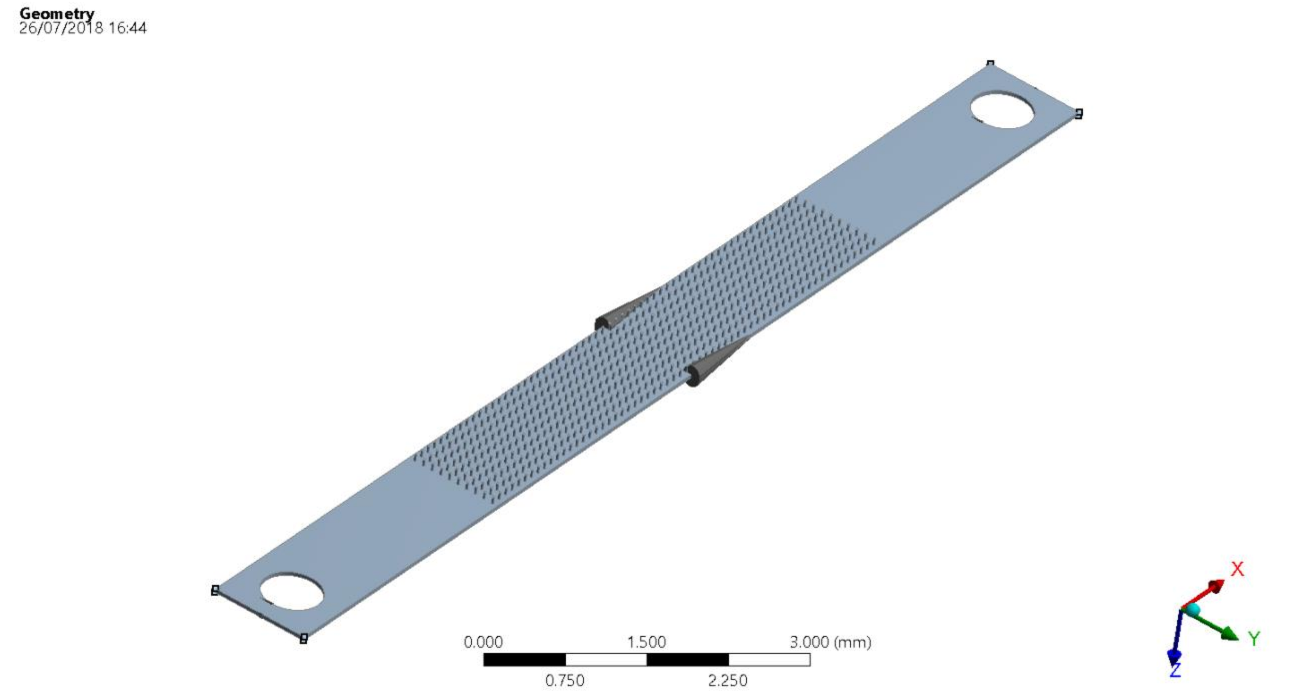

Figure 4:2 Solid domain geometry design

4.2 Mesh

In order to determine the optimum mesh size regarding both accuracy and computation time, the finite element model is divided into two parts and only the micropillars that will be analyzed for displacement meshed with face sizing with a smaller element size. The chosen element was for micro-pillars was 1 µm, and the rest structure meshed with 1 mm element size. Figure 4:3 shows the mesh selections. Figure 4:4 shows the meshed geometry.

Details of "Mesh"	
Display	
Display Style	Body Color
Defaults	
Physics Preference	CFD
Solver Preference	Fluent
Export Format	Standard
Export Preview Surface Mesh	No
Element Order	Linear
Sizing	
Size Function	Curvature
Max Face Size	1.0 mm
Mesh Defeaturing	Yes
Defeature Size	Default (5.e-003 mm)
Growth Rate	Default (1.20)
Min Size	Default (1.e-002 mm)
Max Tet Size	Default (2.0 mm)
Curvature Normal Angle	Default (18.0 °)
Bounding Box Diagonal	12.0440 mm
Average Surface Area	2.3113e-002 mm²
Minimum Edge Length	4.e-002 mm
Quality	
Check Mesh Quality	Yes, Errors
Target Skewness	Default (0.900000)
Smoothing	Medium
Mesh Metric	None
Inflation	
Use Automatic Inflation	None
Inflation Option	Smooth Transition
Transition Ratio	0.272
Maximum Layers	5
Growth Rate	1.2
Inflation Algorithm	Pre
View Advanced Options	No
Assembly Meshing	
Method	None
Advanced	
Number of CPUs for Parallel...	Program Controlled
Straight Sided Elements	
Number of Retries	0
Rigid Body Behavior	Dimensionally Reduced
Triangle Surface Mesher	Program Controlled
Topology Checking	Yes
Pinch Tolerance	Default (9.e-003 mm)
Generate Pinch on Refresh	No
Statistics	
Nodes	409277
Elements	1946914

Details of "Face Sizing" - Sizing	
Scope	
Scoping Method	Named Selection
Named Selection	all
Definition	
Suppressed	No
Type	Element Size
Element Size	1.e-003 mm
Advanced	
Defeature Size	Default (5.e-004 mm)
Size Function	Uniform
Behavior	Soft
Growth Rate	Default (1.2)

Figure 4:3 Meshing Details

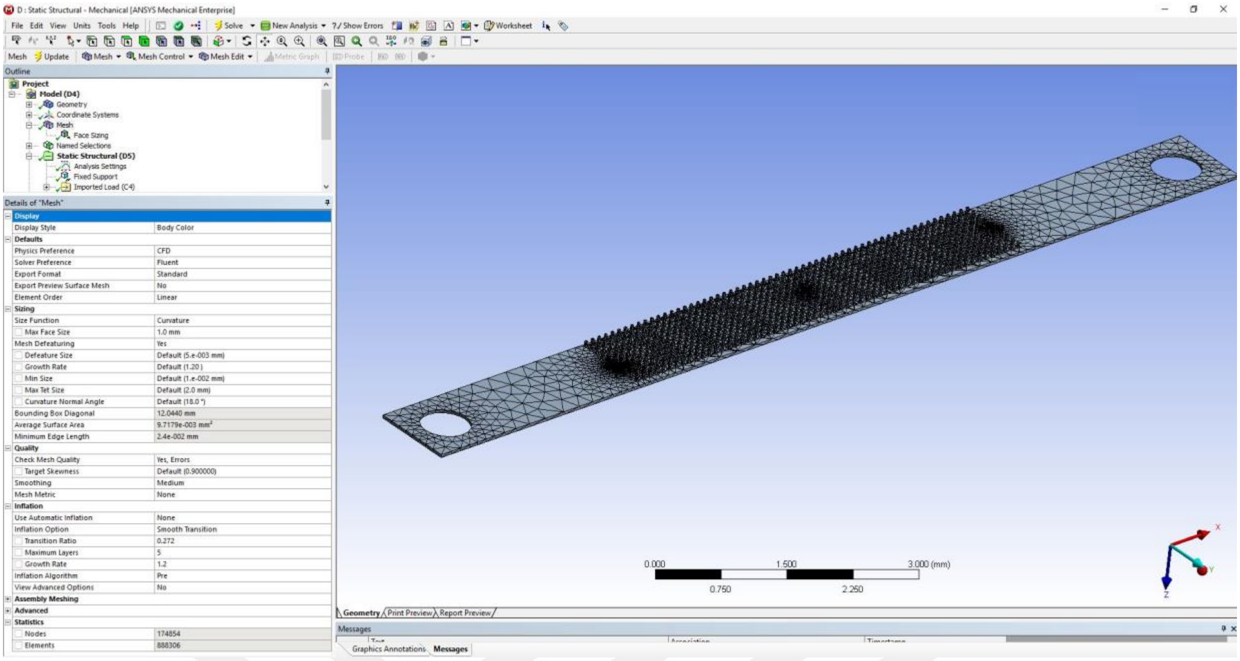

Figure 4:4 Meshed Geometry

4.3 Simulation Settings

The material property input is given from the Engineering Data module in static structural. For this study, we define the material as PDMS. After the material name is defined, the properties such as density, elasticity, Young's modulus, Poisson ratio should be given. The PDMS and the structural steel properties are shown in Figure 4:4.

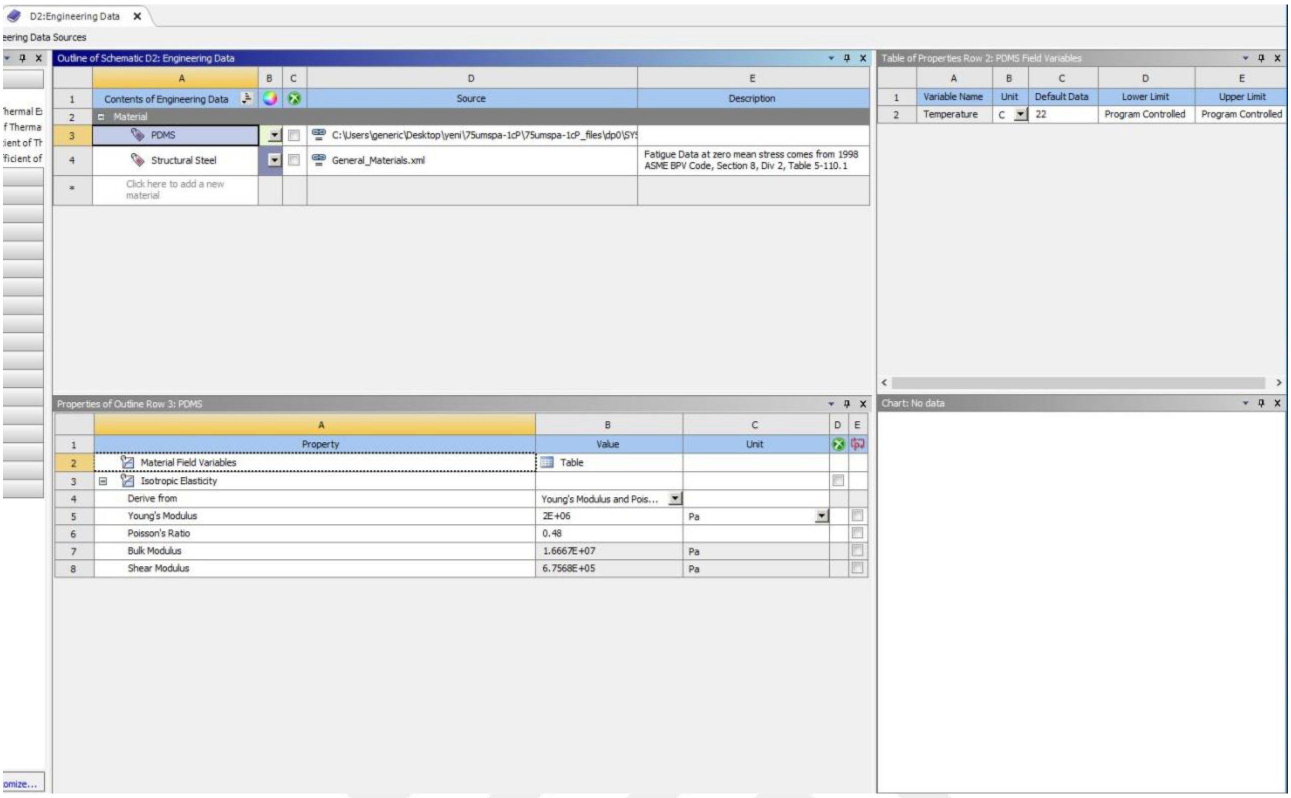

Figure 4:5 Engineering Data

In this study, micropillars are modeled by using one solid body to simplify the model and shorten the analysis time. The environment temperature is defined as 22°C, same as the room temperature that we have done the experiments. The analysis settings are shown in Figure 4:5. For the mechanical boundary conditions, a support can be assigned to a point, edge or surface, as these options can define the displacements of the support. While the modeling of the dynamic micropillars, fixed support is assigned one end of the micropillars along with the rest of the solid structure. In order to obtain the displacement of the micropillars, the pressure data should be defined or imported from the Fluent simulations. Therefore, with the import data function, the pressure data (force per area) of specific micropillars were imported as shown in Figure 4:6. The deformation of the model is calculated with the Equation below;

$$D_{total} = \sqrt{D_x^2 + D_y^2 + D_z^2}$$

Equation 4:1 – Deformation of the model

Where D_{total} is the total displacement and the D_x, D_y and D_z are the directional displacements.

Details of "Analysis Settings"	
Step Controls	
Number Of Steps	1.
Current Step Number	1.
Step End Time	1. s
Auto Time Stepping	Off
Define By	Substeps
Number Of Substeps	5.
Solver Controls	
Solver Type	Program Controlled
Weak Springs	Off
Solver Pivot Checking	Program Controlled
Large Deflection	On
Inertia Relief	Off
Rotordynamics Controls	
Coriolis Effect	Off
Restart Controls	
Generate Restart Poi...	Program Controlled
Retain Files After Fu...	No
Combine Restart Files	Program Controlled
Nonlinear Controls	
Newton-Raphson O...	Program Controlled
Force Convergence	Program Controlled
Moment Convergence	Program Controlled
Displacement Conve...	Program Controlled
Rotation Convergen...	Program Controlled
Line Search	Program Controlled
Stabilization	Off
Output Controls	
Stress	Yes
Strain	Yes
Nodal Forces	No
Contact Miscellaneo...	No
General Miscellaneo...	No
Store Results At	All Time Points
Analysis Data Management	
Solver Files Directory	C:\Users\generic\Desktop\yeni\75umspa-1cP\75umspa-1cP_files\...
Future Analysis	None
Scratch Solver Files ...	
Save MAPDL db	No
Contact Summary	Program Controlled
Delete Unneeded Fil...	Yes
Nonlinear Solution	Yes
Solver Units	Active System
Solver Unit System	nmm

Figure 4:6 Analysis Settings

Details of "Fixed Support"	
Scope	
Scoping Method	Geometry Selection
Geometry	6 Faces
Definition	
Type	Fixed Support
Suppressed	No

Details of "Imported Pressure 3"

Scope	
Scoping Method	Named Selection
Named Selection	InletPillar
Definition	
Type	Imported Pressure
Tabular Loading	Program Controlled
Suppressed	No
Transfer Definition	
CFD Surface	wall solid_mesh_
CFD Data	
CFD Results File	C:\Users\generic\Desktop\yeni\75umspa-1cP\75umspa-1cP_files\...
Settings	
Mapping Control	Program Controlled
Mapping	Profile Preserving
Weighting	Triangulation
Transfer Type	Surface
Graphics Controls	
Display Source Points	Off
Legend Controls	
Legend Range	Program Controlled
Minimum Source	Program Controlled
Maximum Source	Program Controlled

Figure 4:7 Static Structural Settings. Fixed Support and Import Data Properties

4.4 Solution

As the last step of the finite element analysis, we define the total deformation of specified micropillars as given in Figure 4:8. Results are obtained as shown in Figure 4:9. For our study, we simulated the cylindrical and square shaped micropillars with an inter-pillar spacing of 75 µm geometries.

Details of "Inlet Total Deformation"

Scope	
Scoping Method	Named Selection
Named Selection	InletPillar
Definition	
Type	Total Deformation
By	Time
Display Time	Last
Calculate Time History	Yes
Identifier	
Suppressed	No
Results	
Minimum	0. mm
P Maximum	2.8005e-003 mm
Average	1.2825e-003 mm
Minimum Occurs On	Solid
Maximum Occurs On	Solid
Minimum Value Over Time	
Minimum	0. mm
Maximum	0. mm
Maximum Value Over Time	
Minimum	6.3939e-004 mm
Maximum	2.8005e-003 mm
Information	
Time	1. s
Load Step	1
Substep	5
Iteration Number	11

Details of "Solution Information"

Solution Information	
Solution Output	Solver Output
Newton-Raphson Residuals	0
Identify Element Violations	0
Update Interval	2.5 s
Display Points	All
FE Connection Visibility	
Activate Visibility	Yes
Display	All FE Connectors
Draw Connections Attached To	All Nodes
Line Color	Connection Type
Visible on Results	No
Line Thickness	Single
Display Type	Lines

Figure 4:8 Solution Properties

With the finite element modelling done with Static Structural, the displacement of cylindrical and square micropillars with 3:1 aspect ratio and inter-pillar spacing of 75µm as a function of force per area is employed in order to provide an accurate prediction with the experimental setup. The Young’s Modulus found out from literature [58] is used. According to our experimental procedure, Young's Modulus is given specified as 1.5MPa. The simulation results show a spring constant of 0.18N/m for 25µm diameter and 75µm in length of micropillars.

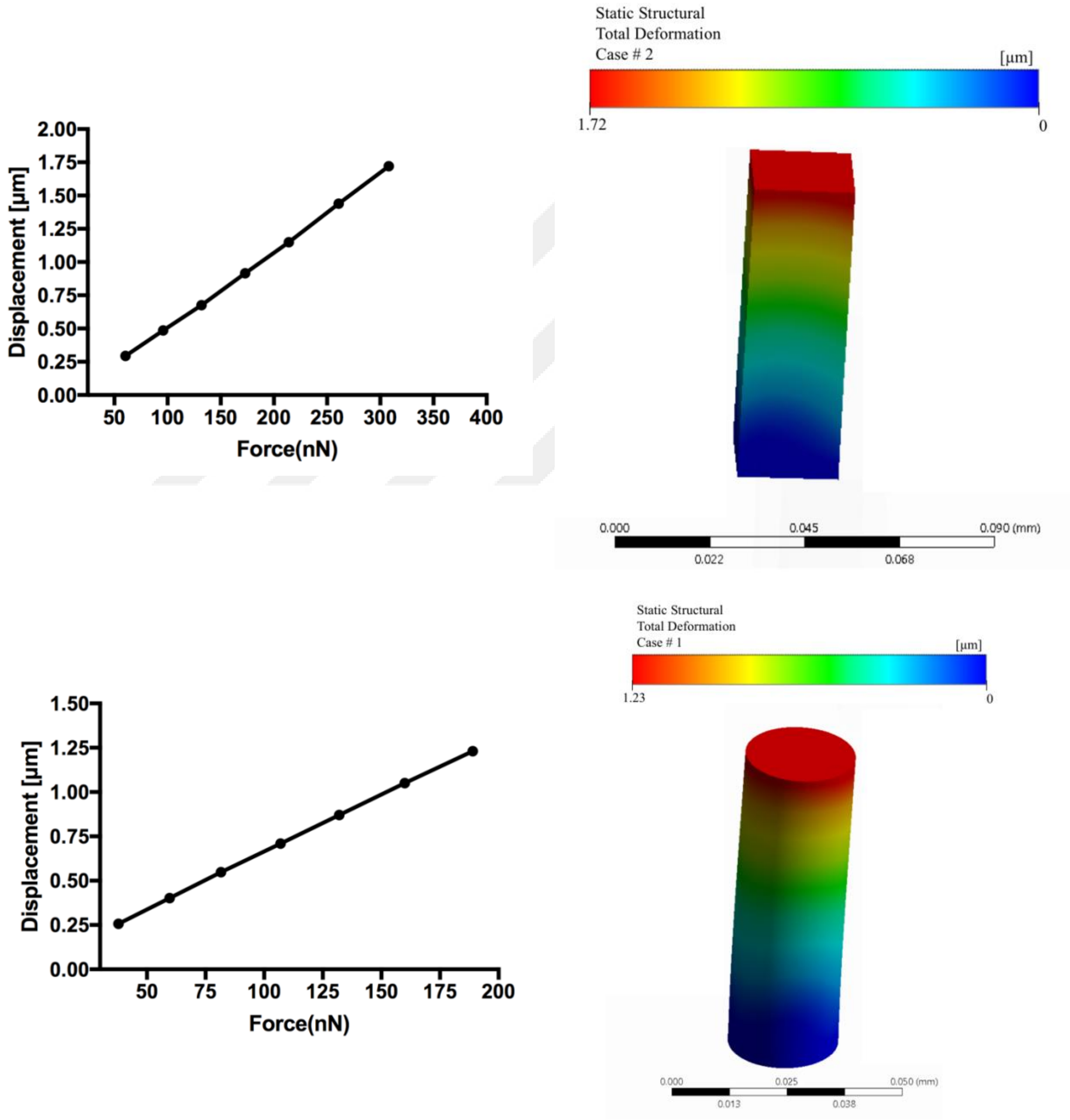

Figure 4:9 Force – Displacement Relationship and schematic of finite element analysis for square micropillars(top). Force – Displacement Relationship and schematic of finite element analysis for cylindrical micropillars(bottom) at 30ml/hr flow rates for 1 cP(water) fluid.

Chapter 5 METHODOLOGY

5.1 Fabrication Process

Within this chapter, the design, fabrication, and characterization of the PDMS micropillar based microchip for microfluidic applications are described. Fabrication process is designed accordingly to infrastructure and material that our Clean Room contains. The fabrication process contains two parts. The first part consists of the photolithography method and the second part is the soft lithography method that introduced by Whitesides[59]. The photolithography process is demonstrated in Figure 5:1 and the PDMS microfluidic chip preperation is shown in Figure 5:2.

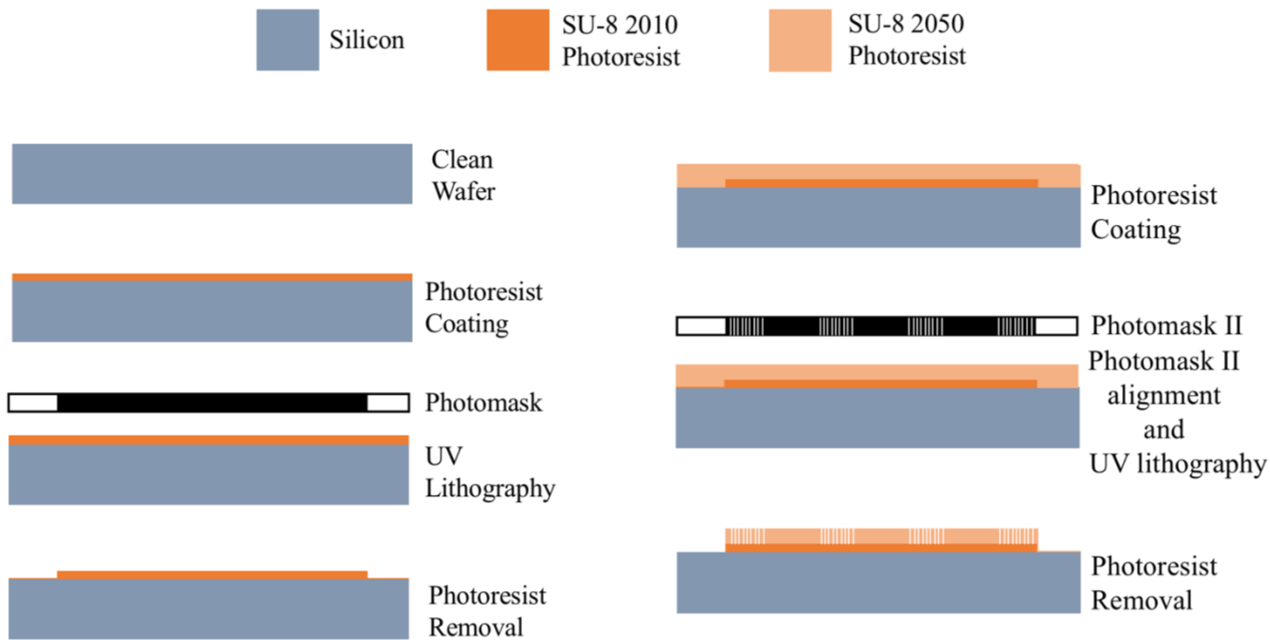

Figure 5:1 Fabrication Process Flow for Micropillar Arrays.

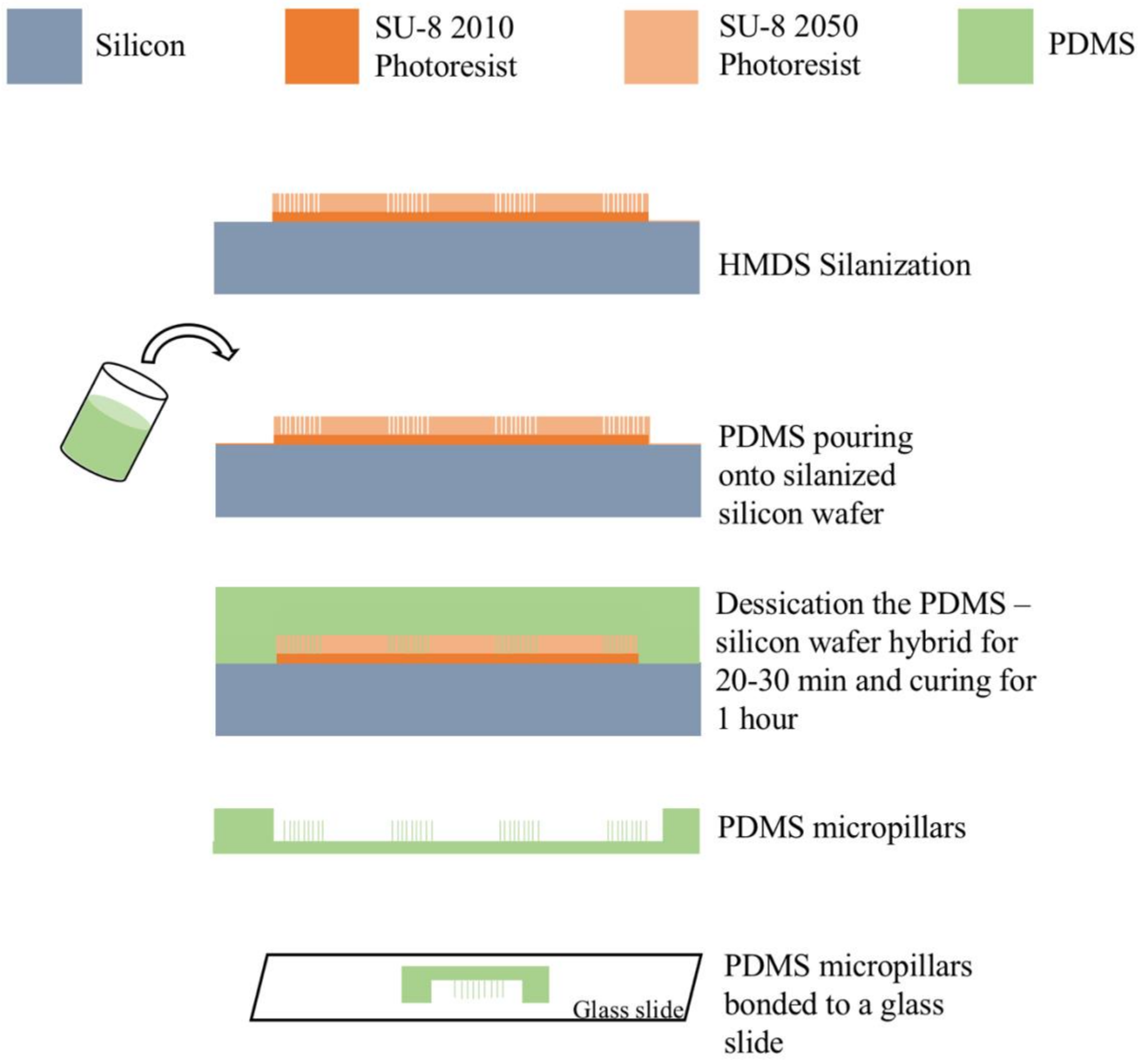

Figure 5:2 Soft Lithography Process Flow for PDMS Micropillar based Miflufluidic Chip.

5.2 Micropillar Array Fabrication

The first step of the fabrication process is UV lithography method where MEMS structure is patterned by using photoresist. For micropillar array structures, SU-8 negative photoresist was used. SU-8 is an epoxy-based negative photoresist. With SU-8 photoresist, an aspect ratio of 40 :1 and thickness of 2mm can be achieved. It is sensitive to 365nm and smaller wavelengths. In order to obtain 3:1 aspect ratio of micropillar arrays, this photoresist is selected. The patterning process is detailed in the Photolithography Section.

Photomask Design

48 equally-sized microchannels, varying in the pillar shape and inter-pillar spacing, were drafted by AutoCAD software (AutoDesk Inc., San Rafel, CA, USA) to fit on a 4-inch diameter silicon wafer.

The design requires two steps, and in the second step where the PDMS micropillars are bonded to a glass slide, they should not stick to the glass surface. For that reason, we designed two photomasks, one containing only the channels and the other mask contains the channels and micropillar structures. Photomasks were fabricated for this work using traditional mask fabrication techniques via laser etching of chrome-plated glass platform by Bilkent University, UNAM Facilities (Ankara, Turkey).

5.2.1 Photolithgraphy

Silicon Wafer Preparation

The master mold is patterned on a 4-inch diameter silicon wafer. At the beginning of the process, the wafer was cleaned with solvent cleaning method. Solvents can clean organic residues. However, acetone-like solvents leave their residues afterward. So that, a two-solvent method is needed. The wafer first dipped into the warm acetone bath (> 55ºC) for 10 minutes. Then placed into a container filled with IPA(2-propanol) for 5 minutes. The IPA cleaning followed by a rise with DI water. To be sure that all residuals of water are gone, the wafer placed onto a hot plate and dried for 20 minutes at 120ºC, then cooled down to room temperature.

SU-8 Negative Photoresist Coating

There are two SU-8 photoresists were used for this step. As the first step, only empty channels were patterned to the wafer. The first SU-8 coated is SU-8 2010, which allows the coating of thin layers to the surface. Coating requires 2 step spin coating procedure. Spin Coating procedure starts with a spin at 500 rpm for 10s with 100 rpm/s acceleration, then continues with spin at 3500 rpm for the 30s with 100 rpm/s acceleration. After spin coating, SU-8 coated wafer is soft-baked at 65ºC and 95ºC for 1min and 3min respectively in order to remove the excess solvent and prevent sticking. In the end, the wafer cooled down to the room temperature.

The second coating step starts with SU-8 2050, which allows the coating of thick layers. The procedure for SU-8 2050 again requires 2 step of spin coating. Spin Coating procedure starts with a spin at 500 rpm for the 30s with 100 rpm/s acceleration, then continues with spin at 1850 rpm for the 30s with 100 rpm/s acceleration. After spin coating, SU-8 coated wafer is soft-baked starting from 65ºC and gradually increased up to 95ºC, then waited for 12min in order to remove the excess solvent and prevent sticking. In the end, the wafer cooled down to the room temperature by gradually decreasing the temperature. As results of experiences with SU-8, we found out that the soft-bake is important for improving the adhesion; therefore, this soft bake process helps us to increase the adhesion of photoresist to the wafer surface.

The SU-8 is a viscous photoresist; therefore, at the end of the spin coating procedure, bead accumulation occurs at the edge of the wafer[24]. The SU-8 is a viscous photoresist; therefore, at the end of the spin coating procedure, bead accumulation occurs at the edge of the wafer. Bead accumulation at the edge blocks the mask from full contact with photoresist coated wafer and causes a gap which leads to diffraction in the UV Lithography[60]. Acetone dipped swap was used for removing the bead at the edge.

Photoresist Exposure – Patterning

For the first layer of SU-8 2010 photoresist, the exposure time found out to be 10s. As for the 80µm thick second layer coated with SU-8 2050, the optimum exposure time was 16s for the exposure process. When the exposure time is lower than 16s, adhesion and etching problems have occurred, and for higher exposure times, overexpose problem occurs. Post-bake step is also a critical step for the patterning of the SU-8 photoresist. The final structure is patterned in this step. In the post-bake, the wafer is baked starting from 65ºC and gradually increased up to 95ºC, then waited for 7min, similar to soft-bake. Post bake has the same effect on adhesion as the soft-bake.

There is an alignment step in the exposure procedure. This process is used for creating a gap between the micropillars and the top surface by using the second mask (Photomask II). In the proposed design of a microfluidic chip, we have a gap size of 5-10µm. Since we could not achieve this gap with a more straightforward method, we proposed a two mask fabrication flow in order to obtain the 5µm gap between the micropillars and the top surface. Figure 5:1 shows the alignment procedure. With the help of the alignment marks that designed and printed on both masks, the Photomask II is aligned with the wafer.

Alignment marks on both masks were designed with the same sizes so that they match without a problem when the second mask is aligned on top of the second layer. When the alignment marks match with each other, whole wafer and structure would be aligned.

We encountered many difficulties in the patterning of SU-8. The major problem is the T-profile[61]. T-profile occurs when the mask and the wafer has a gap when the need to be in full contact with each other. When there is a gap in between, it directs to diffraction in the UV light. Consequently, the SU-8 holes do not go beyond the determined depth and an outcast cure of the wells occured. In order to solve this problem, the edge bead occurred in the spin coating step is removed, and the gap between the mask and the wafer is optimized.

Development (Removal of the Photoresist)

In order to remove the unexposed SU8 from the wafer surface, SU8 Developer was applied to the wafer. In order to get deep and clean wells inside the film, we put the SU-8 Developer filled petri dish inside an ultrasonic liquid bath for 10min intervals. After each period of sonication, the SU8 Developer was renewed, to complete removal of residual of unexposed SU-8.

Hard Bake and Silanization

After developing, the patterned wafer was placed on a hot-plate for 1 hour at 150ºC to hard-bake the SU8. The master template that contains the micropillar wells on the silicon wafer was permitted to cool down to room temperature after 1 hour.

Before proceeding with the second step of fabrication, the master mold should be silanized in order to render the surface of SU-8 wells hydrophobic. As the silanization chemical, we used HMDS(Hexamethyldisilazane), Sigma 999973. The silanization process carried out for 20 minutes inside a vacuum desiccator. The silanized master mold is used in the second step of fabrication with PDMS.

5.2.2 PDMS based Micropillar Array Fabrication

SYLGARD® 184 Elastomer Kit from Dow Corning was used for PDMS mixture. PDMS was mixed with 10:1 base: cross-linker ratio. After mixing, in order to remove the bubbles, the mixture of PDMS was degassed under vacuum for 1 hour. The degassed PDMS was poured onto the surface of the SU-8 master mold and degassed for 30 minutes in order to remove remaining bubbles and make sure that the PDMS goes deep enough to the SU-8 wells. After desiccation, the PDMS-covered wafer inserted in the oven for one hour at 75°C. After one hour, excess PDMS was delicately cut around the wafer edge using a scalpel. Then before separating the PDMS from SU-8 mold, ethanol was poured onto the surface and desiccated for 20 minutes.

After the separation of PDMS, 1.25 mm diameter holes were punched to make inlets for the sample fluid and an outlet for waste of the fluid. The final PDMS piece was attached to a glass slide using an Oxygene Plasma device.

The micropillars were fabricated with diameter range of 25–30 µm, height between 75–90 µm and spacing of 25–75 µm. The aspect ratio of the micropillars fabricated is 3:1. For cylindrical micropillars the diameter and heigh is 25 µm and 75 µm respectively. As for the square micropillars the diameter and heigh is 30 µm and 90 µm respectively. The accurate results of fabricated micropillars were obtained via scanning electron microscopy (SEM). The Figure 5:3 shows the SEM images of 3:1 aspect ratio cylindrical micropillars. And Figure 5:4 shows the 3:1 aspect ratio square micropillars.

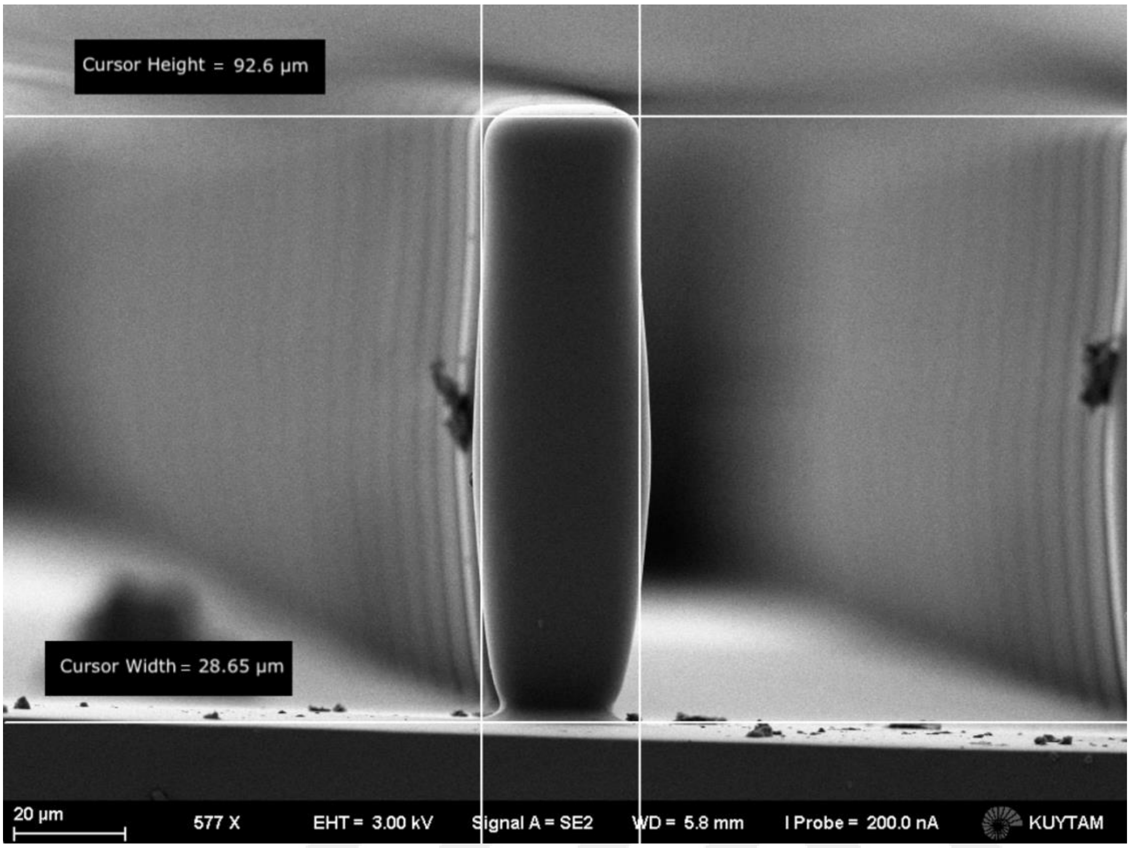
Cursor Height = 92.6 µm
Cursor Width = 28.65 µm
20 µm
577 X
EHT = 3.00 kV
Signal A = SE2
WD = 5.8 mm
I Probe = 200.0 nA
KUYTAM

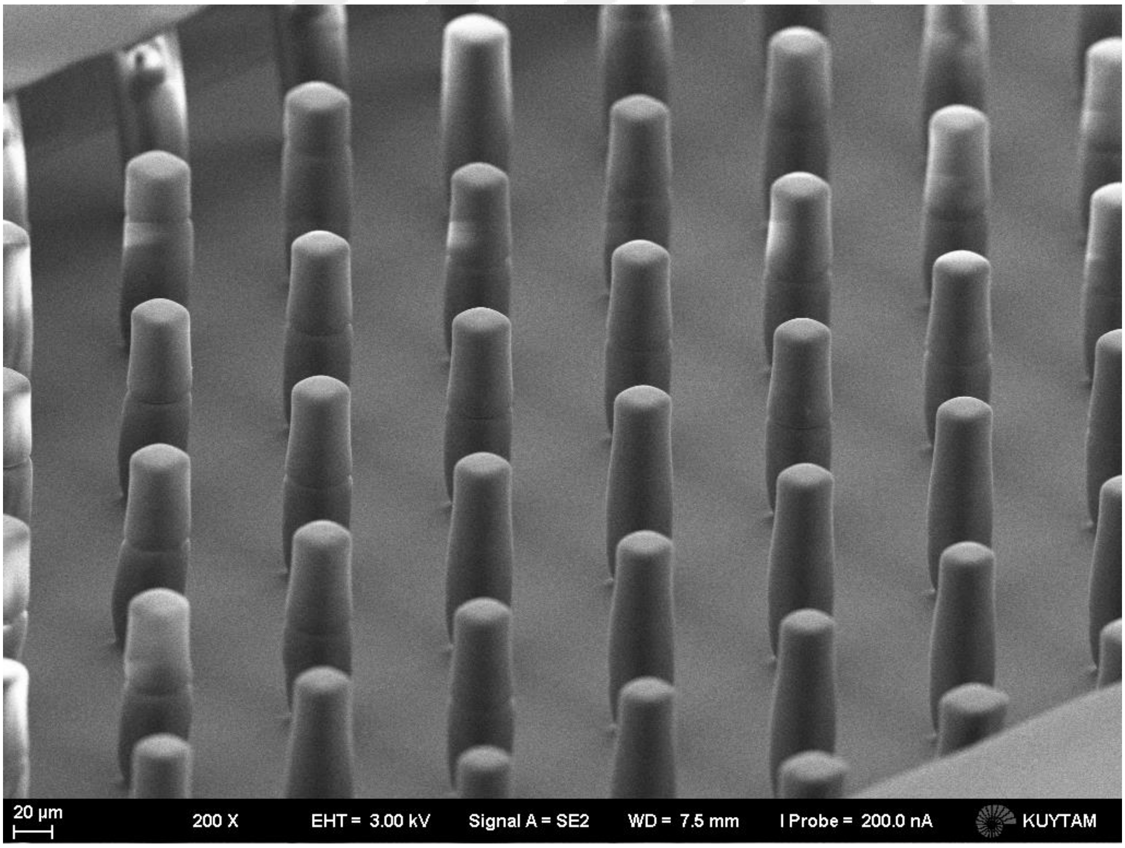
20 µm
200 X
EHT = 3.00 kV
Signal A = SE2
WD = 7.5 mm
I Probe = 200.0 nA
KUYTAM

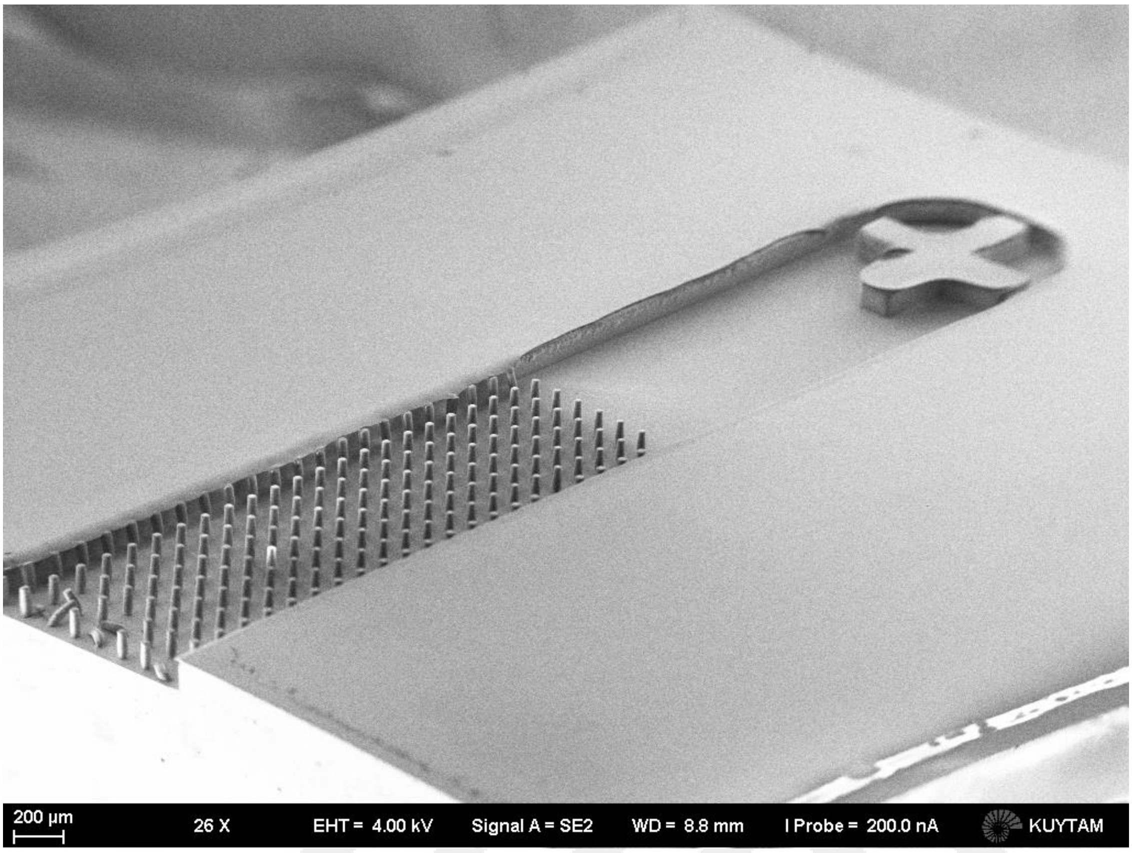

Figure 5:3 SEM images of square micropillars.

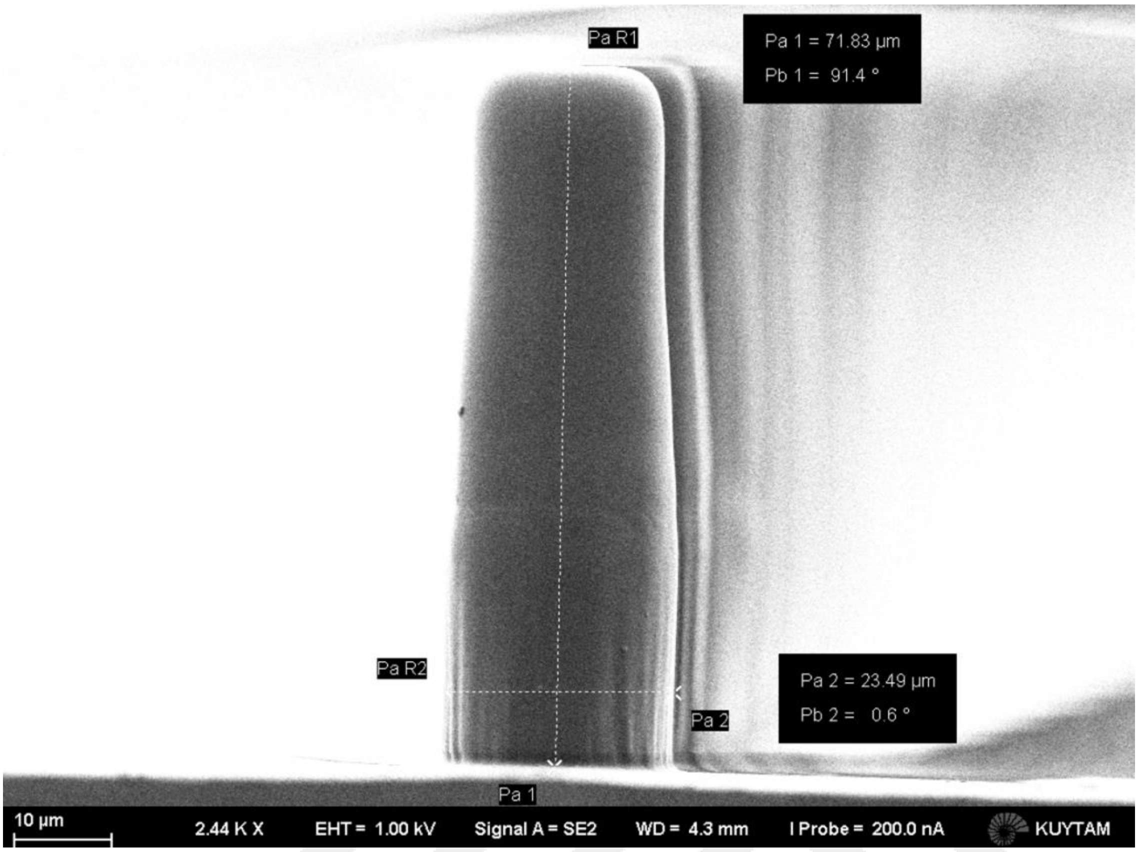
Pa R1
Pa 1 = 71.83 µm
Pb 1 = 91.4 °
Pa R2
Pa 2
Pa 2 = 23.49 µm
Pb 2 = 0.6 °
Pa 1
10 µm
2.44 K X
EHT = 1.00 kV
Signal A = SE2
WD = 4.3 mm
I Probe = 200.0 nA
KUYTAM

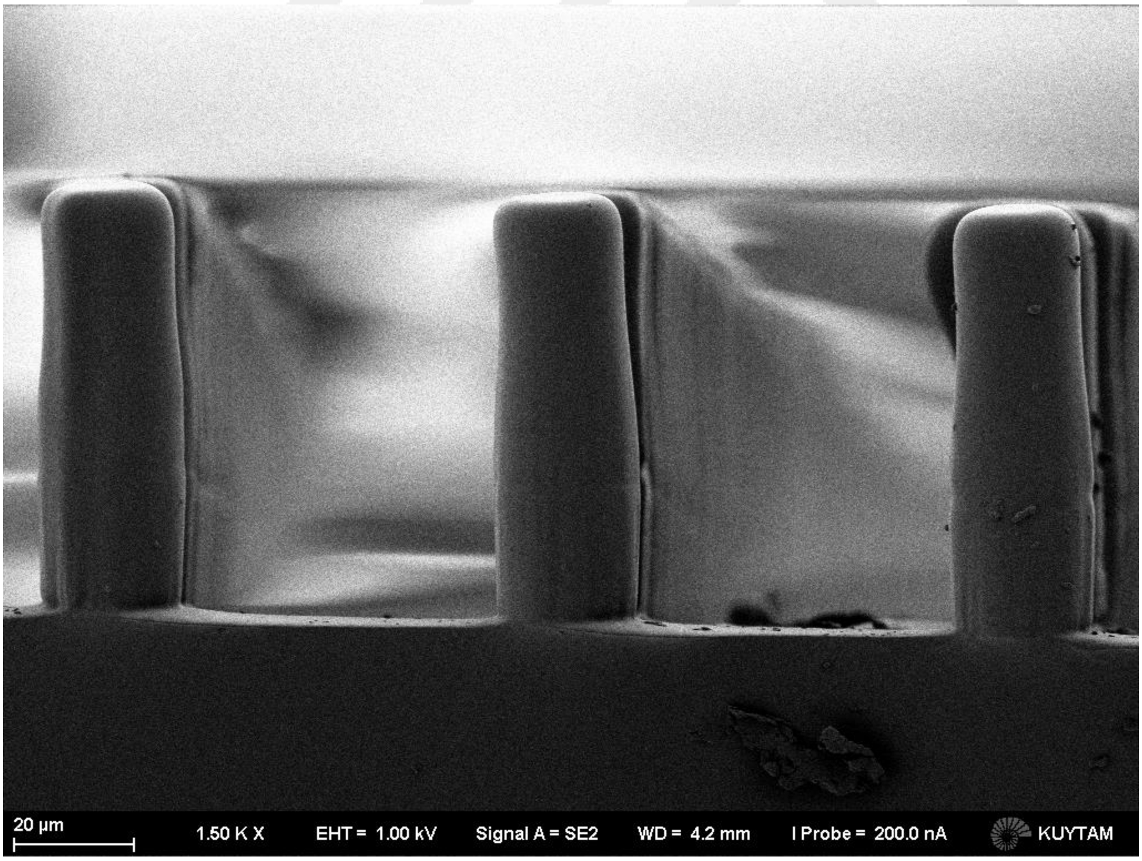
20 µm
1.50 K X
EHT = 1.00 kV
Signal A = SE2
WD = 4.2 mm
I Probe = 200.0 nA
KUYTAM

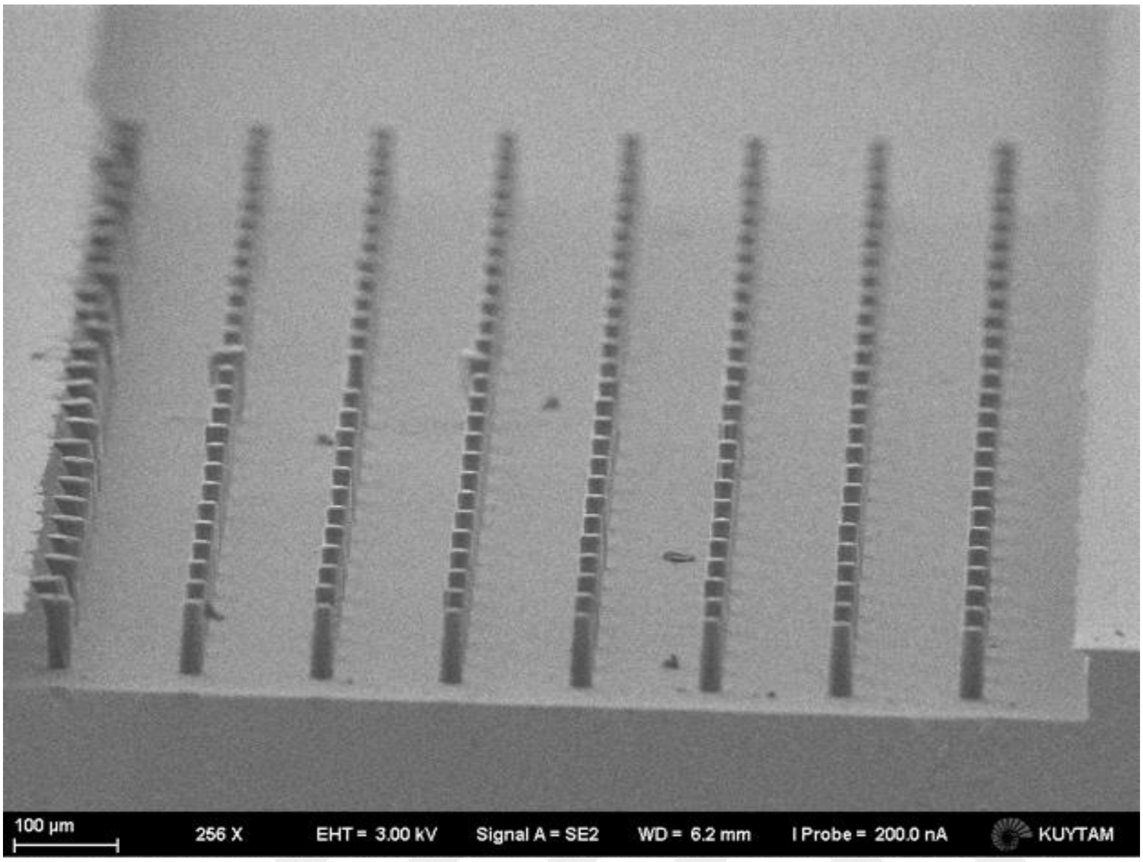

Figure 5:4 SEM images of cylindrical micropillars.

Chapter 6 EXPERIMENTAL SETUP

The measurement of viscosity using micropillars is based on determining the deflection of these micropillars as fluids of different viscosities flow through the microfluidic chip. Fluids flowing through the microfluidic device interacts with the micropillars resulting in their deflection, typically proportional to the viscosity of the fluid. We initially determine average micropillar de-flection at a given flow rate using standard glycerol/water mixtures for various viscosities. For this purpose, micropillars were imaged continuously as the sample fluid flows inside the device and interacts with the micropillars. These images were later analyzed using semi-automated analyze method to determine micropillar deflection.

The experimental setup (Figure 6.1) consists of a microfluidic chip, a microscope (Nikon Eclipse TS100), a syringe pump (33DDS, Harvard Apparatus), a computer and a high-speed camera (Grasshopper3, Point Grey). The sample fluid is injected into the microfluidic chip using the syringe pump. The microfluidic device is initially filled with the sample fluid. The images of micropillars within the microfluidic device are acquired under no flow condition (static) as well as at various flow rates (dynamic). The micropillar deflection is subsequently determined by analyzing images using the semi-automated analysis method.

The microfluidic chip that on the microscope stage was observed with 10X objective focused on the pillar tips. A syringe filled with sample fluid, placed on syringe pump and when the fluid starts to flow, the high-speed camera (FlyCap 2, PT Grey) recorded the experiments. The video recording mode set to M-JPEG with 25% compression and 24 frames per second (fps). Flow rates (30 mL/hr-150 mL/hr +15) used in the experiments were given in syringe pump with infuse mode and 15 seconds of running time. When the flow settled down in the microfluidic channel, the video recording started for static images (2-3 seconds), then the pre-adjusted syringe pump started for dynamic images and captured images until the infusion of syringe pump ends. The process repeated with same channel three times, and all the experiments for different samples and flow rates later analyzed.

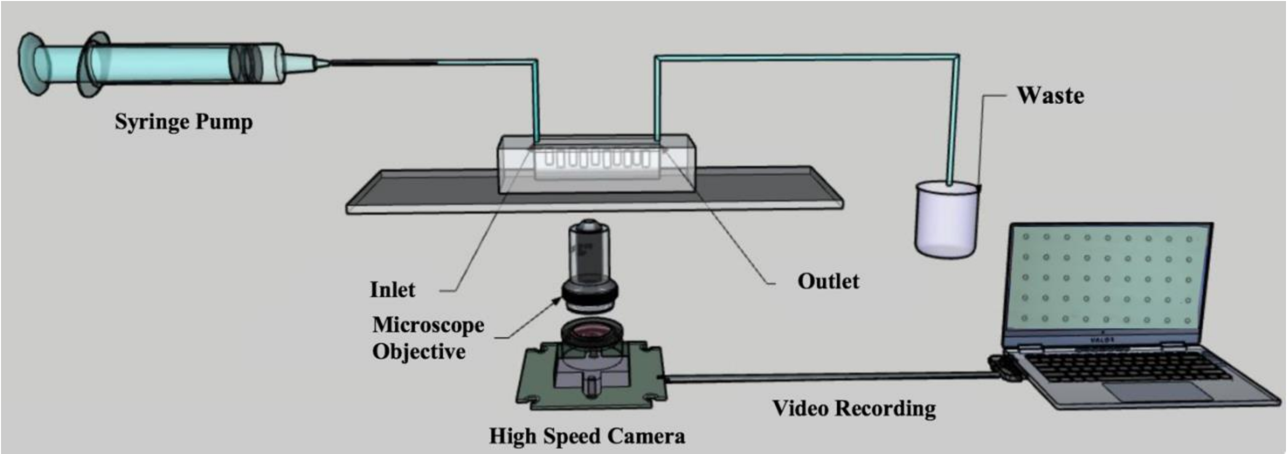

Figure 6:1 3D illustration of experimental setup. Syringe Pump system for sample infusion; microfluidic chip for micropillar deformation tracking; microscope, high-speed camera and computer system for visual observation and record acquisition.

6.1 Image Analysis

In this study, an analytical method similar to image algorithms based on visualization of moving objects has been applied in order to determine the movements of micropillars in the microfluidic system quantitatively. The image processing algorithms initially used to quantitatively detect the movement of micropillars based on the fluid flow in the cartridge is Adobe After Effects (AAFx) system. Acquisition records are transferred to the analysis computer, the record taken in this image forming system is divided into frames by the AAFx system. After selecting the region of interest (ROI) where the micropillars located on the static image, the ROI is tracked in each dynamic image. AAFx track the motion in the coordinate system, ROI coordinates in x and y recorded for each frame. The coordinate data extracted to excel, and the change of the location for each frame calculated according to the following equation:

$$\text{Displacement}^2 = (x_d - x_s)^2 + (y_d - y_s)^2$$

Equation 6:1 – Micropillar Displacement Calculation

Where x_d is the dynamic x coordinate at a certain frame, x_s is the static x coordinate at first frame, y_d is dynamic y coordinate at a certain frame, and y_s is the static y coordinate at first frame. The displacements were calculated in pixels. By converting pixels to micron, with taking account of the lens magnifier (10X) and de-magnifier(0.7X) c-mount, a stage micrometer image was captured, and the conversion constant calculated.

For evaluating the validity of this method, manual substitutions with Image J were calculated and compared. In this manual and semi-automated measurement system comparison, the recordings were divided into frames, the first frame (static image) being excluded, and 20 frames (dynamic image) randomly selected among the frames. The micropillar of the static frame is selected and the surrounding of micropillar is colored. Then, the same micropillar is selected in dynamic images, and the micropillar colored different then the static image color. The static and dynamic images overlaid with transparency. This procedure is shown in Figure 6:2. Micropillar displacement is determined according to the change of center and compared with the semi-automated AAFx method. The comparison is given in Figure 6:3.

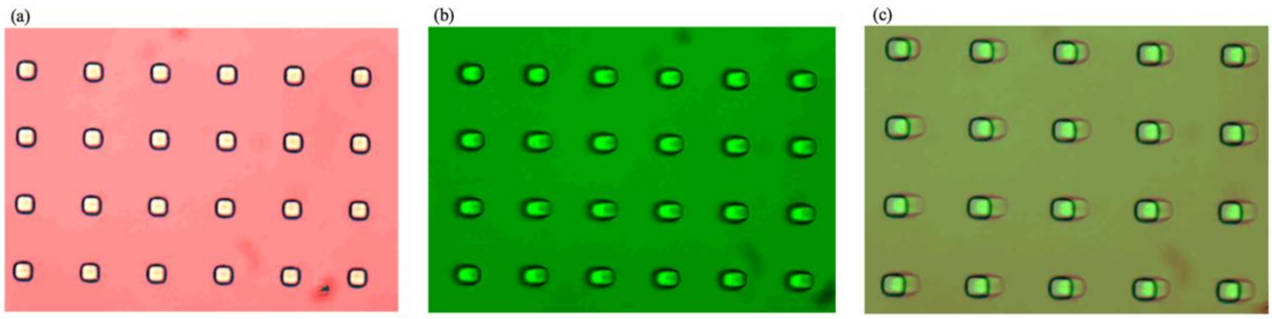

Figure 6:2 The displacement calculations done with Adobe After Effects program. (a) static micropillar location. (b) dynamic location of micropillar based on the displacement. (c) overlaid static and dynamic images, total displacement calculation.

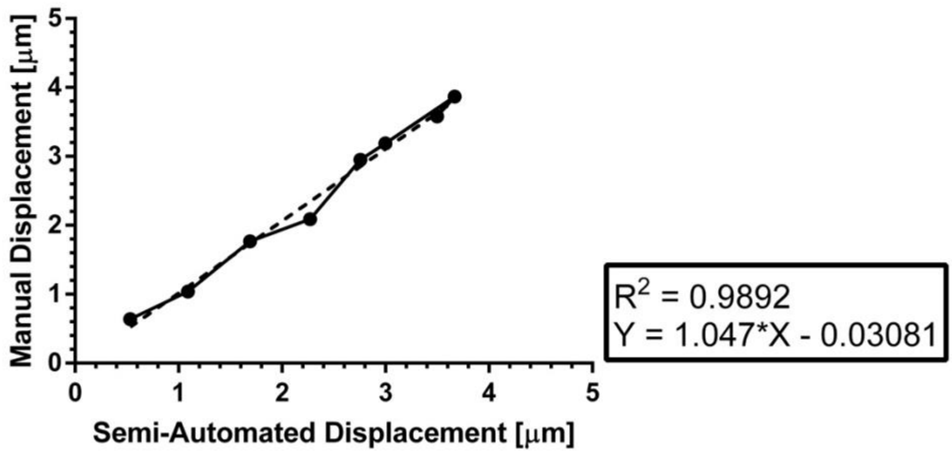

Figure 6:3 Manual (Image J) and semi-automated AAFx displacement analysis methods comparison.

Chapter 7 FINDINGS AND DISCUSSION

The case studies that solved with finite volume method are defined in Table 3:2. These case studies were simulated in order to determine the effects of the micropillar shape and inter-pillar spacing on the flow characteristics. The first case study is based on a regular cylindrical micropillars designed mostly used in cell mechanobiology studies in literature[19, 62-66]. Results for the pressure, wall shear stress and velocity streamlines along the channel for 50µm inter-pillar spacing in 1cP viscosity solution with 90ml/hr flow rate are shown in Figure 7:1.

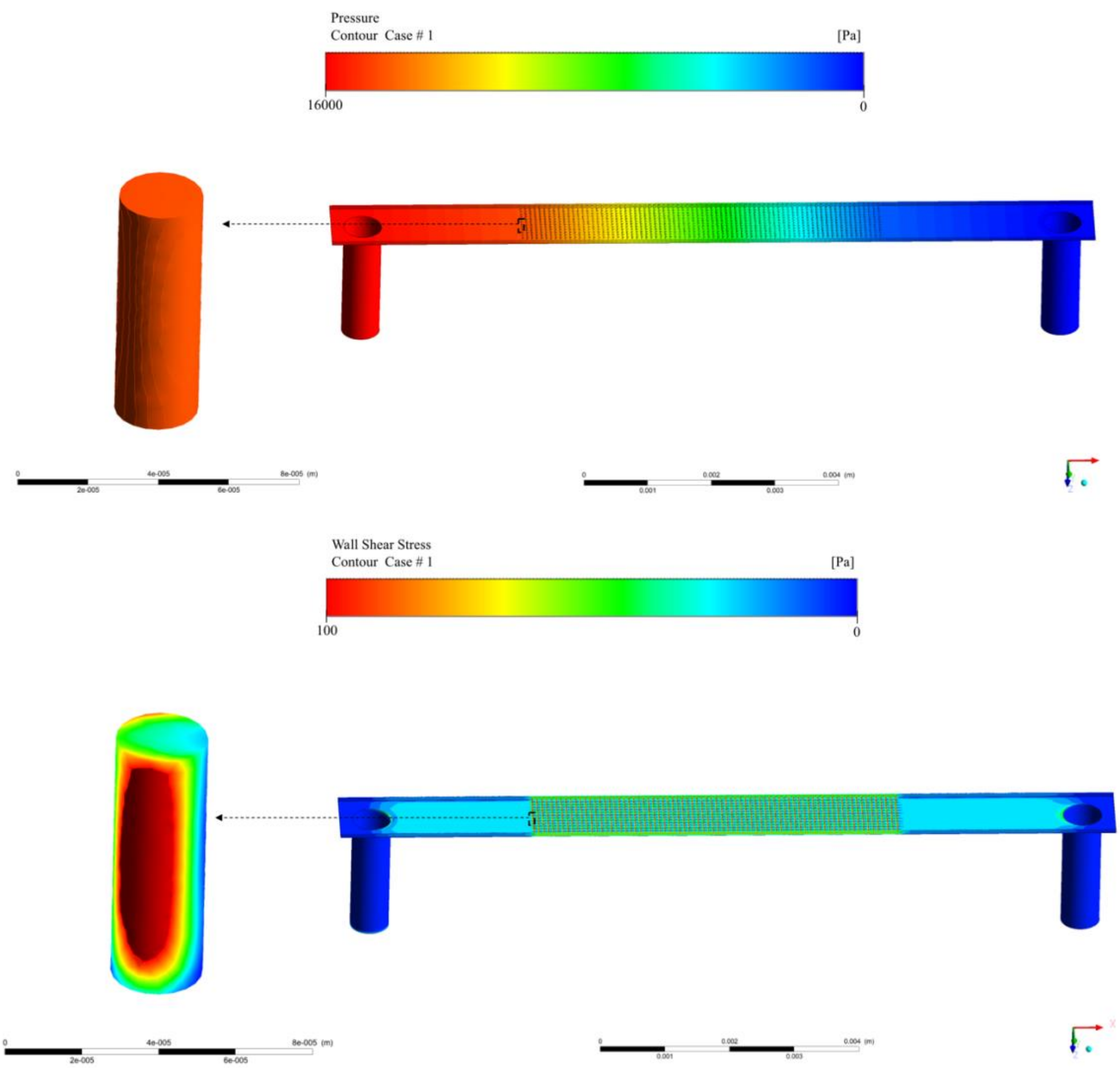

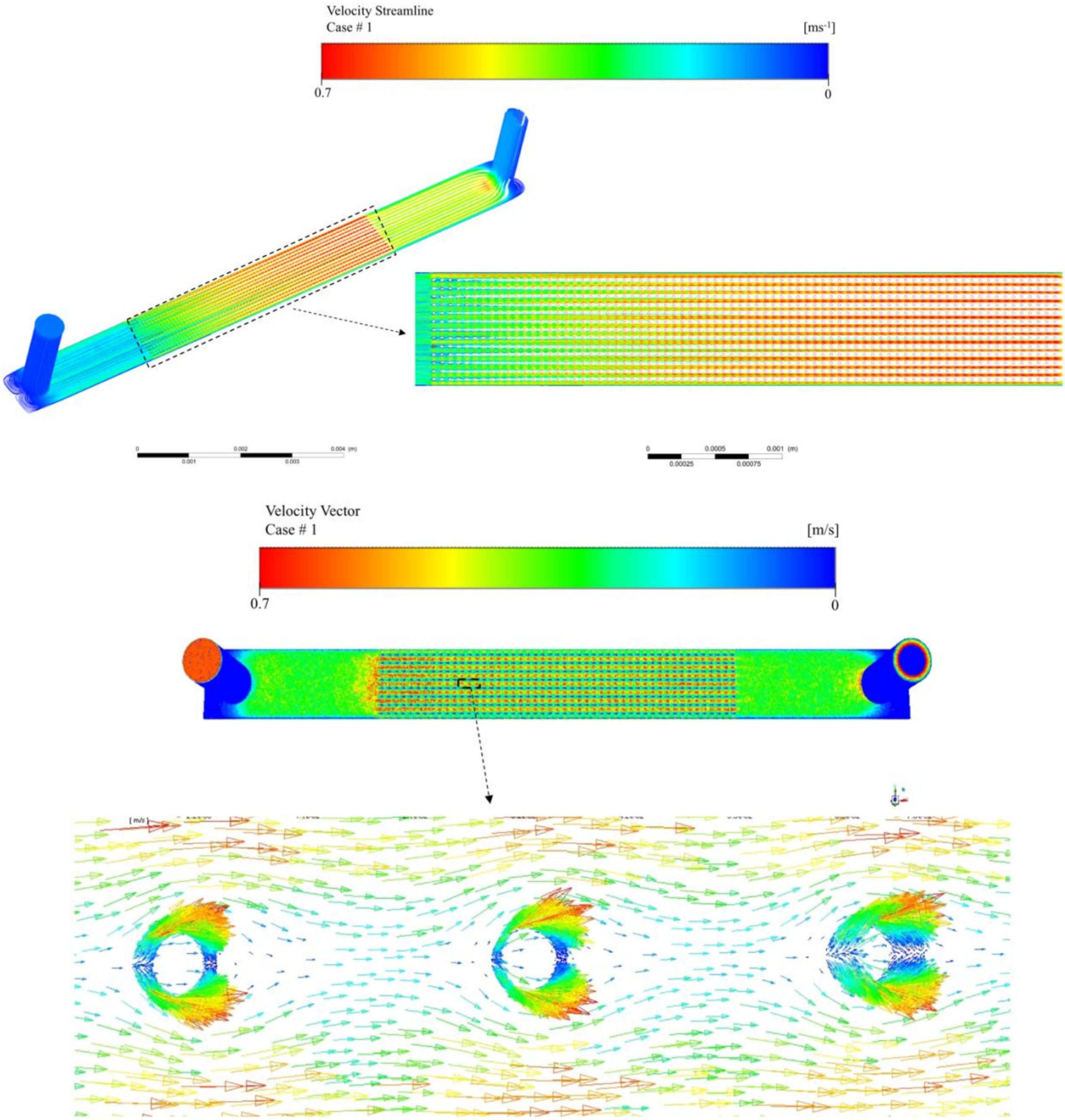

Figure 7:1 Contours of pressure and wall shear stress and the streamline of velocity vector of Case Study #1 (Cylindrical micropillars), 50µm inter-pillar spacing channel, 1cP viscosity solution with 90ml/hr flow rate.

As for the blood flow of the 50µm inter-pillar spacing channel with 90ml/hr flow rate results are shown in Figure 7:2.

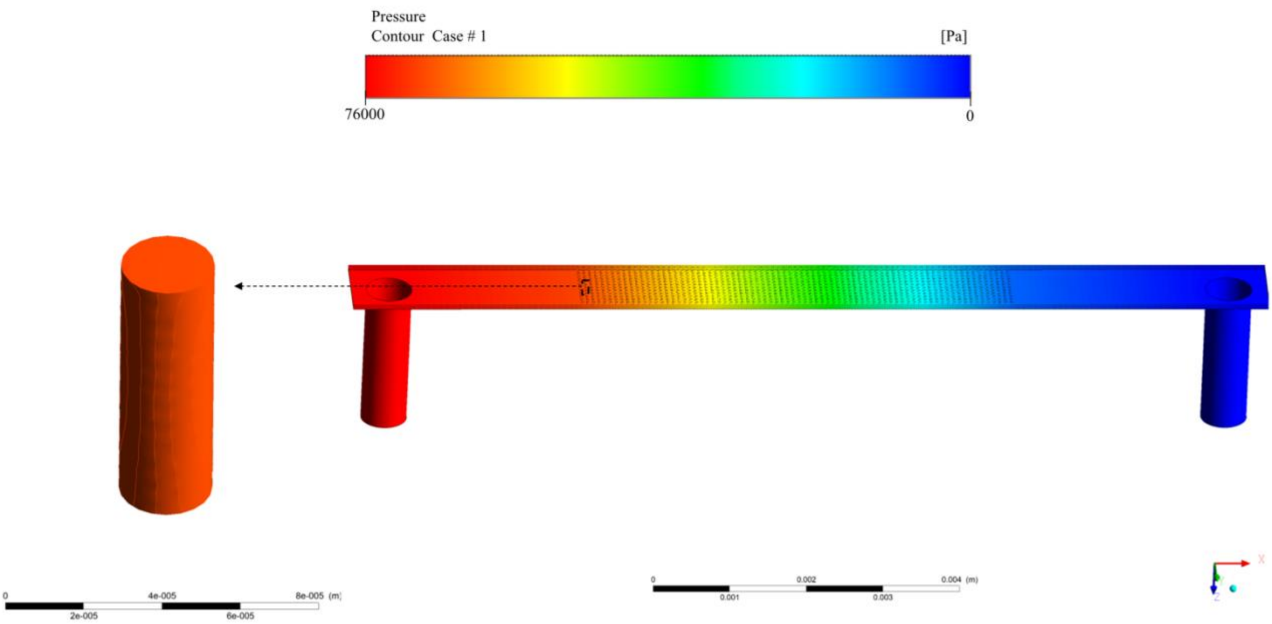
Pressure
Contour Case # 1
[Pa]
76000
0

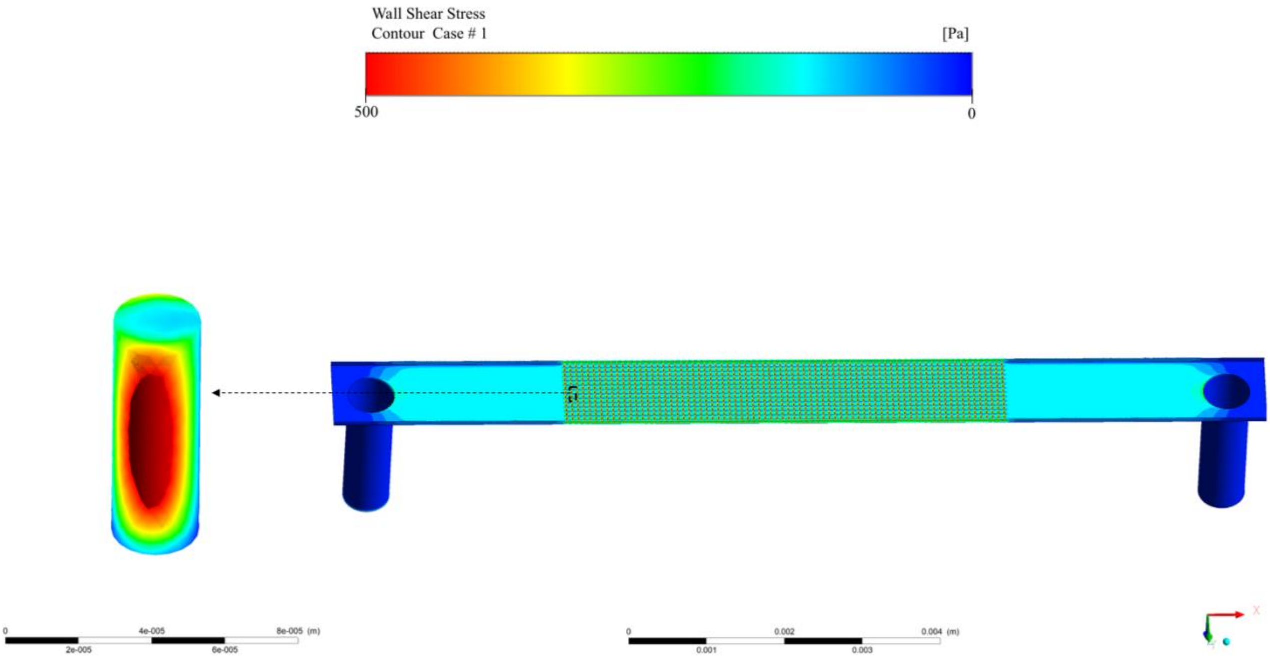
Wall Shear Stress
Contour Case # 1
[Pa]
500
0

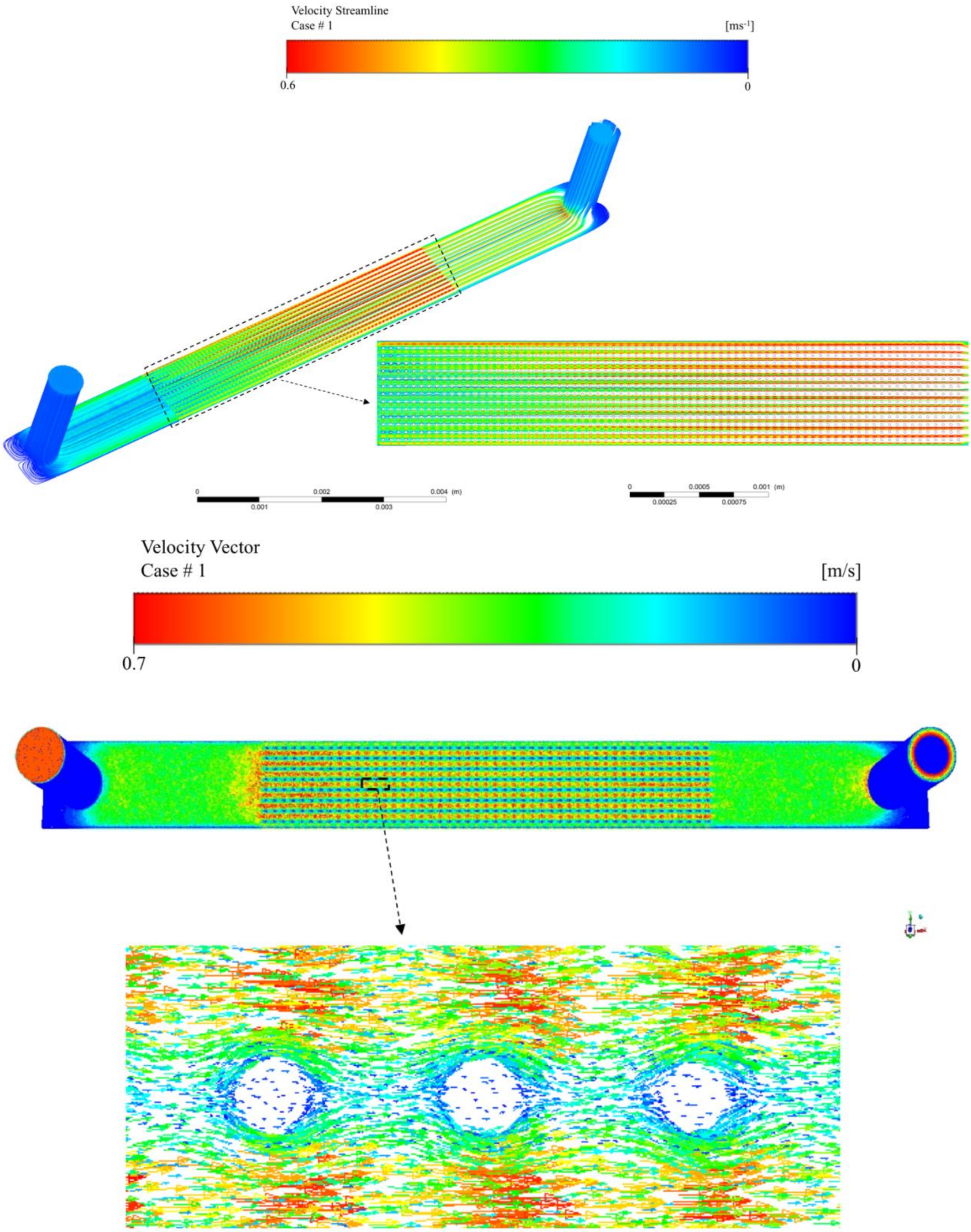

Figure 7:2 Contours of pressure and wall shear stress and the streamline of velocity vector of Case Study #1 (Cylindrical micropillars), 50μm inter-pillar spacing channel, blood flow (Casson model) with 90ml/hr flow rate.

The Case Study #2, is based on the square micropillar shapes that are used for mostly cell rolling dynamics and cell culture studies found in literature[67-69]. Results for the pressure, wall shear stress and velocity streamlines along the channel for 50µm inter-pillar spacing in 1cP viscosity solution with 90ml/hr flow rate are shown in Figure 7:3.

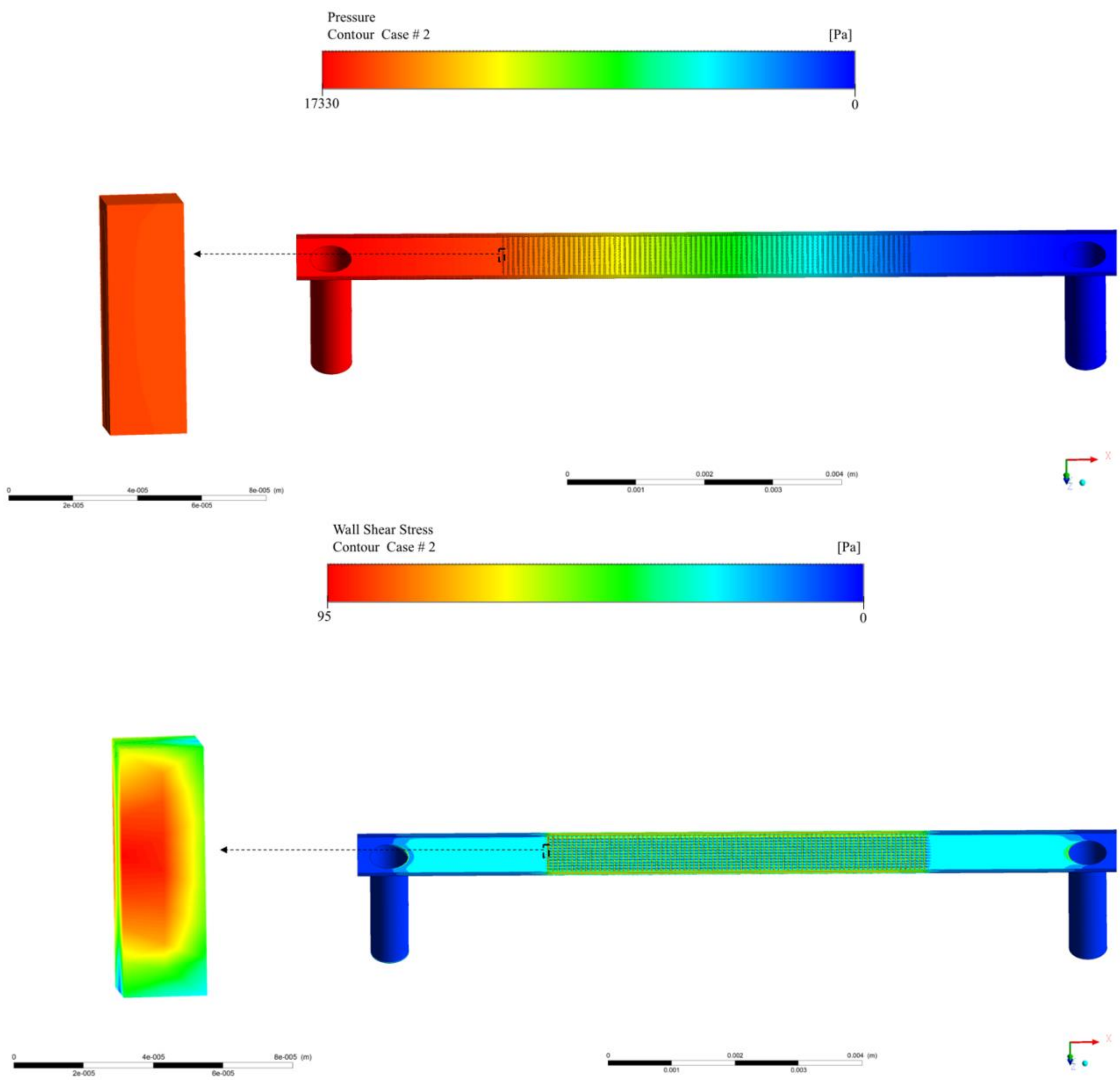

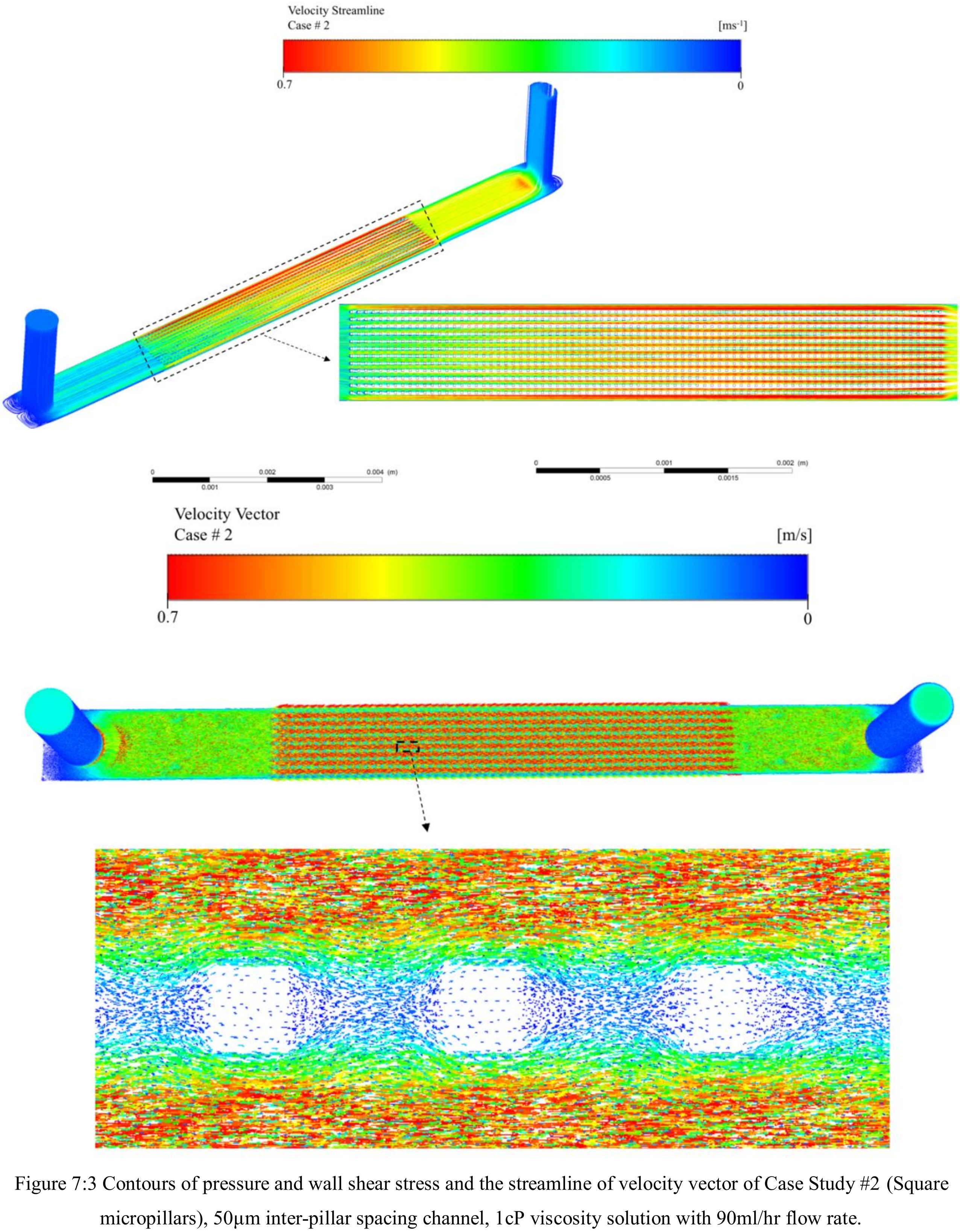

Figure 7:3 Contours of pressure and wall shear stress and the streamline of velocity vector of Case Study #2 (Square micropillars), 50μm inter-pillar spacing channel, 1cP viscosity solution with 90ml/hr flow rate.

The blood flow of the 50µm inter-pillar spacing channel with 90ml/hr flow rate of the Case study #2 results are shown in Figure 7:4.

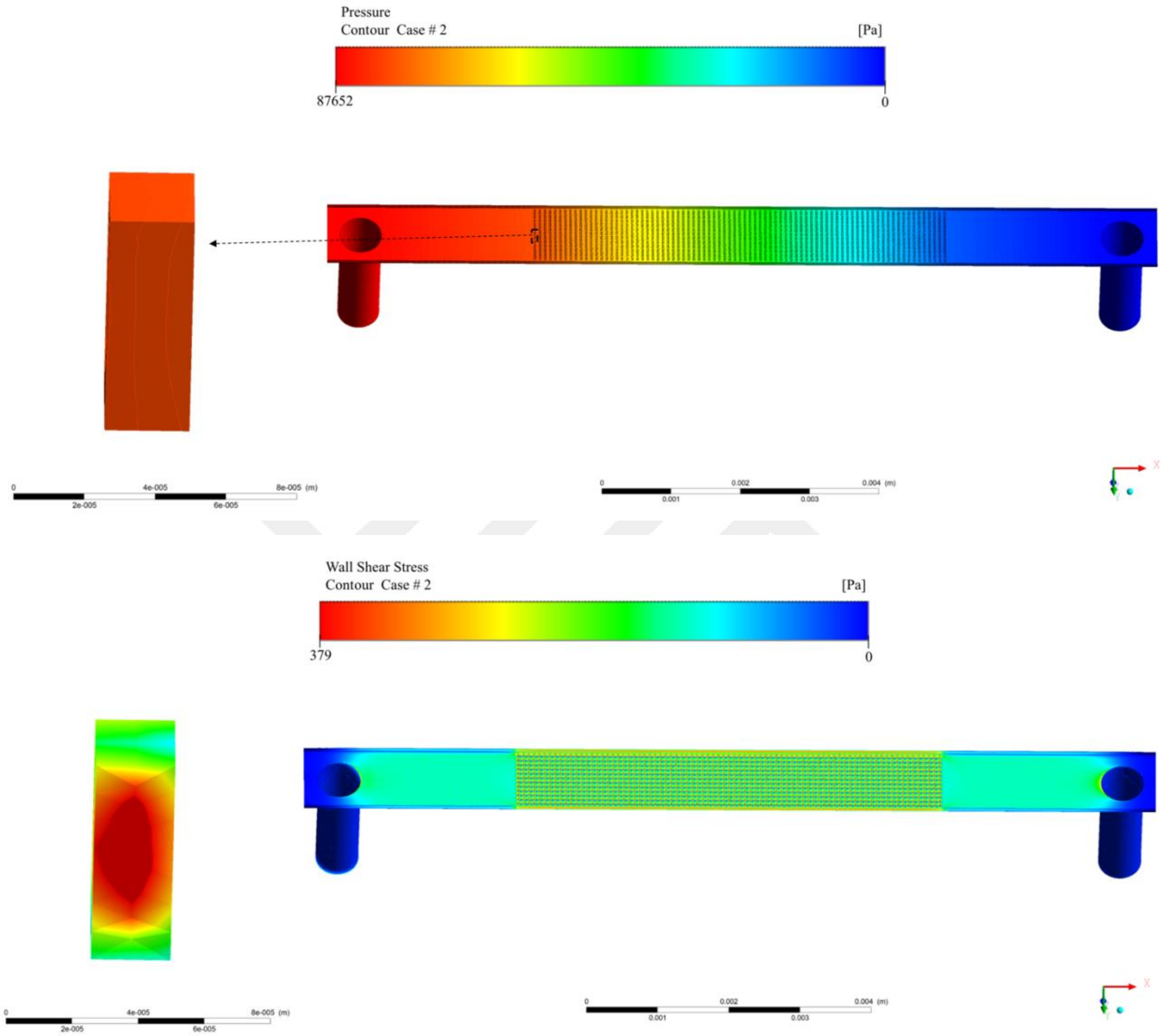

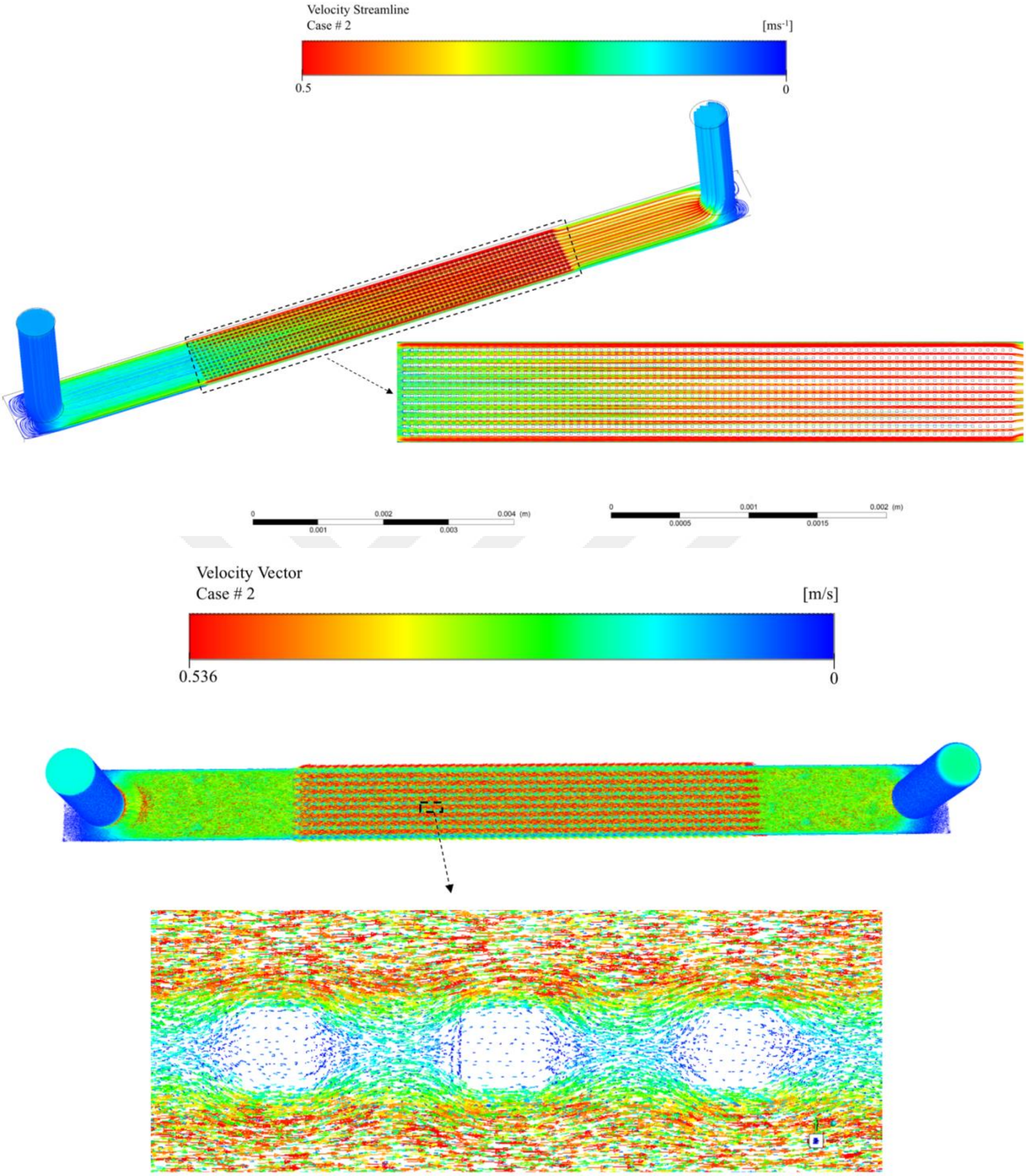

Figure 7:4 Contours of pressure and wall shear stress and the streamline of velocity vector of Case Study #2 (Square micropillars), 50μm inter-pillar spacing channel, blood flow (Casson model) with 90ml/hr flow rate.

Case Study #3, is based on the diamond micropillar shapes. Results for the pressure, wall shear stress and velocity streamlines along the channel for 50μm inter-pillar spacing in 1cP viscosity solution with 90ml/hr flow rate are shown in Figure 7:5.

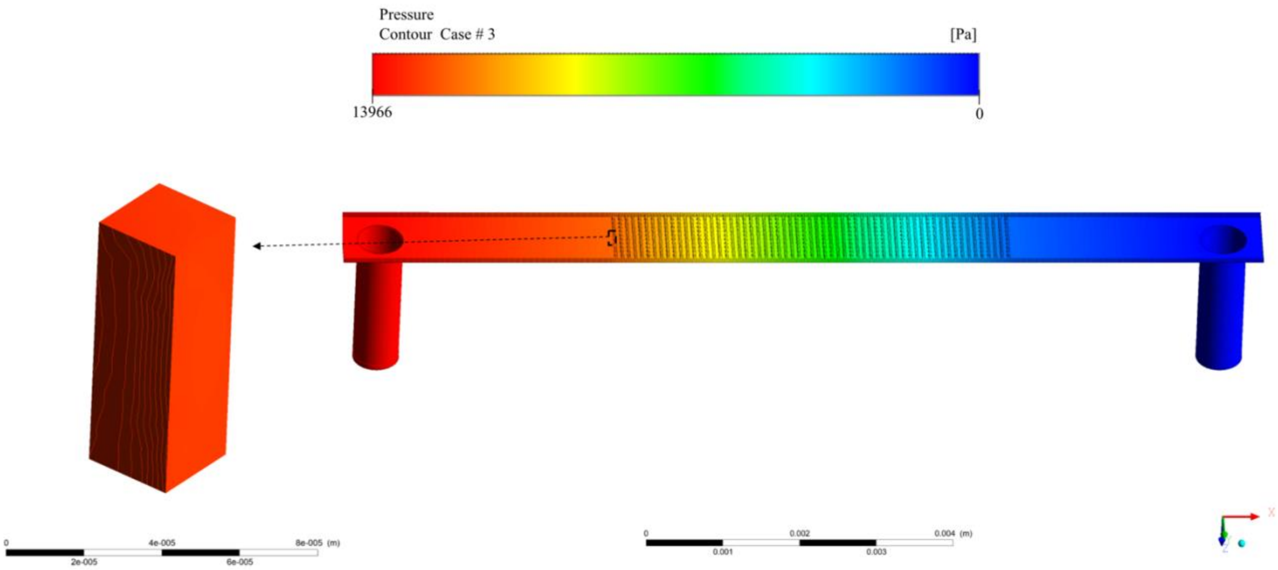
Pressure
Contour Case # 3
[Pa]
13966
0

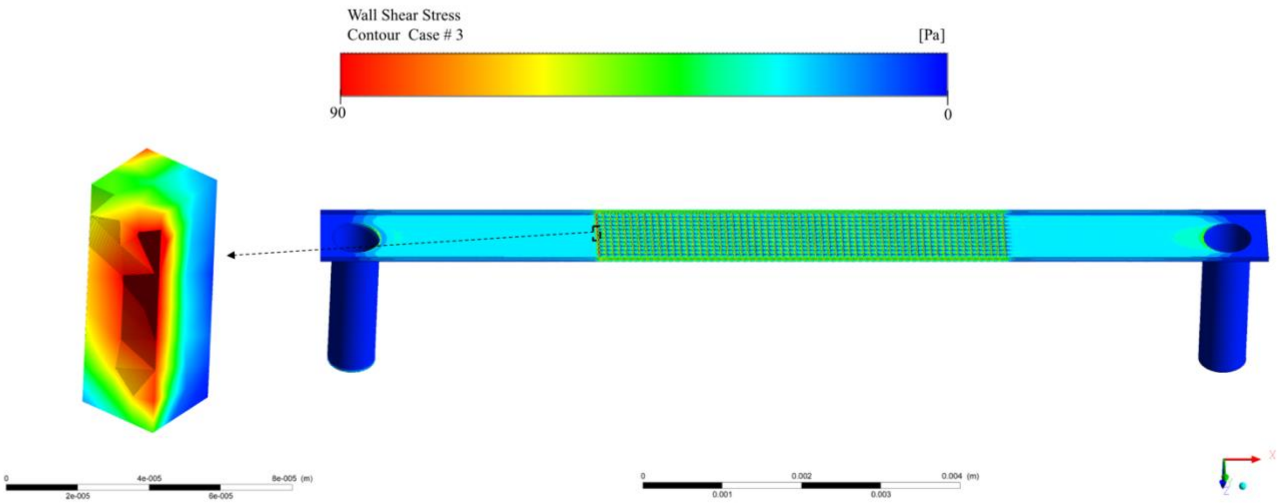
Wall Shear Stress
Contour Case # 3
[Pa]
90
0

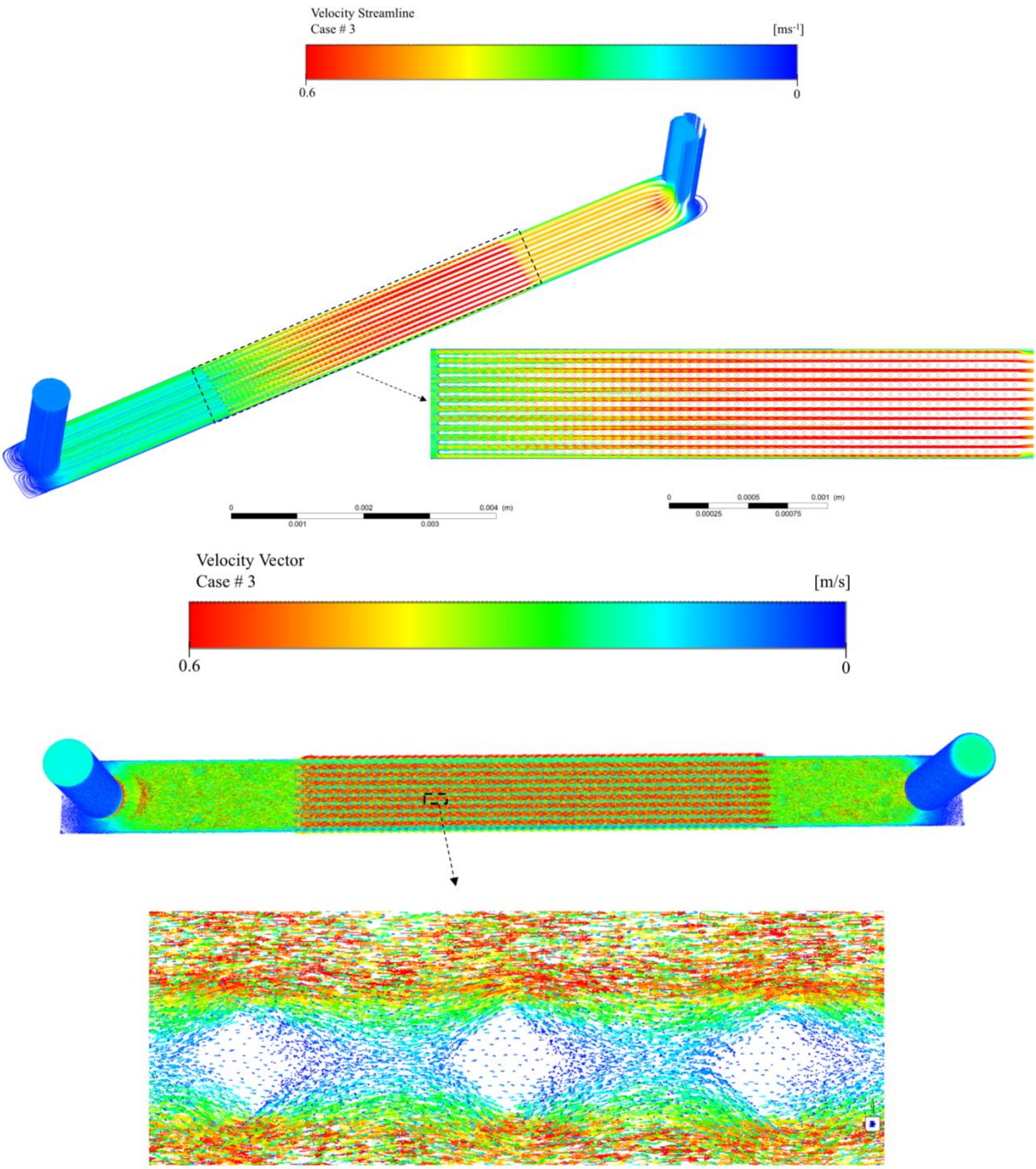

Figure 7:5 Contours of pressure and wall shear stress and the streamline of velocity vector of Case Study #3 (Diamond micropillars), 50µm inter-pillar spacing channel, 1cP viscosity solution with 90ml/hr flow rate.

The results of the Casson model flow of the 50µm inter-pillar spacing channel with 90ml/hr flow rate of the Case study #3 results are shown in Figure 7:6.

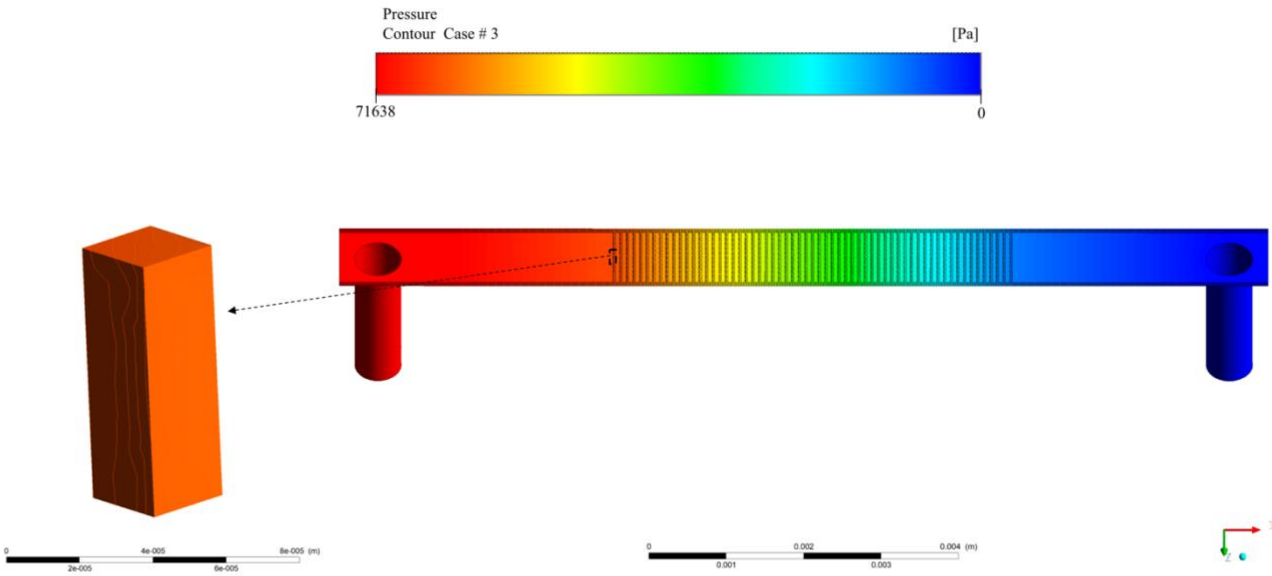

Pressure
Contour Case # 3
[Pa]
71638
0
0
4e-005
8e-005 (m)
2e-005
6e-005
0
0.002
0.004 (m)
0.001
0.003
X
Z

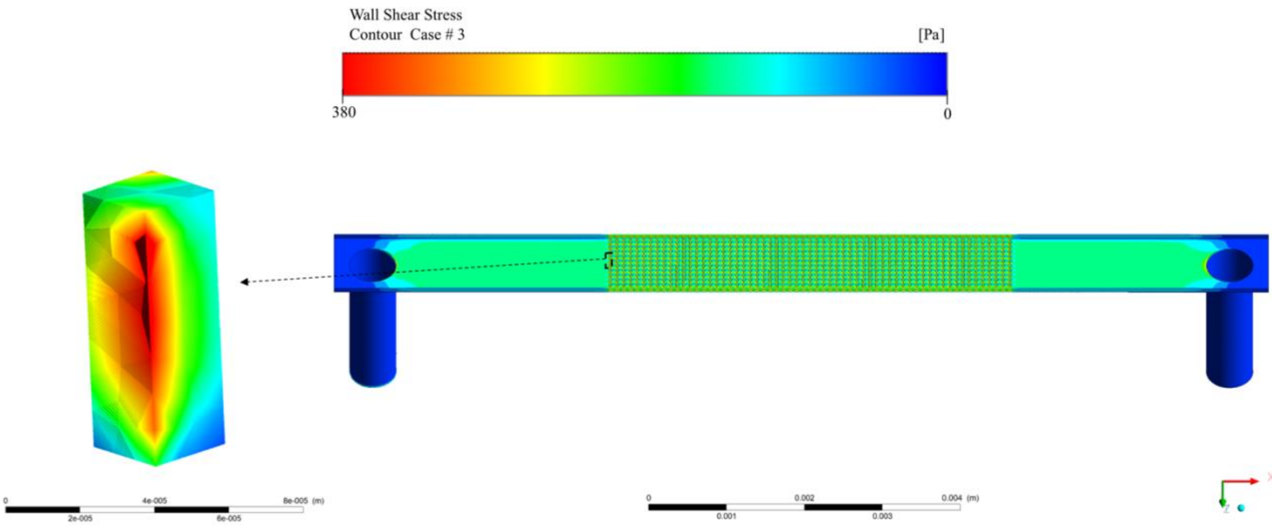

Wall Shear Stress
Contour Case # 3
[Pa]
380
0
0
4e-005
8e-005 (m)
2e-005
6e-005
0
0.002
0.004 (m)
0.001
0.003
X
Z

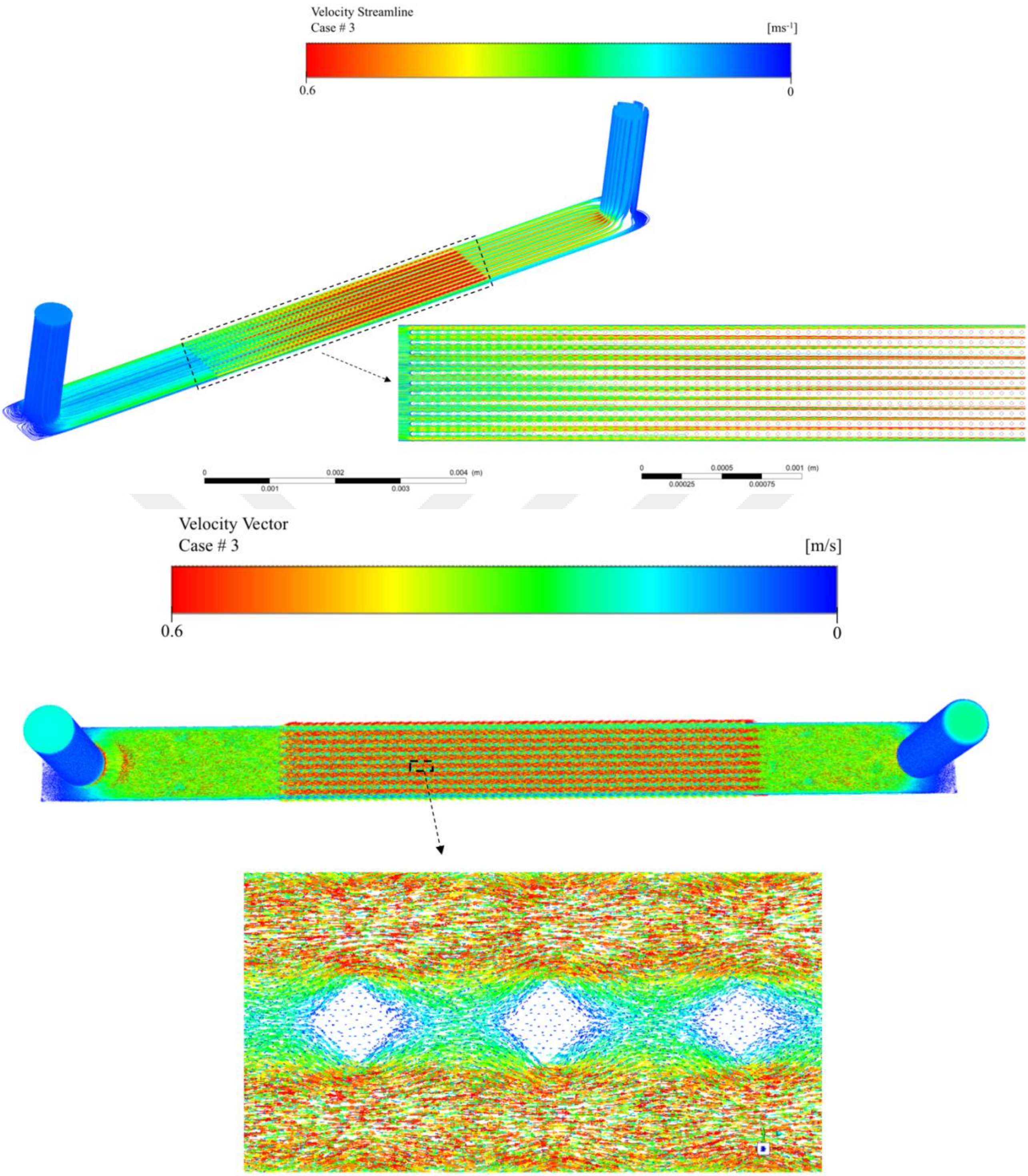

Figure 7:6 Contours of pressure and wall shear stress and the streamline of velocity vector of Case Study #3 (Diamond micropillars), 50µm inter-pillar spacing channel, blood flow (Casson model) with 90ml/hr flow rate.

The last Case Study, is based on the triangle micropillar shapes. We designed the diamond and triangle shaped micropillars in order to observe the sharp edge effect on the flow characteristics[70]. Results for the pressure, wall shear stress and velocity streamlines along the channel for 50μm inter-pillar spacing in 1cP viscosity solution with 90ml/hr flow rate are shown in Figure 7:7.

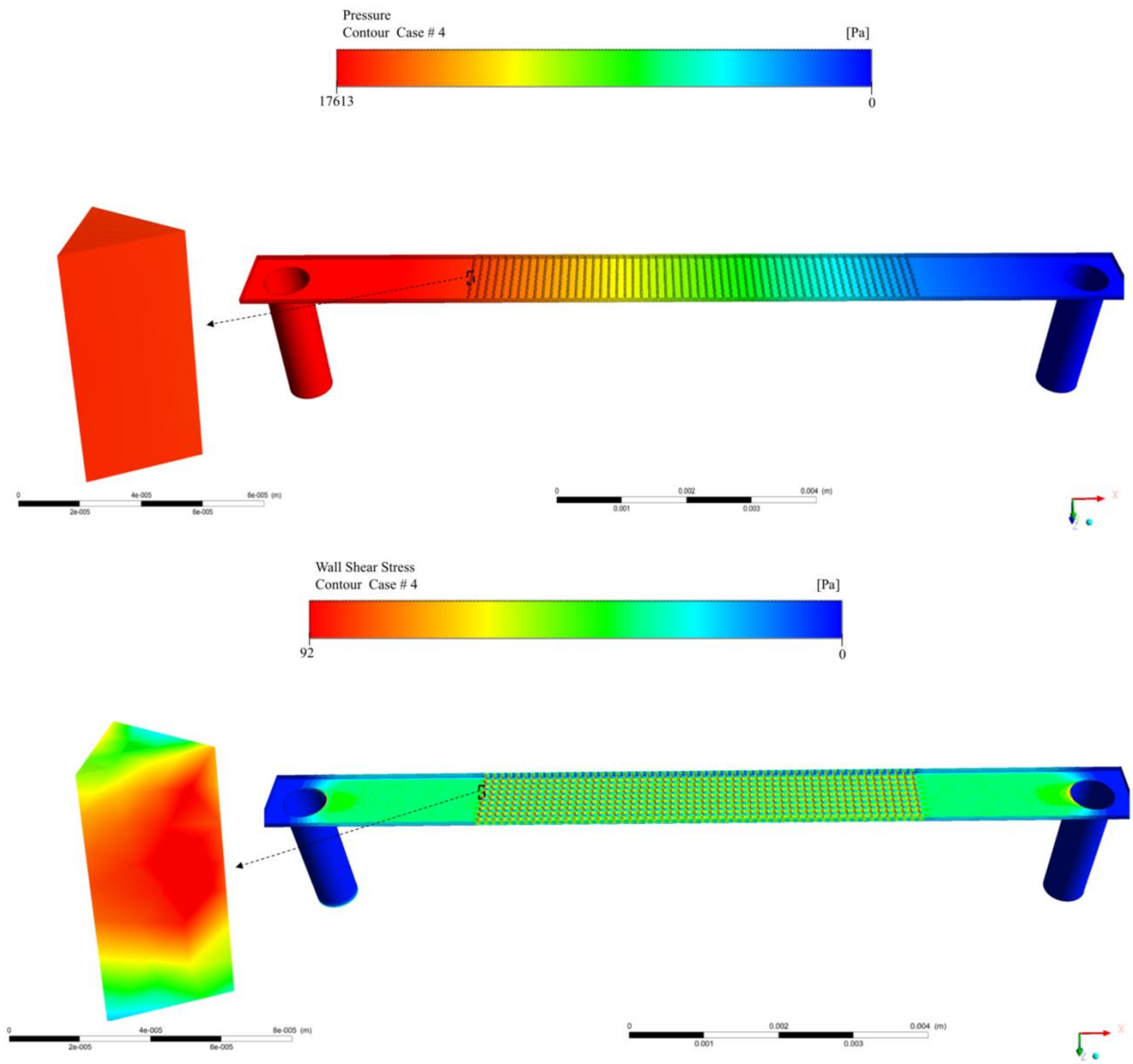

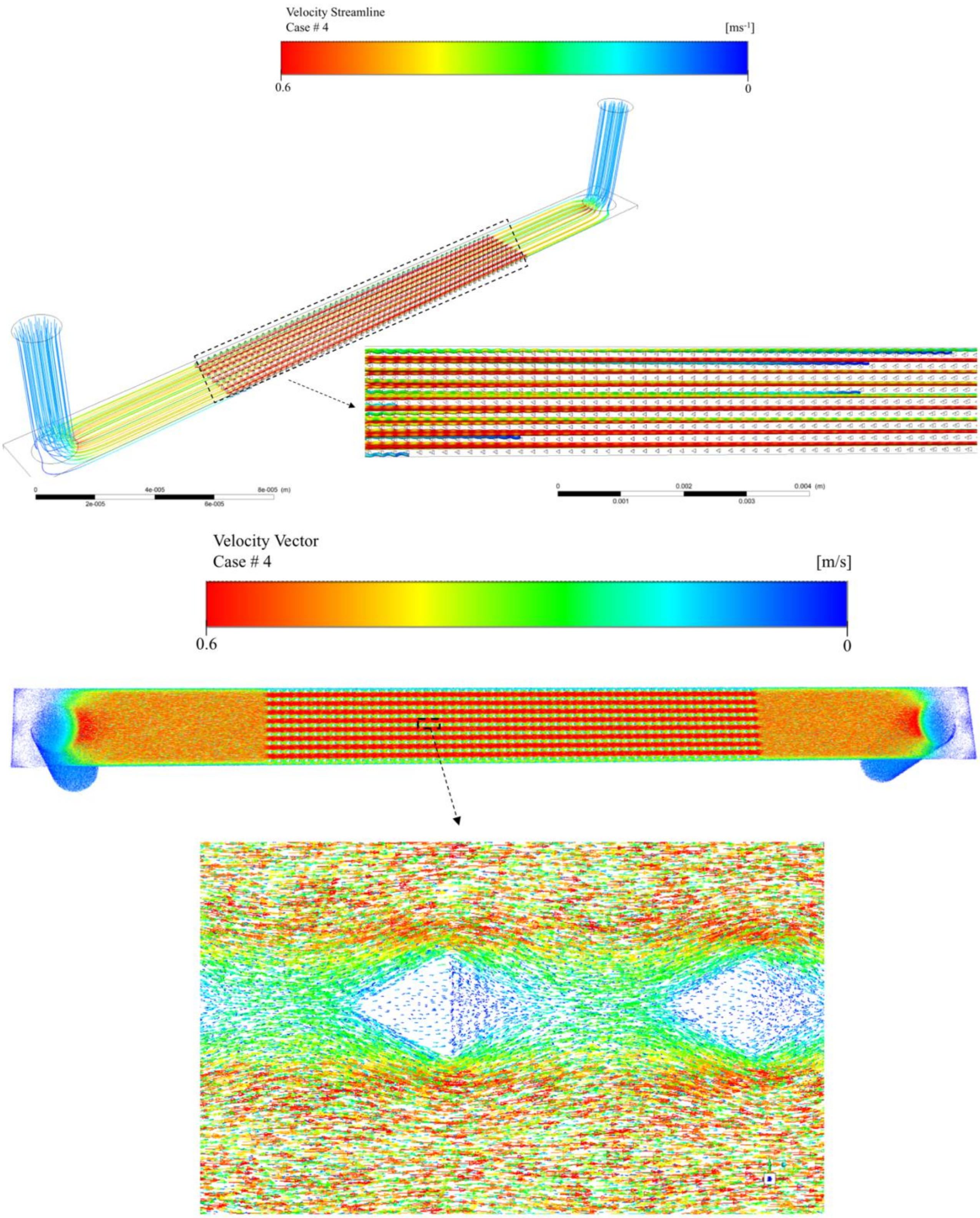

Figure 7:7 Contours of pressure and wall shear stress and the streamline of velocity vector of Case Study #4 (Triangle micropillars), 50μm inter-pillar spacing channel, 1cP viscosity solution with 90ml/hr flow rate.

The results of the Casson model flow of the 50μm inter-pillar spacing channel with 90ml/hr flow rate of the las case study results are shown in Figure 7:8.

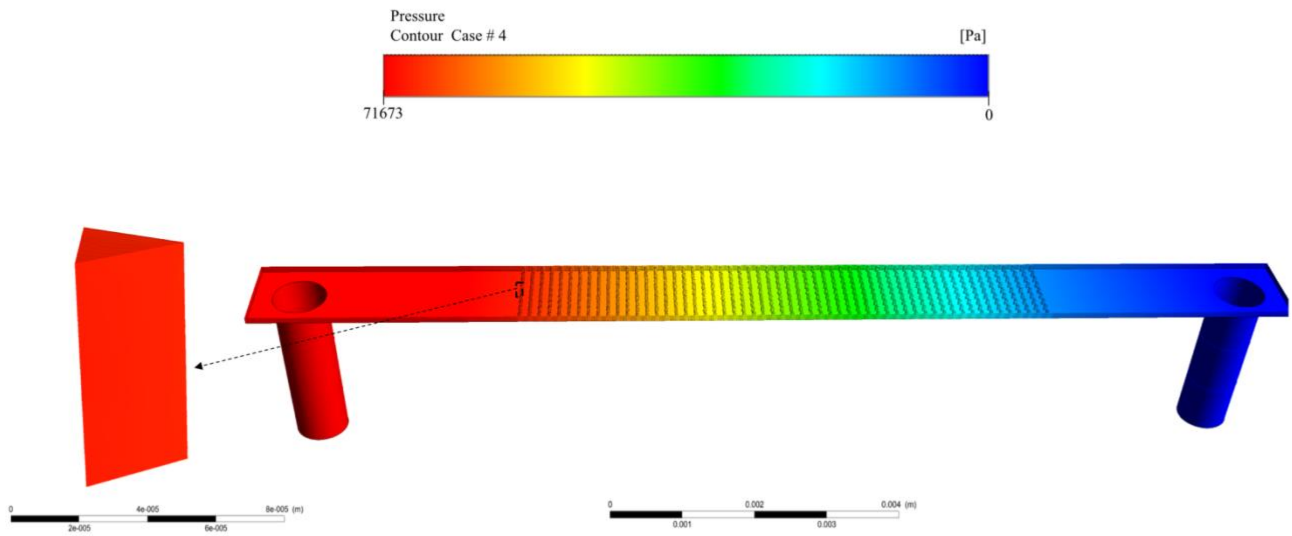
Pressure
Contour Case # 4
[Pa]
71673
0
0
4e-005
8e-005 (m)
2e-005
6e-005
0
0.002
0.004 (m)
0.001
0.003

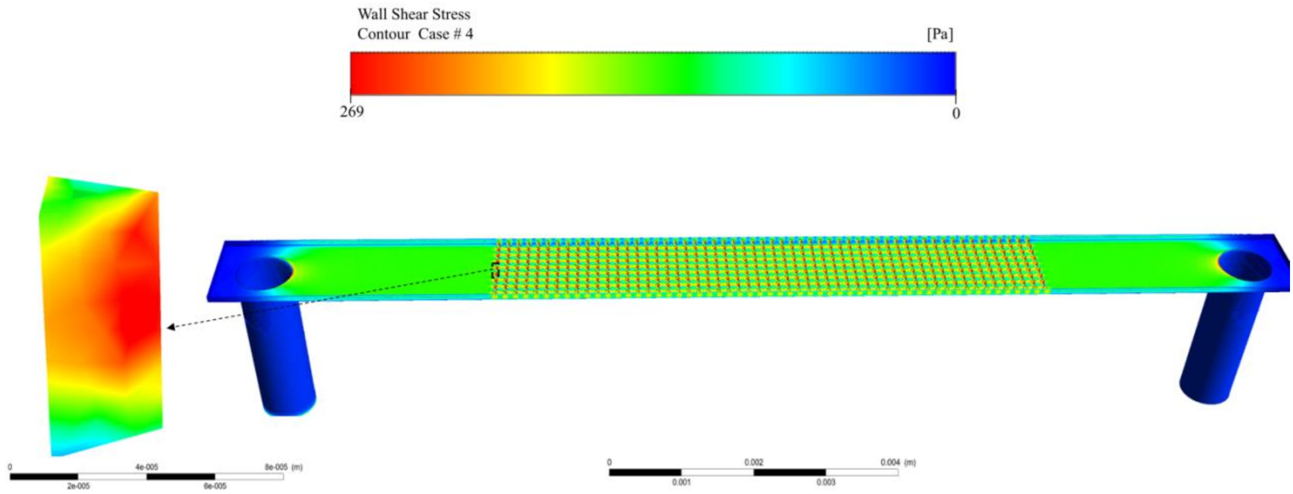
Wall Shear Stress
Contour Case # 4
[Pa]
269
0
0
4e-005
8e-005 (m)
2e-005
6e-005
0
0.002
0.004 (m)
0.001
0.003

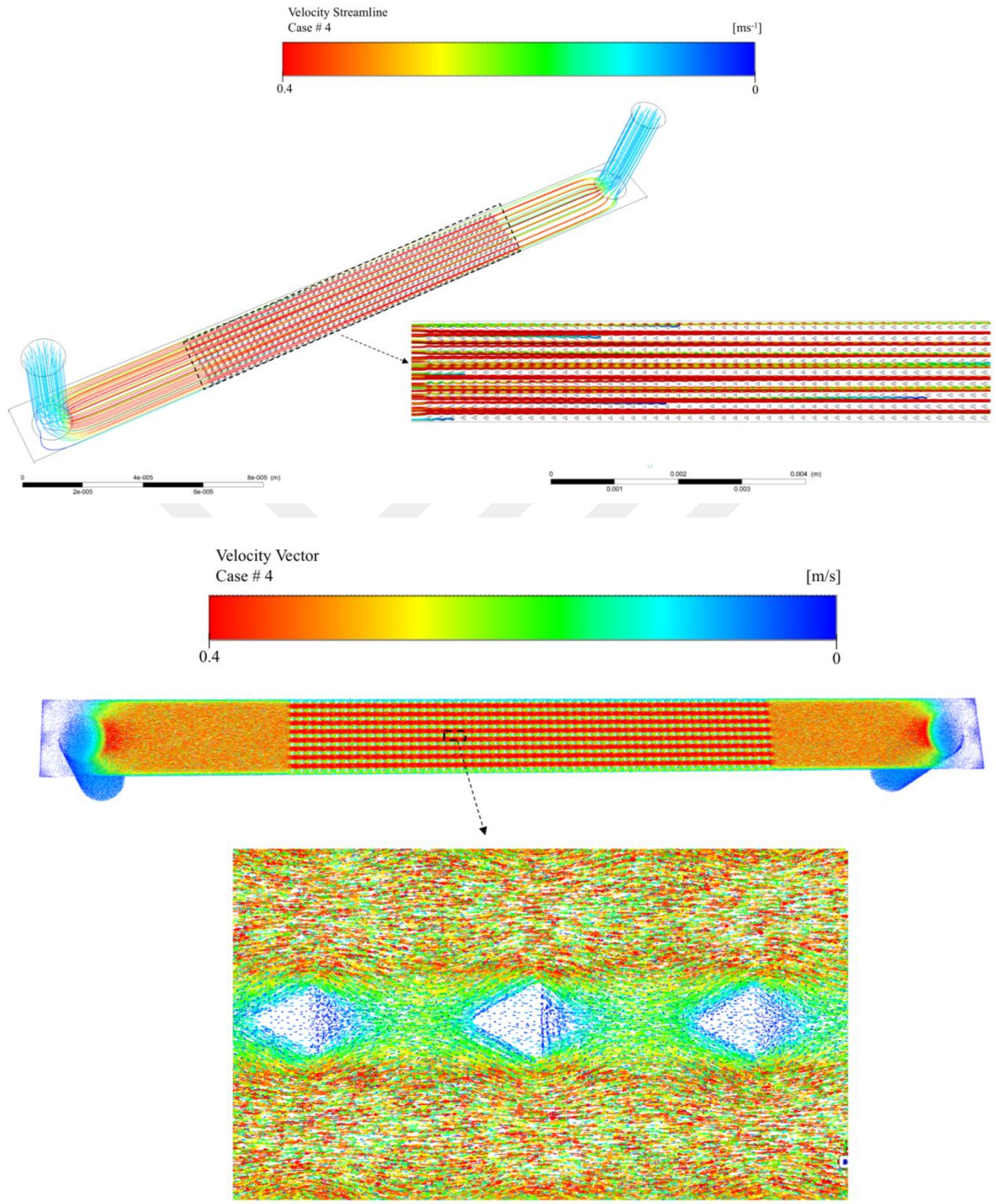

Figure 7:8 Contours of pressure and wall shear stress and the streamline of velocity vector of Case Study #4 (Triangle micropillars), 50µm inter-pillar spacing channel, blood flow (Casson model) with 90ml/hr flow rate.

The total pressure obtained inside the channel for all case studies with 30ml/hr to 150ml/hr flow rate in 1cP fluid flow is shown in Figure 7:9. The left column of Figure 7:9 shows the pressure versus flow rate graph for all pillar cases and 25µm,50µm,75µm inter-pillar spacing. The right column of Figure 7:9 shows the wall shear stress versus flow rate graph for all pillar cases and 25µm,50µm,75µm inter-pillar spacing.

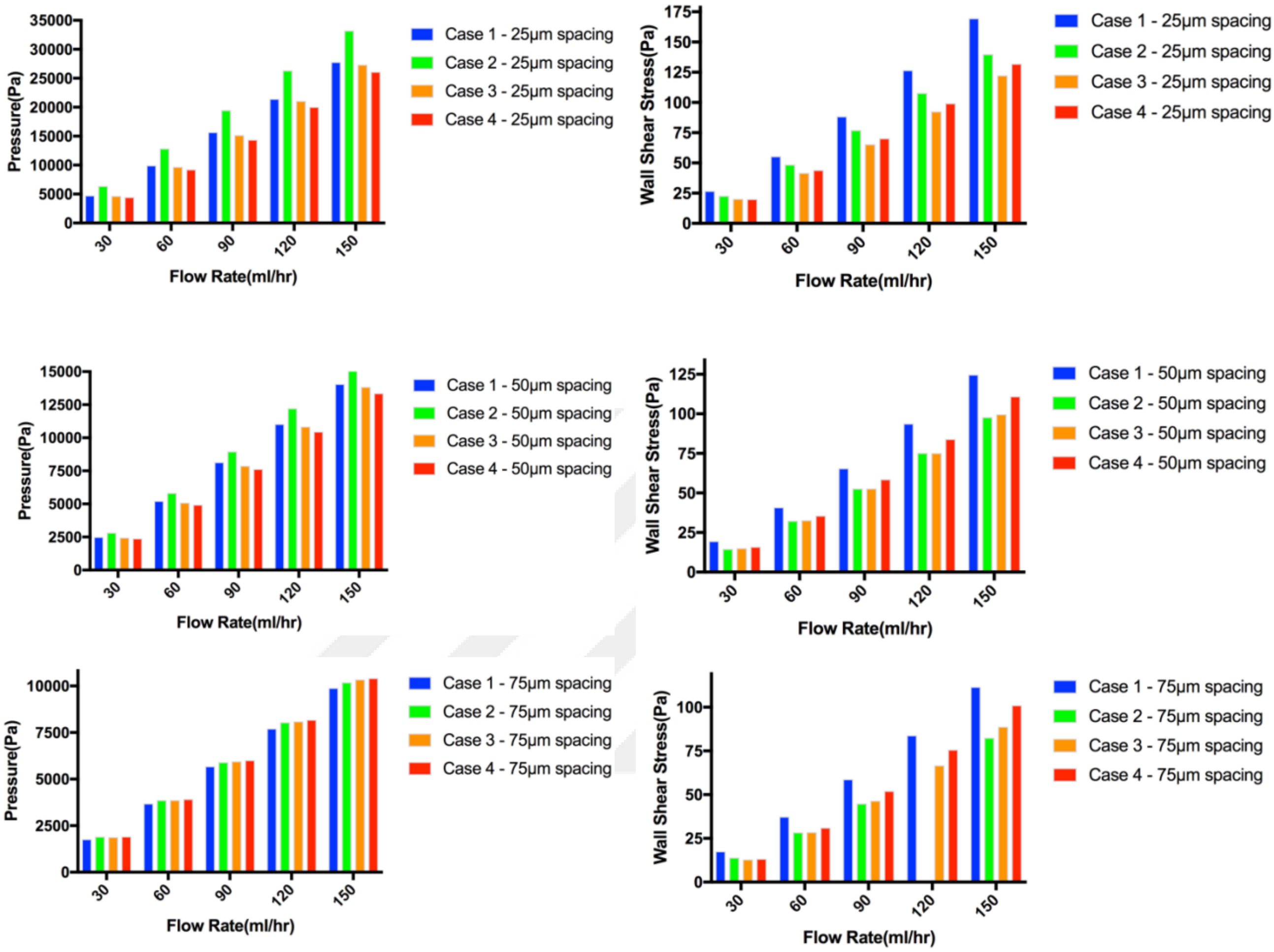

Figure 7:9 Pressure vs Flow Rate(left), Wall Shear Stress vs Flow Rate(right) for 25µm, 50 µm, 75 µm inter-pillar spacing geometries with all case studies for 1cP viscosity fluid(water) with 30ml/hr to 150ml/hr flow rates. (Case 1 : Cylindrical pillar shape, Case 2 : Square pillar shape, Case 3 : Diamond pillar shape, Case 4 : Triangle pillar shape)

The total pressure obtained inside the channel for all case studies with 30ml/hr to 150ml/hr flow rate in Casson model(blood) flow is shown in Figure 7:10. The left column of Figure 7: 10 shows the pressure versus flow rate graph for all pillar cases and 25µm,50µm,75µm inter-pillar spacing. The right column of Figure 7:10 shows the wall shear stress versus flow rate graph for all pillar cases and 25µm,50µm,75µm inter-pillar spacing.

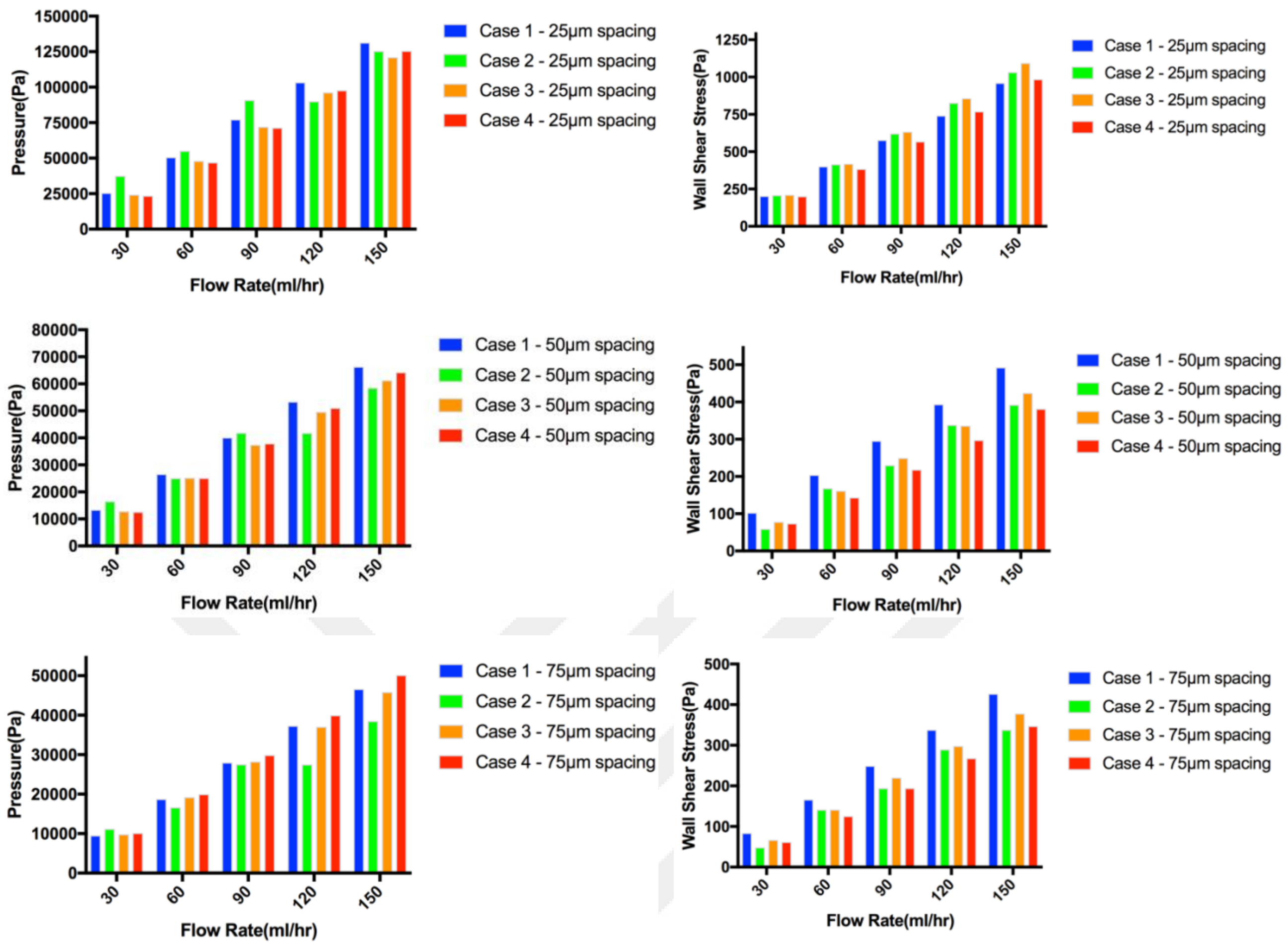

Figure 7:10 Pressure vs. Flow Rate(left), Wall Shear Stress vs. Flow Rate(right) for 25µm, 50 µm, 75 µm inter-pillar spacing geometries along all case studies for Casson model with 30ml/hr to 150ml/hr flow rates. (Case 1: Cylindrical pillar shape, Case 2: Square pillar shape, Case 3: Diamond pillar shape, Case 4: Triangle pillar shape)

The total force applied on per pillar is calculated via the equation below;

$$F_a = \vec{a} \cdot \vec{F}_p + \vec{a} \cdot \vec{F}_v$$

Equation 7:1 – Force Equation

Where, $\vec{a}$ is the specified force vector, $\vec{F}_p$ is the pressure force vector and $\vec{F}_v$ is the viscous force vector. In addition to the pressure, viscous and total forces, there is a force coefficient calculated by $\frac{1}{2}pv^2A$, where, p is the density, v is the velocity and the A is the area specified, in our case the total one pillar area.

Force per micropillar inside the channel with both 1cP viscosity(water) and Casson model(blood), at 30ml/hr to 150ml/hr flow rates for all case studies is given in Figure 7:10. These results were taken from the center pillar at the first pillar array of micropillars inside the channel.

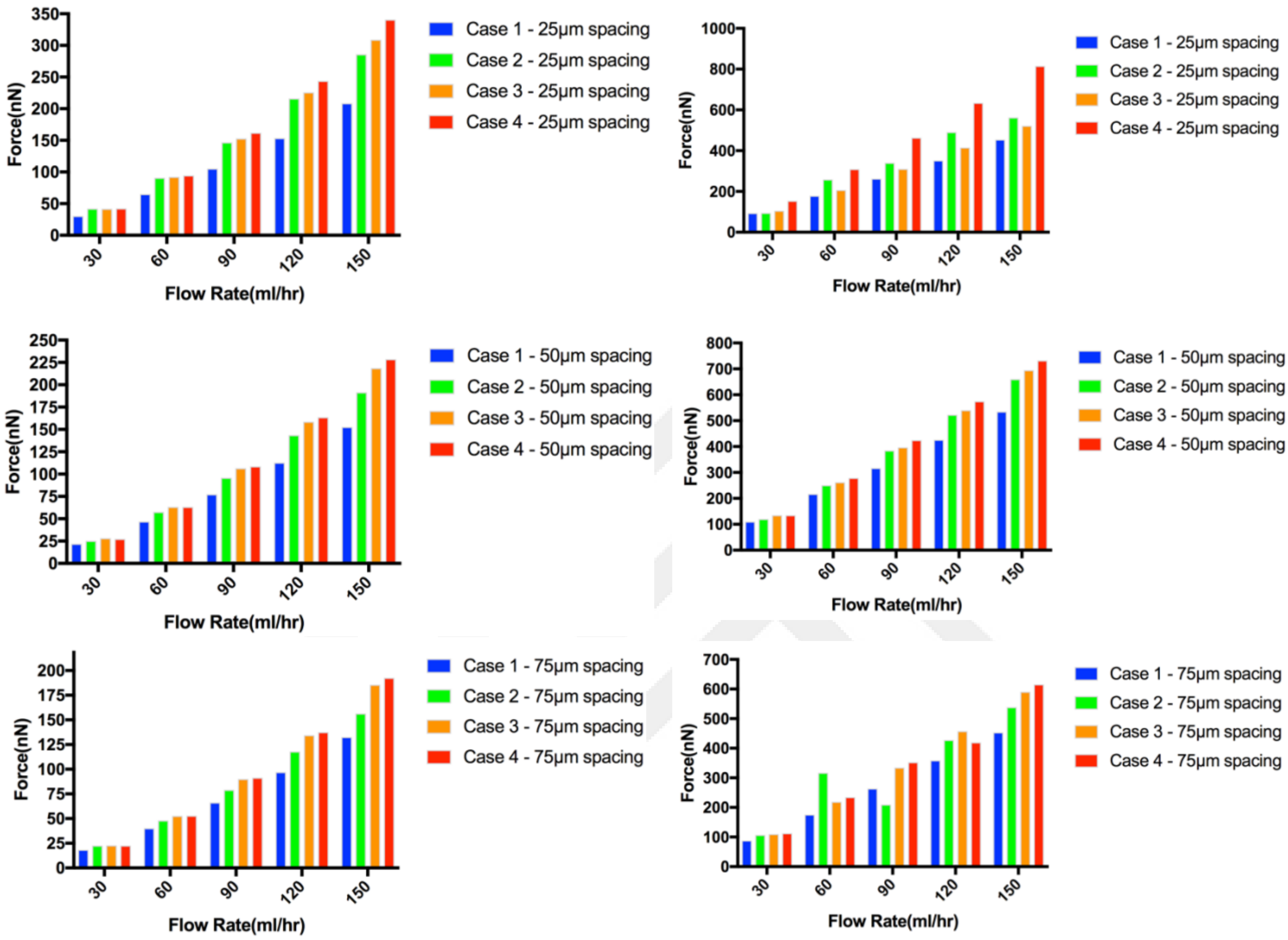

Figure 7:11 Force vs Flow Rate for 1cP viscosity(water) fluid for 25 µm, 50 µm, 75 µm inter-pillar spacing geometries along all case studies(left). Force vs Flow Rate for Casson model (blood) for 25 µm, 50 µm, 75 µm inter-pillar spacing geometries along all case studies(right). Results obtained from the center pillar at the first pilar array of micropillars. (Case 1: Cylindrical pillar shape, Case 2: Square pillar shape, Case 3: Diamond pillar shape, Case 4: Triangle pillar shape)

The first thing we figured out is with the non-Newtonian fluid flow characteristics. The Casson model that we used for blood flow shows linearity between shear stress and the strain rate in the example of 50 µm inter-pillar spacing with 30ml/hr to150ml/hr ranged flow rates as indicated in Figure 7: 12. E. Merrill[52] discussed the Casson model ad indicated that the Casson model is untenable with the hematocrit of around 40. Also, he showed that the blood behavior under high shear rates is Newtonian behavior. The non-Newtonian behavior is below the region of 100s^{-1} strain rate. Compared to his findings, we come up with the idea that, the blood with a hematocrit of 40 behaves as a non-Newtonian fluid inside our channel dimensions.

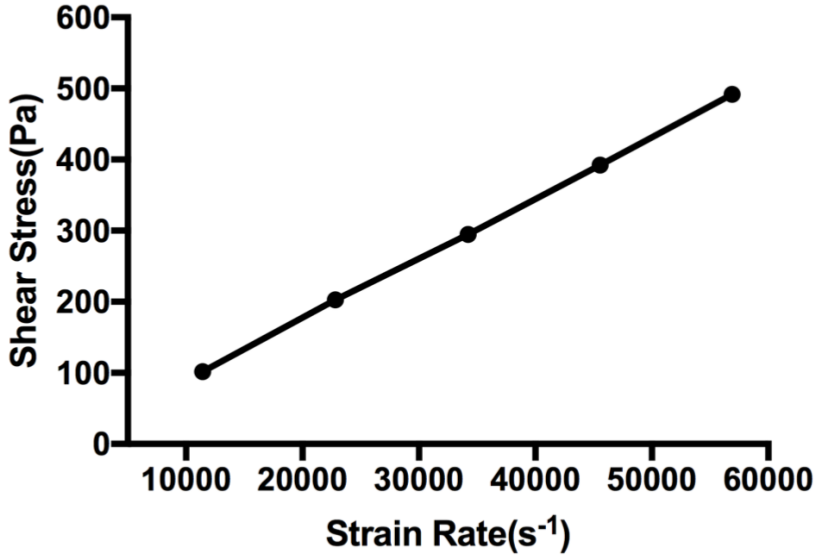

Figure 7:12 Shear Stress-Strain Rate relation in Casson model with 50 µm inter-pillar spaced cylindrical micropillar arrayed channel.

The presence of micropillars modifies the fluid velocity profile inside the channel; therefore the viscous force applied by the fluid[71]. According to this information, we investigate the pillar shape and inter-pillar spacing effects on the flow profiles.

In our case studies, we see that the increase of the inter-pillar spacing the pressure and wall shear stress inside the channel and the force applied to each pillar is decreasing for both fluids flows. According to these findings, we come up with the idea that, the increase with the inter-pillar spacing up to 3 times of the micropillar dimeter shows decrease within the flow characteristics with respect to the pressure and wall shear stress results, which will result in reliable and predictable data. There is a recent research about reducing the inter-pillar spacing of micropillars[79]. This optimization does not give an exact efficiency yet enhances the separation performance of RBC from whole blood with low flow rates. In the meantime, according to Stoecklein et al[72] inter-pillar spacing is crucial, concerning the pillar saturation with the subsequent micropillar in fluid flow. Small inter-pillar spacing within micropillars causes “cross-talk” in their respective fluid deformation, and the common basis of micropillar displacemeny analysis would collapse.

As for the shape analysis, the cylindrical micropillars shows higher shear stress inside the channel than square, triangle, and diamond-shaped micropillars for both blood and water flows. The pressure inside the channel is highest with cylindrical micropillars in blood flow, yet in water flow, we see that it is highest for square micropillars. We also realized that the diamond shaped and triangle shaped micropillars show similar resistance to the flow because of their sharp edge effect; therefore, they show similar results in case of both pressure and wall shear stress inside the channel. Moreover, the sharp edge effect causes less pressure and wall shear stress inside the channel. Force applied per pillar aspect of the simulations shows opposite conclusion with the pressure and wall shear stress results. The triangle shaped micropillars have the highest foce applied on one pillar for both blood and water flow simulations.

According to the information obtained from the simulations and mentioned above, our results are in a good agreement with the literature. There are many researchers studied the effects of different pillar shapes[73-76]. Cylinder pillars were the most popular for fluid flow a dn cell studies[71, 73]. However, Liu et al. [77] showed that triangular pillars are better for cell samples by large deformation because cells deform minimally around the pillar top. Zeming [78] studied the effects of various micropillar shapes, including circular, square, I-shaped, T-shaped, L-shaped micropillars. They found that square micropillars have constant and smooth fluid streamlines between the pillars where nothing creates a disturbance around the pillars in velocity streamline path. In our cases, the main difficulty indicated for all cases that there was a relatively small disturbance between vertical pillar arrays, which effects the micropillar displacement in the future applications.

The micropillar based channels have some limitations. Individual pillars are likely to be missing in size, shape, and height and any structural deformations inside the channel tend to affect the streams. Long channel lengths are needed to accomplish notable lateral displacement[80].

Comparison of Experiments and Simulation Models

In order to demonstrate the validity of the simulations done with both Fluent and Static Structural, we conduct a series of experiments with 1cP, 5cPviscosity fluids and with blood with the range of 30ml/hr to 120ml/hr flow rates. The results were promising in a way that the simulation and the experimental data shows a small deviation.

Figure 7:13 demonstrates both finite element model simulation and experimental flow rate vs. displacement relation of the square micropillars with an inter-pillar spacing of 75µm for 1cP and 5cP viscosity fluids. Moreover, the displacement – flow rate relation of blood flow for square micropillars with an inter-pillar spacing of 75µm is shown in Figure7:14. The simulations carried out with Casson model for the fluid material to represent the blood flow.

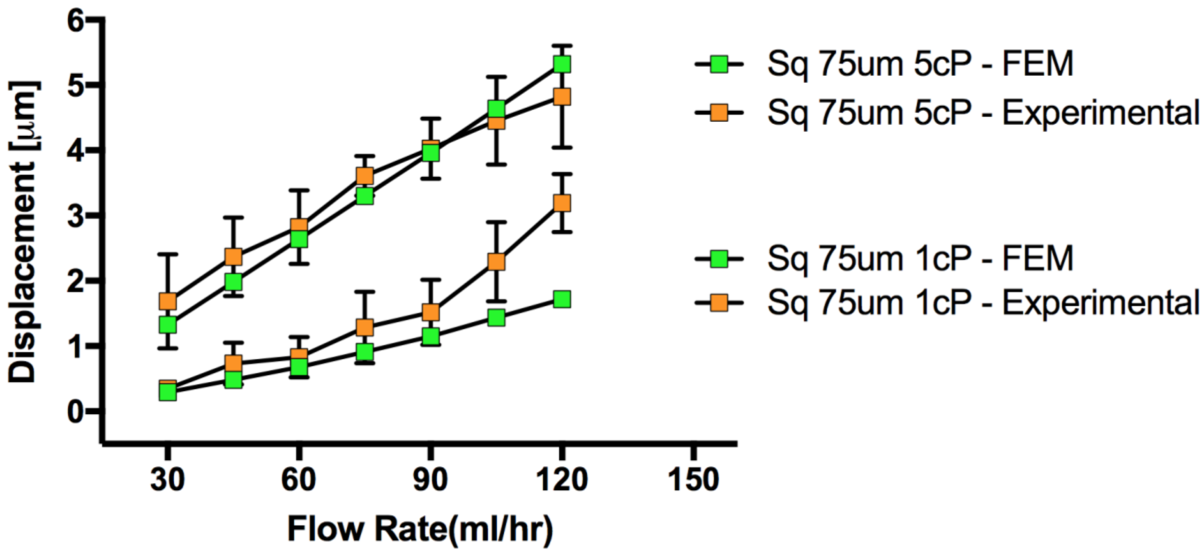

Figure 7:13 Displacement – Flow rate relation of square micropillars with an inter-pillar spacing of 75µm for 1cP and 5cP viscosity fluids.

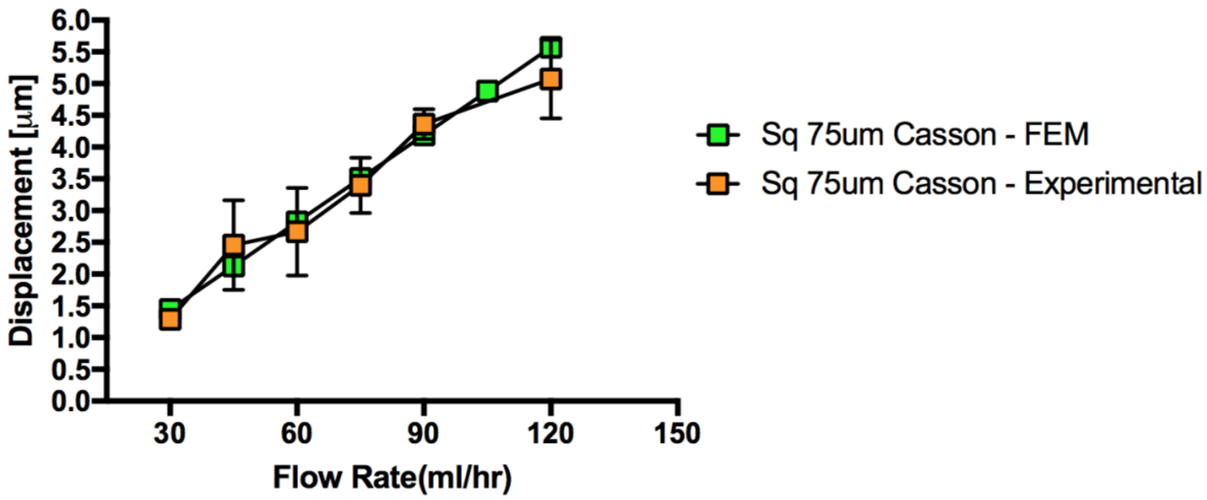

Figure 7:14 Displacement – Flow rate relation of square micropillars with an inter-pillar spacing of 75µm for blood flow.

The finite element model simulations and experimental data of displacement – flow rate relation for the cylindrical micropillars with an inter-pillar spacing of 75µm is indicated in Figure 7:15. As for the last demonstration of the displacement – flow rate relation of blood flow for cylindrical micropillars with an inter-pillar spacing of 75 µm is shown in Figure7:16. The simulations again carried out with Casson model for the fluid material to represent the blood flow.

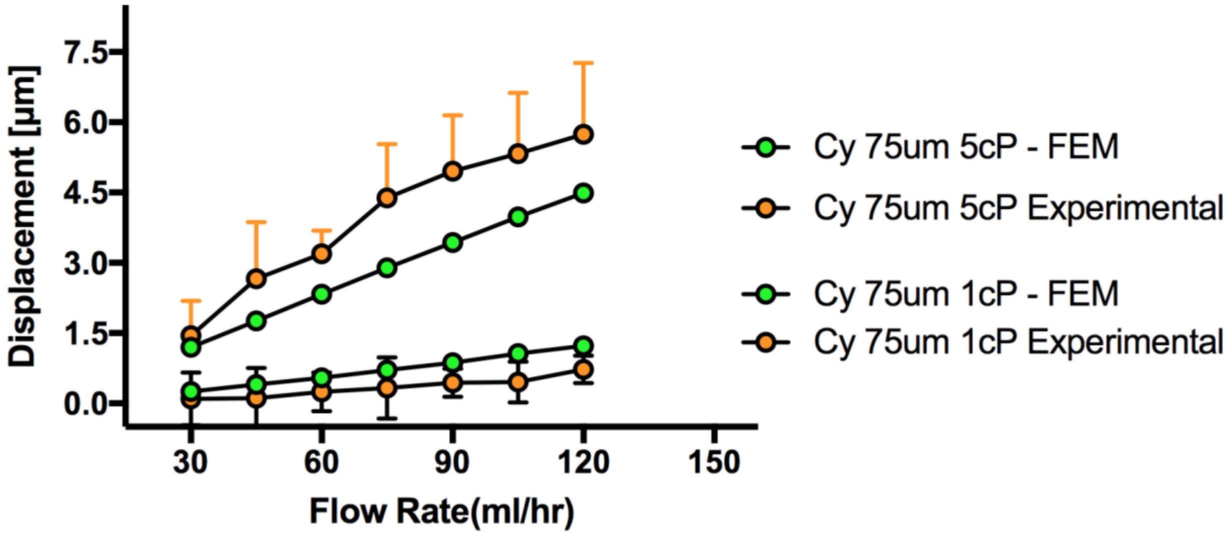

Figure 7:15 Displacement – Flow rate relation of cylindrical micropillars with an inter-pillar spacing of 75µm for 1cP and 5cP viscosity fluids.

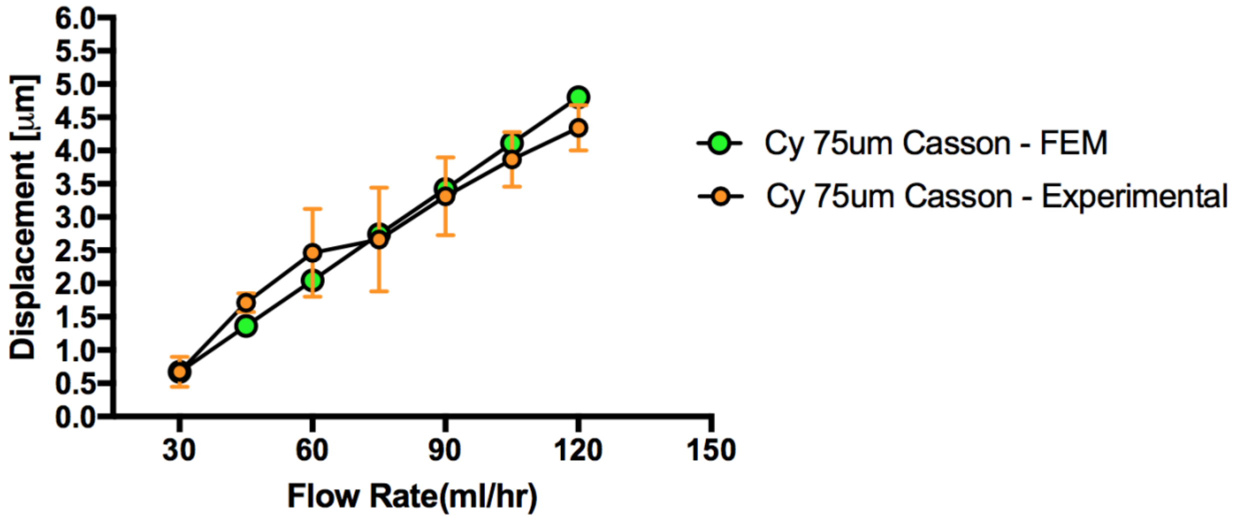

Figure 7:16 Displacement – Flow rate relation of cylindrical micropillars with an inter-pillar spacing of 75µm for blood flow.

We see from the displacement-flow rate relations that the Casson model is in a good agreement with blood characteristics. Both for the square and cylindrical micropillars were predicted with the finite element modelling. In the casson model, the initial viscosity is given as 4.7cP as it was measured for experiments with a hematocrit of around 40. As for the 1cP fluid flow of square micropillars, the results were deviated more with the increased flow rate. The possible reason for that can be the micropillars deformation over time. Experiments repeated three times for each flow rate, after some time, micropillars starts to deflect more and slowly returns to original position. Therefore, at the high flow rates experimental data is higher than the finite element model.

Chapter 8 CONCLUSION

As a conclusion, in this work, different micropillar arrays were designed and fabricated by an extensive study of both experimental and computational for microfluidic channels that can be used in fluid flow applications such as viscometers as a novel method.

The initial point of this work focused mostly on the case studies for flow and channel characteristics inside the various micropillar shape and inter-pillar spacing in a microfluidic channel using finite volume method. There are four types of shapes, and three different inter-pillar spacing have been analysed for Newtonian and Casson model used for non-Newtonian fluid flows. The first significant result at our studies is that the Casson model that we used for blood flow shows linearity between shear stress and the strain rate; therefore, the blood behaves as Newtonian fluid in our channels. The second finding is that the investigations on the case studies indicated that with the increase of the inter-pillar spacing the pressure and wall shear stress inside the channel and the force applied to each pillar is decreasing for both fluid flows. As for the shape analysis, the cylindrical micropillars shows high wall shear stress and pressure inside the channel for blood flow than square, triangle, and diamond-shaped micropillars. Nevertheless, the square shaped micropillars shows higher pressure in water flow then cylindrical micropillars. For the applied force aspect of the work, the triangle shaped micropillars have the highest foce applied on one pillar for both blood and water flow simulations.

The experimental and simulation data with concerning the micropillar displacement results are in a good agreement with each other for square and cylindrical micropillars for 1cP, 5cP and Casson model with 30ml/hr to 120ml/hr flow rate range. In the experiments for square and cylindrical micropillars, we found the micropillars get tired in time with the continuous flow; therefore, the results for high flow rates were slightly higher than the predicted data with simulation results.

This work outlines a notable step towards a new technology by investigating micropillar patterns and shapes within the microfluidic channels through an extensive range of fluid types that can be analyzed concerning the viscosity measurements. Overall, the investigations of different geometries and the ability to detect and analyze the displacement of micropillars through the dynamic fluid flow with different viscosities in this work could significantly contribute to the field of viscometers.

REFERENCES

[1] M. Bao and W. Wang, "Future of microelectromechanical systems (MEMS)," *Sensors and Actuators, A: Physical,* vol. 56, no. 1-2, p. 6, 1996.

[2] P. Tabeling, *Introduction to Microfluidics*. OUP Oxford, 2005.

[3] A. T. Giannitsis, "Microfabrication of biomedical lab-on-chip devices. A review," *Estonian Journal of Engineering,* vol. 17, no. 2, p. 30, 2011.

[4] S. K. Vashist, "Point-of-Care Diagnostics: Recent Advances and Trends," *Biosensors,* vol. 7, no. 4, 2017.

[5] A. St John and C. P. Price, "Existing and Emerging Technologies for Point-of-Care Testing," *Clin Biochem Rev,* vol. 35, no. 3, pp. 155-67, Aug 2014.

[6] L. J. Enriquez and L. Shore-Lesserson, "Point-of-care coagulation testing and transfusion algorithms," *Br J Anaesth,* vol. 103 Suppl 1, pp. i14-22, Dec 2009.

[7] C. M. Samama and Y. Ozier, "Near-patient testing of haemostasis in the operating theatre: an approach to appropriate use of blood in surgery," *Vox Sang,* vol. 84, no. 4, pp. 251-5, May 2003.

[8] A. J. Tudos, G. J. Besselink, and R. B. Schasfoort, "Trends in miniaturized total analysis systems for point-of-care testing in clinical chemistry," *Lab Chip,* vol. 1, no. 2, pp. 83-95, Dec 2001.

[9] D. J. Perry, D. A. Fitzmaurice, S. Kitchen, I. J. Mackie, and S. Mallett, "Point-of-care testing in haemostasis," *Br J Haematol,* vol. 150, no. 5, pp. 501-14, Sep 2010.

[10] L. Syedmoradi, M. Daneshpour, M. Alvandipour, F. A. Gomez, H. Hajghassem, and K. Omidfar, "Point of care testing: The impact of nanotechnology," *Biosensors and Bioelectronics,* 2017.

[11] A. M. Dupuy, S. Lehmann, J. P. Cristol, and S. Lehmann, "Protein Biochip Systems for the Clinical Laboratory," *Clinical Chemistry and Laboratory Medicine,* 2005.

[12] P. Yager *et al.*, "Microfluidic diagnostic technologies for global public health," *Nature,* 2006.

[13] P. Von Lode, "Point-of-care immunotesting: Approaching the analytical performance of central laboratory methods," *Clinical Biochemistry,* 2005.

[14] P. Yager, G. J. Domingo, and J. Gerdes, "Point-of-Care Diagnostics for Global Health," *Annual Review of Biomedical Engineering,* 2008.

[15] H. Lu, L. Y. Koo, W. M. Wang, D. A. Lauffenburger, L. G. Griffith, and K. F. Jensen, "Microfluidic shear devices for quantitative analysis of cell adhesion," *Anal Chem,* vol. 76, no. 18, pp. 5257-64, Sep 15 2004.

[16] F. A. Gomez, *Biological Applications of Microfluidics*. John Wiley & Sons, 2008.

[17] J. C. McDonald *et al.*, "Fabrication of microfluidic systems in poly(dimethylsiloxane)," *Electrophoresis,* vol. 21, no. 1, pp. 27-40, Jan 2000.

[18] C. Macosko, *Principles of Rheology: Measurements and Applications* John Wiley and Sons, 1994.

[19] S. Gupta, W. S. Wang, and S. A. Vanapalli, "Microfluidic viscometers for shear rheology of complex fluids and biofluids," *Biomicrofluidics,* vol. 10, no. 4, p. 043402, Jul 2016.

[20] Y. Li, K. R. Ward, and M. A. Burns, "Viscosity Measurements Using Microfluidic Droplet Length," *Anal Chem,* vol. 89, no. 7, pp. 3996-4006, Apr 4 2017.

[21] T. Gervais, J. El-Ali, A. Gunther, and K. F. Jensen, "Flow-induced deformation of shallow microfluidic channels," *Lab Chip,* vol. 6, no. 4, pp. 500-7, Apr 2006.

[22] F. Del Giudice, F. Greco, P. A. Netti, and P. L. Maffettone, "Is microrheometry affected by channel deformation?," *Biomicrofluidics,* vol. 10, no. 4, p. 043501, Jul 2016.

[23] A. K. Geim, S. V. Dubonos, I. V. Grigorieva, K. S. Novoselov, A. A. Zhukov, and S. Y. Shapoval, "Microfabricated adhesive mimicking gecko foot-hair," *Nat Mater,* vol. 2, no. 7, pp. 461-3, Jul 2003.

[24] C. Greiner, A. D. Campo, and E. Arzt, "Adhesion of bioinspired micropatterned surfaces: effects of pillar radius, aspect ratio, and preload," *Langmuir,* vol. 23, no. 7, pp. 3495-502, Mar 27 2007.

[25] A. Mahdavi *et al.*, "A biodegradable and biocompatible gecko-inspired tissue adhesive," *Proc Natl Acad Sci U S A,* vol. 105, no. 7, pp. 2307-12, Feb 19 2008.

[26] L. Qu, L. Dai, M. Stone, Z. Xia, and Z. L. Wang, "Carbon nanotube arrays with strong shear binding-on and easy normal lifting-off," *Science,* vol. 322, no. 5899, pp. 238-42, Oct 10 2008.

[27] A. Tuteja *et al.*, "Designing superoleophobic surfaces," *Science,* vol. 318, no. 5856, pp. 1618-22, Dec 7 2007.

[28] A. Ahuja *et al.*, "Nanonails: a simple geometrical approach to electrically tunable superlyophobic surfaces," *Langmuir,* vol. 24, no. 1, pp. 9-14, Jan 1 2008.

[29] T. N. Krupenkin, J. A. Taylor, T. M. Schneider, and S. Yang, "From rolling ball to complete wetting: the dynamic tuning of liquids on nanostructured surfaces," *Langmuir,* vol. 20, no. 10, pp. 3824-7, May 11 2004.

[30] C. M. Cesa, N. Kirchgessner, D. Mayer, U. S. Schwarz, B. Hoffmann, and R. Merkel, "Micropatterned silicone elastomer substrates for high resolution analysis of cellular force patterns," *Rev Sci Instrum,* vol. 78, no. 3, p. 034301, Mar 2007.

[31] O. du Roure *et al.*, "Force mapping in epithelial cell migration," *Proc Natl Acad Sci U S A,* vol. 102, no. 7, pp. 2390-5, Feb 15 2005.

[32] N. J. Sniadecki *et al.*, "Magnetic microposts as an approach to apply forces to living cells," *Proc Natl Acad Sci U S A,* vol. 104, no. 37, pp. 14553-8, Sep 11 2007.

[33] N. J. Sniadecki and C. S. Chen, "Microfabricated silicone elastomeric post arrays for measuring traction forces of adherent cells," *Methods Cell Biol,* vol. 83, pp. 313-28, 2007.

[34] N. J. Sniadecki, C. M. Lamb, Y. Liu, C. S. Chen, and D. H. Reich, "Magnetic microposts for mechanical stimulation of biological cells: fabrication, characterization, and analysis," *Rev Sci Instrum,* vol. 79, no. 4, p. 044302, Apr 2008.

[35] J. L. Tan, J. Tien, D. M. Pirone, D. S. Gray, K. Bhadriraju, and C. S. Chen, "Cells lying on a bed of microneedles: an approach to isolate mechanical force," *Proc Natl Acad Sci U S A,* vol. 100, no. 4, pp. 1484-9, Feb 18 2003.

[36] B. A. Evans, A. R. Shields, R. L. Carroll, S. Washburn, M. R. Falvo, and R. Superfine, "Magnetically actuated nanorod arrays as biomimetic cilia," *Nano Lett,* vol. 7, no. 5, pp. 1428-34, May 2007.

[37] Y. Tanaka *et al.*, "Demonstration of a PDMS-based bio-microactuator using cultured cardiomyocytes to drive polymer micropillars," *Lab Chip,* vol. 6, no. 2, pp. 230-5, Feb 2006.

[38] Y. Tanaka *et al.*, "Demonstration of a bio-microactuator powered by vascular smooth muscle cells coupled to polymer micropillars," *Lab Chip,* vol. 8, no. 1, pp. 58-61, Jan 2008.

[39] D. Chandra and S. Yang, "Stability of High-Aspect-Ratio Micropillar Arrays against Adhesive and Capillary Forces," *ACCOUNTS OF CHEMICAL RESEARCH* vol. 43, no. 8, pp. 1080-1091, 2010.

[40] K. Autumn *et al.*, "Adhesive force of a single gecko foot-hair," *Nature,* vol. 405, no. 6787, pp. 681-5, Jun 8 2000.

[41] A. Sidorenko, T. Krupenkin, A. Taylor, P. Fratzl, and J. Aizenberg, "Reversible switching of hydrogel-actuated nanostructures into complex micropatterns," *Science,* vol. 315, no. 5811, pp. 487-90, Jan 26 2007.

[42] A. Saez, M. Ghibaudo, A. Buguin, P. Silberzan, and B. Ladoux, "Rigidity-driven growth and migration of epithelial cells on microstructured anisotropic substrates," *Proc Natl Acad Sci U S A,* vol. 104, no. 20, pp. 8281-6, May 15 2007.

[43] R. Chen, M. C. Lu, V. Srinivasan, Z. Wang, H. H. Cho, and A. Majumdar, "Nanowires for enhanced boiling heat transfer," *Nano Lett,* vol. 9, no. 2, pp. 548-53, Feb 2009.

[44] H. K. Versteeg and W. Malalasekera, *An Introduction to Computational Fluid Dynamics - The Finite Volume Method*. Harlow, England: Pearson Education Ltd., 2007.

[45] H. A. Stone, "Introduction to Fluid Dynamics for Microfluidic Flows," in *CMOS Biotechnology*(Series on Integrated Circuits and Systems, Boston, MA: Springer, 2007, pp. 5-30.

[46] R. A. Secco, J. R. deBruyn, and M. Kostic. Fluid Viscosity Measurement [Online]. Available: http://www.kostic.niu.edu/K12208_C046-Viscosity-PR.pdf

[47] D. A. Rubenstein, W. Yin, and M. D. Frame, *Biofluid Mechanics*. Academic Press, 2016, p. 544.

[48] R. P. Chhabra and J. F. Richardson, "Non-Newtonian fluid behaviour," in *Non-Newtonian Flow in the Process Industries*, 1999, pp. 1-36.

[49] N. Hamedi and S. Busch, "CFD with OpenSource software Non-Newtonian Models in OpenFOAM Implementation of a non-Newtonian model," 2014.

[50] G. W. Blair, "An equation for the flow of blood, plasma and serum through glass capillaries," *Nature,* vol. 183, no. 4661, pp. 613-4, Feb 28 1959.

[51] J. L. Martin, R. M. Jacobs, and A. L. Copley, "Apparent viscosity of whole human blood at various hydrostatic pressures. I. Studies on anticoagulated blood employing a new capillary viscometer," *Biorheology,* vol. 11, no. 6, pp. 439-48, Nov 1974.

[52] E. W. Merrill, A. M. Benis, E. R. Gilliland, T. K. Sherwood, and E. W. Salzman, "Pressure-flow relations of human blood in hollow fibers at low flow rates," *J Appl Physiol,* vol. 20, no. 5, pp. 954-67, Sep 1965.

[53] S. Pramanik, "Casson fluid flow and heat transfer past an exponentially porous stretching surface in presence of thermal radiation," *Ain Shams Engineering Journal,* vol. 5, no. 1, p. 7, 2014.

[54] S. R. Idelsohn and E. Oñate, "Finite volumes and finite elements: two good friends.," *International Journal for Numerical Methods in Engineering,* vol. 37, no. 19, p. 18, 1994.

[55] S. Rao, *The Finite Element Method in Engineering*, 5 ed. Butterworth-Heinemann, 2010, p. 726.

[56] O. C. Zienkiewicz and R. L. Taylor, *The Finite Element Method*, 5 ed. Butterworth-Heinemann, 2000.

[57] J. Venkatesan, D. S. Sankar, K. Hemalatha, and Y. Yatim, "Mathematical Analysis of Casson Fluid Model for Blood Rheology in Stenosed Narrow Arteries," *Journal of Applied Mathematics,* vol. 2013, pp. 1-11, 2013.

[58] I. D. Johnston, D. K. McCluskey, C. K. L. Tan, and M. C. Tracey, "Mechanical characterization of bulk Sylgard 184 for microfluidics and microengineering," *Journal of Micromechanics and Microengineering,* vol. 24, no. 3, 2014.

[59] D. Qin, Y. Xia, and G. M. Whitesides, "Soft lithography for micro- and nanoscale patterning," *Nat Protoc,* vol. 5, no. 3, pp. 491-502, Mar 2010.

[60] H. Lee, K. Lee, B. Ahn, J. Xu, L. Xu, and K. W. Oh, "A new fabrication process for uniform SU-8 thick photoresist structures by simultaneously removing edge bead and air bubbles," *Journal of Micromechanics and Microengineering,* vol. 21, no. 12, 2011.

[61] R. L. Barber, M. K. Ghantasala, R. Divan, K. D. Vora, E. C. Harvey, and D. C. Mancini, "Optimisation of SU-8 processing parameters for deep X-ray lithography," *Microsystem Technologies,* vol. 11, no. 4-5, pp. 303-310, 2005.

[62] N. E. Oyunbaatar, D. H. Lee, S. J. Patil, E. S. Kim, and D. W. Lee, "Biomechanical Characterization of Cardiomyocyte Using PDMS Pillar with Microgrooves," *Sensors (Basel),* vol. 16, no. 8, Aug 9 2016.

[63] B. Li, L. Xie, Z. C. Starr, Z. Yang, J. S. Lin, and J. H. Wang, "Development of micropost force sensor array with culture experiments for determination of cell traction forces," *Cell Motil Cytoskeleton,* vol. 64, no. 7, pp. 509-18, Jul 2007.

[64] I. Schoen, W. Hu, E. Klotzsch, and V. Vogel, "Probing cellular traction forces by micropillar arrays: contribution of substrate warping to pillar deflection," *Nano Lett,* vol. 10, no. 5, pp. 1823-30, May 12 2010.

[65] S. M. Khare, A. Awasthi, V. Venkataraman, and S. P. Koushika, "Colored polydimethylsiloxane micropillar arrays for high throughput measurements of forces applied by genetic model organisms," *Biomicrofluidics,* vol. 9, no. 1, p. 014111, Jan 2015.

[66] K. Nagayama, T. Inoue, Y. Hamada, and T. Matsumoto, "A novel patterned magnetic micropillar array substrate for analysis of cellular mechanical responses," *J Biomech,* vol. 65, pp. 194-202, Dec 8 2017.

[67] S. Ghassemi, N. Biais, K. Maniura, S. J. Wind, M. P. Sheetz, and J. Hone, "Fabrication of elastomer Pillar Arrays with Modulated Stiffness for Cellular Force Measurements," *J Vac*

Sci Technol B Microelectron Nanometer Struct Process Meas Phenom, vol. 26, no. 6, pp. 2549-2553, Nov 1 2008.

[68] A. Kajzar, C. M. Cesa, N. Kirchgessner, B. Hoffmann, and R. Merkel, "Toward physiological conditions for cell analyses: forces of heart muscle cells suspended between elastic micropillars," *Biophys J,* vol. 94, no. 5, pp. 1854-66, Mar 1 2008.

[69] K. Kim, J. Koo, S. Moon, and W. G. Lee, "Role of micropillar arrays in cell rolling dynamics," *Analyst,* vol. 142, no. 1, pp. 110-117, Dec 19 2016.

[70] C. Roh, J. Lee, and C. Kang, "Physical Properties of PDMS (Polydimethylsiloxane) Microfluidic Devices on Fluid Behaviors: Various Diameters and Shapes of Periodically-Embedded Microstructures," *Materials (Basel),* vol. 9, no. 10, Oct 15 2016.

[71] B. Darbois, T. P. Laurent, S. Stoukatch, and S. Dorbolo, "Wicking through a confined micropillar array," *Microfluid Nanofluid,* vol. 20, no. 53, 2016.

[72] D. Stoecklein, C. Wu, D. Kim, D. D. Carlo, and B. Ganapathysubramanian, "Optimization of micropillar sequences for fluid flow sculpting," *Physics of Fluids,* vol. 28, 2016.

[73] S. H. Holm, J. P. Beech, M. P. Barrett, and J. O. Tegenfeldt, "Separation of parasites from human blood using deterministic lateral displacement," *Lab Chip,* vol. 11, no. 7, pp. 1326-32, Apr 7 2011.

[74] J. P. Beech, S. H. Holm, K. Adolfsson, and J. O. Tegenfeldt, "Sorting cells by size, shape and deformability," *Lab Chip,* vol. 12, no. 6, pp. 1048-51, Mar 21 2012.

[75] D. Holmes *et al.*, "Separation of blood cells with differing deformability using deterministic lateral displacement(dagger)," *Interface Focus,* vol. 4, no. 6, p. 20140011, Dec 6 2014.

[76] N. M. Karabacak *et al.*, "Microfluidic, marker-free isolation of circulating tumor cells from blood samples," *Nat Protoc,* vol. 9, no. 3, pp. 694-710, Mar 2014.

[77] Z. Liu *et al.*, "Rapid isolation of cancer cells using microfluidic deterministic lateral displacement structure," *Biomicrofluidics,* vol. 7, no. 1, p. 11801, 2013.

[78] K. K. Zeming, S. Ranjan, and Y. Zhang, "Rotational separation of non-spherical bioparticles using I-shaped pillar arrays in a microfluidic device," *Nat Commun,* vol. 4, p. 1625, 2013.

[79] K. K. Zeming, T. Salafi, C. H. Chen, and Y. Zhang, "Asymmetrical Deterministic Lateral Displacement Gaps for Dual Functions of Enhanced Separation and Throughput of Red Blood Cells," *Sci Rep,* vol. 6, p. 22934, Mar 10 2016.

[80] D. J. Collins, T. Alan, and A. Neild, "Particle separation using virtual deterministic lateral displacement (vDLD)," *Lab Chip,* vol. 14, no. 9, pp. 1595-603, May 7 2014.